INVESTIGATION OF BLOCKAGE EFFECTS FROM FLOW ABOUT CIRCULAR CYLINDERS IN A TWO-DIMENSIONAL WIND TUNNEL

Thesis by

Louis V. Schmidt

In Partial Fulfillment of the Requirements

For the Degree of

Aeronautical Engineer

California Institute of Technology

Pasadena, California

1950

ACKNOWLEDGEMENT

The author wishes to express his appreciation to Dr. Clark B. Millikan under whose direction this research investigation was carried out. He sincerely appreciates the assistance of Messrs. Richard W. Bell, Josiah E. Smith and Edwin Pounder with regard to technical problems. He is indebted to the members of the GALCIT ten-foot wind tunnel staff for their splendid cooperation during the investigations, and to Mmes. Nell Kindig and Marguerite Schmidt for their efforts in preparing the manuscript.

ABSTRACT

In these investigations a study of the blockage effects encountered in wind tunnel testing was made. Emphasis was placed on obtaining perceptible values of wake blockage in order to check the reliability of approximate derivations that are based on the assumption of small wakes. A bluff body (circular cylinder) was chosen for these investigations since it develops a pronounced wake. Three cylinders of varying size were employed in order to obtain a variation in the magnitudes of the blockage effects.

The combined influence of surface irregularities such as static pressure orifices and the vertical walls resulted in the flow over the cylinders exhibiting three-dimensional characteristics. An investigation of these effects was conducted in order to determine means of circumventing three-dimensional characteristics. Two-dimensional flow characteristics were realized after the point of flow separation on the aft portion of the cylinder was made uniform in the spanwise direction. This was accomplished by means of separation strips fastened to the cylinder forward of the point of maximum thickness.

After the realization of two-dimensional flow characteristics in the test section, the original purpose of the test was carried out to a limited extent. Experimental measurements of wake blockage effects were compared with the predicted values that are based on approximate derivations for cases where comparison could be made.

TABLE OF CONTENTS

INDEX OF RUNS

Date	Run	Configuration	Test	q_o, $\frac{lb}{ft^2}$	α_g	Remarks
3-30-48	1	Clear Tunnel	P_2+P_2'	10		
"	2	" "	" + "	20		
"	3	" "	" + "	40		
"	4	" "	" + "	80		
4-1-48	5	C_1	P_1+P_2	Vary	-4.37°	
"	6	" + R_1	$P_1+P_2+P_3$	80	"	
"	7	" + R_2	P_3	"	"	
"	8	" + R_3	"	"	"	
"	9	" + R_4	"	"	"	
"	10	" + R_5	"	"	"	
"	11	" + R_6	"	"	"	
"	12	" + R_7	"	"	"	
4-2-48	13	"	P_2'	"	"	
"	5A	"	P_1	"	0°	Repeat of Run 5 at $\alpha_g = 0^\circ$
"	14	" + T_1 + R_1	$P_1+P_2+P_3$	"	"	
"	15	" + " + R_2	P_3	"	"	
"	16	" + " + R_3	"	"	"	
4-5-48	17	" + T_2	P_1	"	"	
"	18	" + T_3 + R_3	$P_1+P_2+P_3$	"	"	
"	19	" + "	P_2+P_1 (Vis.)	"	"	

INDEX OF RUNS (Cont.)

Date	Run	Configuration	Test	q_o $\frac{lb}{ft^2}$	α_g	Remarks
4-5-48	20	$C_1 + T_3 + R_2$	P_3	80	0°	
"	21	" + " + R_1	"	"	"	
4-6-48	22	" + T_4 + "	"	"	"	
"	23	" + " + R_2	P_3+P_1(Vis.)	"	"	
"	24	" + " + R_3	P_1+P_2+P_3	"	"	
"	25	" + "	P_2'	"	"	
"	26	" + T_2	P_2+P_1(Vis.)	"	"	
"	27	Clear Tunnel	P_2'	Vary		
4-7-48	28	C_3	P_1	"	0°	
"	29	C_3 + R_1	P_1+P_2+P_3	10	"	
4-8-48	30	C_3 + R_2	P_3	"	"	
"	31	"	P_2'	"	"	
"	32	" + T_5 + R_1	P_1+P_2+P_3	"	"	
"	33	" + " + R_2	P_3	"	"	
"	34	" + "	P_2'	"	"	
"	35	" + T_6 + R_2	P_1+P_2	"	"	
"	36	" + T_7 + "	P_1+P_2+P_3	"	"	
4-9-48	37	" + " + R_1	P_3	"	"	
"	38	" + "	P_2'	"	"	
4-28-48	39	Clear Tunnel	Press.			Calibration of Rake Statics
4-29-48	40	C_1 + R_5	P_3	80	0°	Model Orifices Taped

INDEX OF RUNS (Cont.)

Date	Run	Configuration	Test	q_o, $\frac{lb}{ft^2}$	α_g	Remarks
4-29-48	41	$C_1 + R_4$	P_3	80	0°	Model Orifices Taped
"	42	" + R_1	"	"	"	Model Orifices Taped
"	43	" + R_4	P_3(Vis.)	"	"	Model Orifices Taped, Tape on Model in front of Rake
"	44	" + R_1	"	"	"	Model Orifices Taped, Tape on Model in front of Rake
"	45	" + "	P_3	"	"	Cylinder Orifices Waxed
4-30-48	46	" + R_5	"	"	"	Cylinder Orifices Waxed
"	46A	" + "	"	"	"	Cylinder Orifices Waxed, Wiped Model of Surface Oxidation
"	47	" + R_4	"	"	"	Cylinder Orifices Waxed
"	48	" + R_8	"	"	"	Cylinder Orifices Waxed
"	48A	" + "	"	"	"	Cylinder Orifices Waxed
"	49	" + R_8'	P_3(Vis.)	"	"	
5-1-48	50	" + T_8 + R_8'	"	"	"	Sandpaper Separation Strips Blew Loose
"	50A	" + " + "	"	"	"	Repeat of Run 50

INDEX OF RUNS (Cont.)

Date	Run	Configuration	Test	q_o, lb/ft²	α_g	Remarks
5-1-48	51	$C_1 + T_9 + R_8'$	P_3(Vis.)	80	0°	
5-3-48	52	" + T_{10} + "	P_3(Vis.)+P_4	"	"	End Plate Unsealed
"	49A	" + R_8	" +"	"	"	Cylinder Orifices Waxed, End Plate Unsealed
"	49B	" + "	" +"	"	"	Cylinder Orifices Waxed, End Plate Sealed
"	53	" + X_1 + R_8'	" +"	"	"	
"	54	" + " + R_8''	P_3(Vis.)	"	"	
5-4-48	55	" + S_1 + R_8'	"	"	"	
"	56	" + R_8	P_2+P_3	"	"	
"	57	" + R_9	" + "	"	"	
"	58	" + R_9'	P_3(Vis.)	"	"	
"	49C	" + R_8'	"	"	"	Cylinder Orifices Waxed, End Plate Sealed, Repeat of Run 49B
5-5-48	59	" + T_2 + R_8	P_2+P_3	"	"	
"	60	" + " + R_9	P_3	"	"	
"	61	" + T_4 + "	P_2+P_3	"	"	
"	62	" + " + R_8	P_3	"	"	
"	63	" + T_3 + "	P_2+P_3	"	"	
"	64	" + " + R_9	P_3	"	"	
5-6-48	65	C_2 + R_9	P_4	24	"	
"	66	" + "	P_1+P_2+P_3	"	"	

INDEX OF RUNS (Cont.)

Date	Run	Configuration	Test	q_o, $\frac{lb}{ft^2}$	a_g	Remarks
5-6-48	67	C_2	P_1	Vary	"	
"	68	" + R_8	$P_2'+P_3$	24	"	
5-7-48	69	" + T_{11} + R_8	$P_1+P_2+P_3$	"	"	
"	70	" + " + R_9	$P_2'+P_3$	"	"	
"	71	" + T_{12} + "	$P_1+P_2'+P_3$	"	"	
"	72	" + " + R_8	P_2+P_3	"	"	
5-8-48	73	C_3 + R_8	" + "	10	"	
"	74	C_1' + "	$P_2+P_2'+P_3$	80	"	
"	75	" + R_8'	P_3(Vis.)	"	"	

INDEX OF FIGURES

INDEX OF FIGURES (Cont'd)

INDEX OF FIGURES (Cont'd)

INDEX OF FIGURES (Cont'd)

INDEX OF FIGURES (Cont'd)

Page

Static Pressures Around Cylinder C_2

Static Pressures Around Cylinder C_3

INDEX OF FIGURES (Cont'd)

INDEX OF FIGURES (Cont'd)

THEORETICAL (Appendix)

TABLE 1

A. NOMENCLATURE

Definition of Tests

P_1 = Static pressure measurements made on cylinder using cylinder orifices. Measurements were recorded photographically.

P_1(Vis.) = Visual observation and recording of P_1 pressure measurements.

P_2 = Static pressure measurements made at floor and ceiling of test section using flush mounted orifices which were coincident with vertical plane through tunnel centerline. Measurements were indicated on a multimanometer and recorded photographically.

P_2' = P_2 static pressure measurements made visually using a Zahm type precision micromanometer.

P_3 = Static and total head measurements of the wake made using the survey rake. Measurements were indicated on a multimanometer and recorded photographically.

P_3(Vis.) = Visual observation and recording of P_3 pressure measurements.

P_4 = Visual observation and recording of static pressures on cylinder endplate support as indicated on a multimanometer.

Definition of Angular and Linear Measurements

α_g = Angle of attack of horizontal cylinder diameter with zero defined by rotating the cylinder in the windstream until orifice number 1 indicated that it was measuring the forward stagnation pressure. Positive angular displacement occurs when the nose is raised or trailing edge is lowered (as a tunnel observer would see it).

θ = Angular measurement of point on cylinder relative to horizontal radius (when model is at α_g = 0°). See sketch to right.

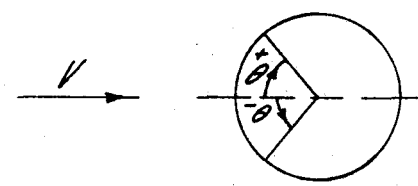

x = Distance from trunnion axis measured in direction parallel to tunnel centerline. Positive value corresponds to downstream direction.

TABLE 1 (Cont'd.)

y = Distance from trunnion axis measured in vertical direction. Positive value corresponds to measurement above trunnion axis.

z = Distance from tunnel centerline measured parallel to trunnion axis (i.e. horizontal). Positive value corresponds to measurement to left (North) of tunnel centerline (observer looking upstream).

d = Diameter of cylinder.

Definition of Coefficients

C_p = Total or static pressure coefficient. Figures on which the scales are labeled C_p have the curves marked so as to identify the pressure coefficient presented.

$$C_p = \frac{P_x - P_{ref.}}{q_o} \quad \text{or} \quad \frac{H_x - P_{ref.}}{q_o}$$

R = Reynolds number = $\frac{\rho d V_o}{\mu}$

Where the foregoing coefficients are associated with the following quantities:

q_o = Dynamic pressure in clear tunnel test section as indicated when using calibrated tunnel piezometer rings. ($\frac{1}{2}\rho V_o^2$ in lb/ft.^{2})

$q = H_x - p_x$ = True dynamic pressure measured in tunnel when model is present ($\frac{1}{2}\rho V^2$ in lb/ft.^{2})

H_x = Total head as indicated by measurements made using the rake.

P_x = Static pressure measurements made at "x" where subscripts used are:

x = denotes location of static pressure orifice as indicated on figures. (i.e. Rake, model, or endplate static orifices)

w = denotes static pressure measurement made on the wall (floor and ceiling) when model is present in tunnel.

TABLE 1 (Cont'd.)

$P_{ref.}$ = Reference static pressure measurement where subscript "ref." may be:

20 ~ denotes static pressure measurements made at the 20 ft. piezometer ring

$3\frac{1}{2}$ ~ denotes static pressure measurements made at the $3\frac{1}{2}$ ft. piezometer ring

o ~ denotes static pressure measurements made at the intersection of the tunnel centerline with the trunnion axis when no model is present

$\mathcal{L}$ ~ denotes static pressure measurements made when no model is present at points on the tunnel centerline other than at intersection with the trunnion axis

w_o ~ denotes static pressure measurements made on the wall (floor and ceiling) when no model is present

V_o = Freestream velocity when no model is present.

V = Local freestream velocity when model is present.

ρ = Mass density of air (note: A correction is applied in the tunnel airspeed calibration so that in the above formulae ρ is to be taken as the free air density unaffected by compressibility.)

μ = Absolute viscosity of air (for T = 15°C., h = 760 mm)

$= 3.726 \times 10^{-7} \frac{\text{lb - wt. x sec}}{\text{ft}^2}$

In addition to the preceding definitions, new definitions are given in the text when they occur in conjunction with derivations, etc.

TABLE 1 (Cont'd.)

B. Notations Used to Describe Configurations Tested

C_1 = Steel cylinder machined and ground to a high polish. Length is 36.0 inches and diameter is 6.598 inches. It is equipped with 20 static pressure orifices made by installing 3/32" O.D. copper tubing flush to the surfaces. Orifices are spaced evenly apart with number 1 orifice being on the leading edge. The orifices were mounted on tunnel centerline in an unstaggered (axially) position.

C_1' = C_1 with static pressure orifices filled in with brass rod. Slight surface irregularities still existed.

C_2 = Steel cylinder similar to C_1 but of 12.613 inch diameter. It is equipped with 36 static pressure orifices mounted in a vertical plane coincident with the tunnel centerline.

C_3 = Steel cylinder similar to C_2 but of 17.338 inch diameter.

R_1 = Standard 80 tube GALCIT traversing total head rake installed so as to make a vertical total head survey 20½ inches aft of the trunnion axis and 6 inches South of tunnel centerline. Rake also equipped with static pressure tubes.

R_2 = Rake mounted 32½ inches aft of the trunnion axis and 6 inches South of tunnel centerline.

R_3 = Rake mounted 44½ inches aft of the trunnion axis and 6 inches South of tunnel centerline.

R_4 = Rake in same axial position as R_1 but mounted 12 inches South of tunnel centerline.

R_5 = Rake in same axial position as R_1 but mounted on tunnel centerline.

R_6 = Rake in same axial position as R_1 but mounted 6 inches North of tunnel centerline.

R_7 = Rake in same axial position as R_1 but mounted 12 inches North of tunnel centerline.

R_8 = Rake mounted 20½ inches aft of trunnion axis. Differs from previous rake notation in that this location allows a complete horizontal traverse in addition to the vertical traverse. Actual position of rake in traverse plane is noted on pressure data.

TABLE 1 (Cont'd.)

R_8' = Rake R_8 with total head tube mounted on outside of static pressure tube mount so as to permit total head measurements to be taken close to the South tunnel wall. (Total head tube was mounted on South side of rake.)

R_8'' = Rake R_8 with total head tube mounted to flanges on North side of rake so as to permit total head survey close to the North wall.

R_9 = Rake mounted 39½ inches aft of trunnion axis. Similar to R_8 in that notation is used to denote rake being used for complete traverse with actual rake position noted on pressure data.

R_9' = Rake R_9 with total head tube mounted as in R_8'' so as to permit total head survey near South wall.

T_1 = 0.041 inch diameter (piano wire) separation strips taped spanwise on model at $\theta = \pm 65°$. Used in conjunction with cylinder C_1.

T_2 = 0.018 inch diameter (piano wire) separation strips taped spanwise on cylinder C_1 at $\theta = \pm 65°$.

T_3 = Separation strips similar to T_2 except taped at $\theta = \pm 85°$.

$T_4 = T_2 + T_3$

T_5 = 0.039 inch diameter (piano wire) separation strips taped spanwise on cylinder C_3 at $\theta = \pm 65°$.

T_6 = 0.0675 inch diameter (welding rod) separation strips taped spanwise on cylinder C_3 at $\theta = \pm 55°$.

T_7 = Separation strips similar to T_6 except taped at $\theta = \pm 85°$.

T_8 = One inch wide chordwise separation strips (sandpaper) mounted on each end of cylinder. Extended around leading edge from $\theta = +100°$ to $\theta = -100°$.

T_9 = 0.0675 inch diameter (welding rod) separation strips taped spanwise on cylinder C_1 at $\theta = \pm 65°$.

T_{10} = Separation strips similar to T_9 but modified such that they only extended to within 2 inches of each wall.

T_{11} = 0.0675 inch diameter (welding rod) separation strips taped spanwise on cylinder C_2 at $\theta = \pm 65°$.

TABLE 1 (Cont'd.)

T_{12} = 0.0675 inch diameter (welding rod) separation strips taped spanwise on cylinder C_2 at $\theta = \pm 65°$ and $\pm 85°$.

S_1 = ½ inch wide cellulose tape strips mounted parallel to chord plane of cylinder C_1 and spaced 3 inches apart across the span.

X_1 = Wax fillet installed at intersection of front side of cylinder C_1 and North tunnel wall.

Clear Tunnel = Test section of wind tunnel devoid of models so as to permit preliminary calibrations of air flow.

I. INTRODUCTION

A comprehensive study was originally proposed to cover the blockage effects resulting from real viscous flow over a body spanning a rectangular test section at flow velocities which are associated with incompressible flow. Blockage effects take the form of solid blockage, wake blockage, and wake buoyancy corrections. The first two corrections arise from the tendency of the solid body and wake to increase the flow velocity in the channel, whereas in free air these velocity increases do not occur. The third correction accounts for the change in buoyancy and acceleration forces of the model when the wake is not in free air.

Knowledge of the incompressible flow blockage effects and corrections to account for them is necessary in order to permit reliable test data to be taken on models whose size with respect to tunnel size is not small, especially since present day trends in low speed wind tunnels are in the direction of increasing the model size in an attempt to bring the Reynolds numbers of the model closer to those of the prototype. Also at high speeds, where compressibility effects become pronounced, small flow perturbation theories such as the Extended Prandtl-Glauert Rule obtain compressible flow blockage corrections by applying a compressibility factor to the incompressible flow corrections. As a result, blockage effects (such as resulting from the wake) that are oftentimes considered negligible in incompressible flow have perceptible values when compressibility factors are taken into account.

The relative magnitudes of the three blockage effects are as follows:

1. The solid blockage correction to velocity in a channel is the most apparent. As a consequence reliable methods have been developed to account for it.
2. The wake blockage correction to velocity in a channel is usually considered negligible in low speed testing of streamlined bodies. As a consequence the development of reliable methods of predicting this correction was not stressed until the advent of high speed testing.
3. The wake buoyancy correction can for all practical purposes be considered as being imperceptible.

The purpose of these investigations is to study blockage effects in two-dimensional channel flow with particular emphasis placed upon obtaining qualitative measurements of wake blockage and its variation along the tunnel axis. The fact that the wake blockage effects are transmitted undiminished in a vertical direction permits the direct measurement to be made at the floor and ceiling walls by means of static pressure orifices. The requirement of large wakes determined the body shape to be tested, namely a bluff body such as a circular cylinder. A. Thom [1] derives an approximate equation for determining the wake blockage directly above an airfoil as a function of the drag coefficient. In addition he points out that the wake blockage correction at the airfoil is one-half of its value far downstream. The correlation of these investigations

with the results of reference 1 would determine the reliability of his approximate equations when applied to exaggerated cases such as encountered in high speed testing. The effects of the wake upon the velocities at the wall are to be correlated with the equation(for an airfoil)

$$\varepsilon_{ww} = \frac{C_D}{4} \cdot \frac{d}{a} \qquad \ldots(1.1)$$

where

ε_{ww} = percentage change in velocity at wall above model due to wake and its images

C_D = uncorrected drag coefficient

d = diameter of cylinder

a = vertical height of tunnel

Three cylinder sizes were selected in order to obtain a pronounced variation of the blockage effects. The ratio of cylinder diameter to tunnel test section height varied between 0.065 and 0.175. The corresponding variation of the cylinder length to diameter ratio was between 5.45 and 2.85. Solid blockage variations were obtained by varying the cylinder size while maintaining a constant Reynolds number. The value of Reynolds number was chosen such that the corresponding range of tunnel velocities could be reliably set. Preliminary calculations showed that this value of Reynolds number corresponded to a turbulent type of flow separation. The wake blockage effects were to be varied independently of solid blockage effects by inducing the flow separation point to move forward on the cylinder. This forward movement of the flow separation point was to be attained by means of wire strips taped to the aft portion of

the cylinder ahead of the flow separation point as previously determined on the clean cylinder.

An axial row of flush orifices at the cylinder midspan was employed to measure the surface static pressures. The decision to use a row of orifices, instead of rotating the cylinder with only one orifice, was based upon the necessity of recording a large amount of data in an allotted test period. Past experience had shown that an axial row of orifices on an airfoil resulted in only a local departure of the flow from being two-dimensional and that wake measurements made downstream of the airfoil indicated uniform two-dimensional flow except in a narrow region influenced by the orifices. Therefore, it was expected that two-dimensional flow would be encountered over the cylinder except in a region near to the plane of the orifices, and that the wake pattern would be essentially two-dimensional.

Past experience with airfoils had also shown that a slight distortion of the flow field should be expected in the region near the vertical walls because of interference caused by the velocity gradient through the wall boundary layer. The test program outlined prior to the actual test period took into account these expected interference difficulties.

When actual testing on the cylinders began, it became apparent that the expected effects* were underestimated and that nowhere in the

* A survey of available literature [2,3] indicated that these effects would be encountered and that they would be pronounced, but not that they would be of the order of magnitude encountered here.

wake behind the cylinders did there exist any semblance of a two-dimensional flow pattern. Attempts were made to avoid the uncertain interference effects of the orifices, but little success was achieved by any method that attempted to cover the orifices at the surface. An example of an incident that occurred helps to illustrate the difficulties encountered. A visual survey of the total head losses in the wake made late one afternoon happened to be repeated on the following morning. Comparison of the data indicated that the total head losses had markedly increased in a certain region of the wake. Close inspection of the cylinder surface ahead of this region disclosed the fact that a fingerprint left accidentally on the forward portion of the cylinder had caused an almost imperceptible amount of surface corrosion during the night. Repolishing of the corroded region with crocus cloth and kerosene followed by a cleansing of the surface with alcohol permitted the taking of total head loss measurements that were in agreement with the previous days results. This extreme sensitivity of the flow over the circular cylinders to surface irregularities was unexpected, experience with airfoil sections with metallic surfaces having indicated less severe tendencies in that regard.

The original purpose of the test could not be completely carried out after the three-dimensional flow patterns over the cylinders were noted. The test program was of necessity modified and became an investigation of methods of avoiding the three-dimensional flow over circular cylinders caused by interference effects from the

vertical walls, model orifices, and small surface irregularities. Reasonable success was achieved in adjusting the flow pattern in order to obtain two-dimensional flow. This was accomplished when the point of flow separation on the cylinder was made approximately uniform across the span by means of separation wires taped to the cylinder in the region ahead of the maximum thickness point (between $\theta = \pm 65^{\circ}$ and $\pm 85^{\circ}$). The width of the wake could be varied by varying the exact location of these wire strips. The experimental results are presented in sections IV-A and B.

After the attainment of approximately a two-dimensional flow pattern, it was possible to realize a portion of the original purpose of the investigation. A study of the wall pressure measurements is presented in Section IV-C. From these wall pressure measurements are obtained the experimental values of wake blockage along the tunnel axis. A correlation is made between the experimental and predicted [1] values of wake blockage for the cylinder configurations that are applicable.

A complete outline of the tests may be found in the Index of Runs, and the definition of model configurations and test nomenclature may be found in Table 1. The experimental setup is described in Section II. Section III describes the method of data reduction and presentation.

II. DESCRIPTION OF TEST SETUP AND FLOW CALIBRATIONS

A. Test Equipment

The experiments presented herein were conducted in the GALCIT two-dimensional tunnel, which consists of a two-dimensional working section installed inside the throat of the normal GALCIT ten-foot wind tunnel (cf. Fig. II-1). Two-dimensional models are mounted horizontally across the tunnel between turntables in the vertical working section walls. The working section is three feet wide, ten feet long, and eight and one-half feet high. The contraction ratio is approximately 12½ to 1 as compared to the ratio of 4 to 1 for the normal ten-foot tunnel. At its upstream end the rectangular working section is faired smoothly into the contraction cone of the ten-foot tunnel. Downstream of the working section the flow is expanded in an "eight degree"* diffuser as far as the first corner vanes. At this point vertical Frey deflector vanes are installed to guide the air flow out to the normal tunnel walls. Between the working section and diffuser there is a two-foot breather gap where an arrangement of vanes help to guide the air flow and prevent flow oscillations. In the twenty foot section of the normal tunnel far upstream of the contraction cone are installed five 30 x 30 mesh, phosphor-bronze, wire screens. These, combined with the high contraction ratio, tend to reduce the turbulence level of the tunnel air stream to an extremely small value. Tests with a hot wire anemometer have

---

* The rate of area expansion is equivalent to that of an eight degree cone.

indicated that the turbulence level (root mean square of the ratio of velocity fluctuations to velocity) was 0.08% parallel and 0.12% perpendicular to the flow direction.

The models tested were three cylinders of 36.0 inch span and of 6.598,12.613, and 17.838 inch diameter respectively. The cylinders were finished to a high polish. They were finished on a centerless grinder in order to assure their being circular about their original center. They were mounted on the tunnel centerline between the turntables (endplates) in the vertical walls (cf. Fig. II-2). Angle of attack adjustments were made by rotating the turntables. The models were equipped with a chordwise row of flush static pressure orifices in the midspan, and the pressures as indicated by these orifices were transmitted through long rubber tubing leads that were brought out from the model along the axis of rotation. These pressure leads were connected to a multimanometer beneath the test section, and the pressures as measured by the model orifices were available at all times on the multimanometer for either visual or photographic recording.

A wake survey rake was used in order to measure the wakes behind the cylinders. It was mounted on a special frame at the downstream end of the working section. Horizontal (spanwise) and vertical lead screws driven from outside the working section permitted variation of the rake position in the tunnel. Preset counters on the lead screws indicated the rake position in the tunnel. The survey plane was adjusted fore and aft by means of sliding clamps which secured the rake support beam to the frame. The rake consisted of 80 total head tubes spaced 0.1 inch apart and 5 static pressure tubes mounted

on the side and spaced vertically in a manner to measure the static pressure variation in the region of the total head tubes. The total head tubes were constructed of hypodermic needles partially flattened at the upstream end. The pressures as indicated by the wake rake were transmitted through rubber tubing to a multimanometer set up under the tunnel test section. They were recorded either visually or photographically.

Thirty-eight static pressure orifices spaced six inches apart on the floor and ceiling of the working section in a vertical plane through the tunnel axis were employed to measure the horizontal wall static pressures. They were connected by means of rubber tubing to a third multimanometer beneath the tunnel working section in order to permit remote measurement of the pressures. Accurate measurements of the floor and ceiling pressures in the region above and below the models were made by connecting the pressure leads in parallel to a precision micromanometer.

The turntable on the North side of the tunnel was equipped with twenty-seven flush static pressure orifices (cf. Fig. II-3). These orifices were also connected to a multimanometer beneath the test section by means of long rubber tubing. The orifices were read visually during only a few runs of the test, and during the remainder of the test the pressure leads were disconnected and clamped shut.

B. PRELIMINARY FLOW CALIBRATIONS

The dynamic pressure in the two-dimensional test section was determined during the tunnel calibration by mounting a standard Prandtl pitot-static tube on the tunnel centerline at the trunnion axis. The pressure difference between the static pressure in the 20-foot entrance section and the static pressure at the entrance ($3\frac{1}{2}$-foot) section was determined at the same time that the dynamic pressure was measured. These "calibrated" static pressures were used to set the dynamic pressure on all tests. Fig. II-4 presents the results of these calibrations in the form of the dynamic pressure q_o versus the ratio of dynamic pressure q_o to the static pressure difference h between the two piezometer orifice stations. A correction was applied to the dynamic pressure readings as obtained by the Prandtl pitot-static tube to account for the compressibility effect upon the air density.

In accordance with the purpose of these tests, no corrections were applied when setting the dynamic pressure to account for the blocking effects of the models or their wakes.

Figs. II-5 and II-6 present results of the preliminary flow calibrations made when no model was present in the tunnel test section. They show the static pressure coefficient variations along the tunnel axis, and in the horizontal and vertical directions perpendicular to the tunnel axis at the trunnion station. It will be noted on Fig. II-5 that the static pressure coefficient along the tunnel axis is constant in the region from 17 inches forward to 25 inches aft

of the trunnion axis for the clear tunnel configuration. Figure II-7 presents results of static pressure measurements made over the floor and ceiling when no model was present in the test section. These data are employed in the floor and ceiling data reduction.

The static pressures read by the static tubes on the rake were calibrated in order to correct for instrument error. The static pressure errors as a function of dynamic pressure q_o are presented on Fig. II-8 for four static tubes. The fifth static tube was faulty and therefore could not be relied upon. The calibration of these static tubes was made in a region of constant static pressure, whereas in actual practice the static tubes read static pressures in the model wakes. The existence of static pressure gradients in the model wake introduces another source of error in the static tube reading since the reading of the static pressure as measured on the multimanometer does not necessarily correspond to the static pressure at the tube centerline. The temporal fluctuations of the wake patterns were large and precluded the necessity of applying a tube displacement correction.

III. METHOD OF EXPERIMENTAL PRESENTATION

All data presented herein are normalized in a manner such that the terms are dimensionless. Length terms (i.e. coordinates) are normalized with respect to the cylinder diameter. The coordinate system used is indicated in the sketch. Pressures are normalized with respect to the dynamic pressure q_o which is the dynamic pressure at the intersection of the tunnel axis and the trunnion axis when no model is present. In addition to being normalized with respect to dynamic pressure q_o, the pressure coefficients are referred to the pressures which are associated best with the data presentation. Velocities are normalized with respect to V_o which is the velocity at the intersection of the tunnel axis and the trunnion axis when no model is present.

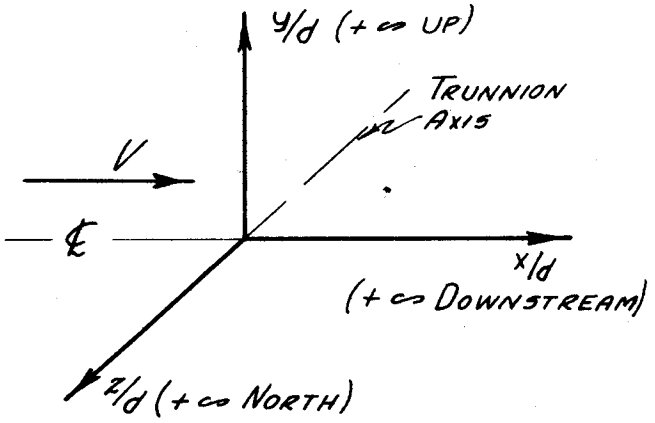

A. WAKE SURVEYS

The bulk of the data recorded during the test were pressure measurements obtained with the wake survey rake. A description of the wake survey rake is presented in section II-A. The large wake widths being observed necessitated an overlapping of wake pattern measurements since in many cases the total head tubes on the rake could not completely span the wake. It was necessary to take several

photographic records at each rake setting in order to average out wake fluctuations.

The data are presented on the figures in sections IV-A in two ways as follows:

1. Figures showing the wake patterns present the total head and static pressure coefficients as a function of the dimensionless vertical coordinate (y/d), while the horizontal and axial dimensionless coordinates are held constant. The two pressure coefficients are referred to the same reference pressure and have the form of $\frac{H - P_{20}}{q_0}$ and $\frac{P_x - P_{20}}{q_0}$. The difference between the two curves at any y/d coordinate gives the ratio of local dynamic pressure to clear tunnel dynamic pressure. These figures also show a reference pressure coefficient line $\left(\frac{P_\ell - P_{20}}{q_0} \right)$ which makes readily apparent the change in local static pressure.

2. Figures showing the contours of constant static or total head coefficient decrements also are presented. These figures are the results of crossplotting the data in the wake pattern group mentioned above. The contours appear as lines in the survey plane a constant distance behind the cylinder.

The data, as is evident from the actual figures, are subject to appreciable experimental scatter. The total head pressure data are subject to the most scatter near the point of maximum total head loss. At this point variations in pressure coefficient of 0.1 are common. The static pressure data are also subject to this amount of

scatter, depending upon the model configuration. The static pressure data for cylinders with separation stripe are unreliable and in these cases no fairing of the points is attempted. The fairing of static pressure data is not as trustworthy as the total head fairing because of the small number of pressure tubes on the wake rake.

B. PRESSURE SURVEYS AROUND CYLINDERS

Data indicating the static pressures around the cylinders were obtained from static orifices distributed in a chordwise plane at the model midspan and from static orifices distributed over the surface of the North endplate. A description of the equipment setup is given in section II-A. All static pressure data for this group are presented in the form of dimensionless pressure coefficients and are referred to the static pressure at the intersection of the tunnel and trunnion axes (i.e. $\frac{p-p_o}{q_o}$).

The static pressure data obtained from the model orifices are employed to determine the pressure drag coefficient. The equation used in determining the pressure drag coefficient is:

$$C_D = \int_{-1/2}^{+1/2} \left[\left(\frac{p_f - p_o}{q_o} \right) - \left(\frac{p_r - p_o}{q_o} \right) \right] d\left(\frac{y}{d} \right) \qquad \ldots(3.2)$$

where

p_f = static pressure on front face of cylinder

p_r = static pressure on rear face of cylinder

C_D = pressure drag coefficient

The data are presented in section IV-B in the three following ways:

1. Figures are presented showing the variation of static pressure coefficient as a function of the cylinder angle Θ. The variation of static pressure coefficient for the perfect fluid case is shown on these figures by a dashed curve.

2. The results of pressure measurements over the endplates are shown by means of constant static pressure coefficient

contours in the plane of the endplate.

3. Curves are presented showing the variation of pressure drag coefficient with Reynolds number. These data were obtained when the model had no separation strips. Data for the models with separation strips were obtained at fixed Reynolds numbers; the pressure drag coefficients computed from these data are presented on the figures as plotted points only.

C. FLOOR AND CEILING PRESSURE DATA

The floor and ceiling pressure data were obtained from two types of manometers, namely a multimanometer and a precision micromanometer. A description of the equipment setup is presented in section II-A. The data obtained from the multimanometer are used to describe the nature of the pressure variation, while the data from the micromanometer are used to accurately determine the pressure levels. By this method, a reliable pattern of the static pressure variation along the floor and ceiling walls is obtained. Since the floor and ceiling wall data are presumably symmetric about the tunnel axis and since all the changes in tunnel flow result from configuration changes that are symmetric about the tunnel axis, the floor and ceiling static pressure variations are averaged to give a mean value for the effects at the walls.

The average change in floor and ceiling static pressure coefficient as a function of the normalized longitudinal axis coordinate (x/d) is presented in the figures of section IV-C. The pressure coefficient is in the form of $\frac{p_w - p_{wo}}{q_o}$, where p_w is the static pressure at the wall when a model is present, and p_{wo} is the static pressure at the wall when no model is present in the tunnel. For sake of convenience the perturbation velocities instead of the static pressures at the wall are presented for a few cases.

The perturbation velocities may be obtained readily by considering the incompressible form of the energy equation. The

relation between the perturbation velocity and the wall static pressure is:

$$\frac{u_w}{V_o} - 1 = \sqrt{1 - \frac{p_w - p_{wo}}{q_o}} \qquad \ldots(3.3)$$

where

u_w = velocity at wall in axial direction

IV. DISCUSSION

A. Study of Wake

Presented in this section are the results of static and total head pressure measurements made while surveying the wake behind the cylinders with the GALCIT 80 tube traversing rake.

Figures IV-1 and 2, 16 and 18, and 32 present the contours of constant total head decrements aft of cylinders C_1, C_2 and C_3 respectively in survey planes behind the cylinders. All linear dimensions are normalized with respect to the cylinder diameter. It can be noted on these figures that the contours do not correspond to two-dimensional flow. Distinct regions are visible on these figures which may be associated with interference effects from the vertical walls and the model orifices at the midspan. Comparison of Figures IV-1 and 18, which apply to cylinders C_1 and C_2 respectively in a survey plane approximately 3.1 diameters behind the cylinder axis, shows that the wall interference effects extend over a region in the spanwise direction of about 1 cylinder diameter. Also it can be noted that the total head decrement contours are very similar and of approximately the same magnitude on these two figures.

Attempts were made with cylinder C_1 to minimize the effects of the orifices at the midspan by closing the orifices. The various methods employed were to fill the orifices in with wax and make the surface uniform, tape the orifices closed with cellulose tape, and carefully plug the orifices with brass rods. Figures IV-3 to 14 show the wake patterns at 3.1 diameters behind the cylinder axis at three spanwise stations for the cases of cylinder with orifices

open, filled with wax, taped, and plugged. It can be noted from these figures that the effects of the orifices upon the wake patterns could not be eliminated completely, and even if they were, the wall interference effects still would be present.

Reasonable success in obtaining a two-dimensional wake pattern was obtained by fastening wire separation strips in a spanwise direction on the top and bottom surfaces in the region between $\theta = \pm 65^{\circ}$ and $\pm 85^{\circ}$, which is just forward of the point of maximum thickness. Figure IV-15 shows the improvement in the wake pattern aft of cylinder C_1 and from this figure it can be seen that both wall and orifice interferences were made less important when the separation point was fixed fairly uniformly across the span by means of these separation wires. Figures IV-20 to 31 are concerned with the wake patterns and contours of total and static head decrement aft of cylinder C_2 with separation strips T_{11} and T_{12} (0.0675 inch diameter welding rods taped to the cylinder surface at $\theta = \pm 65^{\circ}$, and $\theta = \pm 65^{\circ}$ and $\pm 85^{\circ}$ respectively). From these figures it can be seen again that the wake patterns approximately resemble two-dimensional flow characteristics and that the wake width could be varied by varying the location of the separation strips.

B. STUDY OF STATIC PRESSURES AROUND CYLINDERS

This section presents the results of pressure investigations conducted in the vicinity of the circular cylinders employing flush mounted static pressure orifices at the midspan and the North support endplate. The cylinders were rotated in the airflow until orifice number 1 at the midspan indicated the stagnation pressure and the pressure patterns as measured by the orifices on the top and bottom surfaces of the cylinder were symmetrical. By visually observing the static pressure distribution while rotating the cylinder a rapid and precise method of model orifice alignment relative to the windstream was attained. Figure IV-37 presents the static pressure distribution over the small cylinder (C_1) when the orifices are rotated -4.37° from the observed symmetrical pressure pattern. As can be seen on the figure, the pressure measurements over the cylinder show a consistent and symmetrical pattern after they are corrected for orifice misalignment (tagged symbols denote lower surface).

As indicated in the introduction, the effects of the orifices upon the flow over the cylinders is similar to that arising from irregularities on the surface. It is doubtful, therefore, whether the orifices measured a flow pattern corresponding to true two-dimensional flow. For this reason, the pressure data are interpreted as being of a qualitative rather than of a quantitative nature.

It was expected prior to the test that the critical range of Reynolds number, in which range the flow separation point markedly moves aft in accord with the change from a laminar to a turbulent

type of wake formation, would be between 3.0 and 3.5 x 10^5. For the case of cylinders without separation stripe, pressure measurements were made for a range of Reynolds numbers from below to well above the expected critical range. These measurements indicated the existence of a range of Reynolds numbers between 3.5 and 4.0 x 10^5 in which range the separation point markedly moved aft on the cylinders. The bulk of the data taken were at Reynolds numbers between 8.4 and 8.9 x 10^5.

The effects of variation in Reynolds number (dynamic pressure) upon the measured static pressure distributions at the cylinder midspan are presented on Figures IV-33 to 37, 42 to 45, and 48 to 51 for cylinders C_1, C_2, and C_9 respectively. General characteristics to be noted are:

1. The point of flow separation moves aft on the three cylinders as the Reynolds number passes through the range of values between 3.5 and 4.0 x 10^5, and past this range of Reynolds numbers the separation point remains relatively constant.
2. A pronounced rise in the static pressure occurs on the aft separated portion of the cylinder as the Reynolds numbers goes through the previously mentioned range of values.
3. The measured static pressures over the front portion of the cylinders at Reynolds numbers greater than 4.0 x 10^5 are close to being in agreement with values determined by potential flow theory.
4. The peak negative value of static pressure coefficient increases markedly as the Reynolds number is brought above

the previously mentioned range of values.

5. The peak negative value of static pressure coefficient (based upon the apparent dynamic pressure) increases with cylinder size. This is in accord with fact that solid and wake blockage effects are increasing with cylinder size.

The effects upon static pressure measurements of taping spanwise separation wires to the top and bottom surfaces of the cylinders in the region forward of the maximum thickness are presented in Figures IV-39 to 41, 46 and 47, and 52 to 53 for cylinders C_1, C_2 and C_3 respectively. General characteristics to be noted from these figures are that as the separation stripe moved forward on the cylinder, the flow separation point moved forward and increased the wake size. Figures IV-38 and 39 relate to measurements made on cylinder C_1 (diameter = 6.598 inches) with piano wire separation stripe T_1 and T_2 (0.041 and 0.018 inch diameter respectively) placed at $\Theta = \pm 65^\circ$. This variation of wire size has negligible effects upon the point of flow separation.

Figure IV-55 presents the contours of constant static pressure coefficient in a plane normal to the cylinder axis when the fluid medium is inviscid and the flow is irrotational. These contours were determined by means of potential flow theory. This figure is presented in this section because the two following figures deal with endplate static pressure measurements and are presented in an analogous manner. Figures IV-56 and 57 present the contours of constant static pressure at the North endplate. These figures are consistent with expectations that the flow pattern in the immediate vicinity

of the vertical walls would be influenced by the slower moving air in the wall boundary layer. The static pressure contours indicate a more negative static pressure on the aft separated portion of the cylinder at the wall than at the cylinder midspan. The wake rake measurements in section IV-A indicate the magnitude of these wall effects in a spanwise direction and show that if the linear dimensions are normalized with respect to cylinder diameter, these effects are approximately the same for all cylinders. Figure IV-56 presents the wall static pressure contours for cylinders C_1 and C_2 using a dimensionless coordinate system, and it can be seen that the static pressure contours are identical within the limits of experimental accuracy. Figure IV-57 presents the static pressure contours for cylinder C_1 with separation strips T_{10} and shows that a forward movement of the flow separation point is induced by the separation strips.

Figure IV-58 presents the effects of Reynolds number upon the pressure drag coefficient for cylinder C_1. The pressure drag coefficient is defined by equation 3.2 in section III-B and is uncorrected for blockage effects or for possible interference effects of the orifices upon their measurements. Also presented on this figure is the rise in pressure drag coefficient resulting from the addition of separation strips to cylinder C_1 while operating at a Reynolds number of 9×10^5.

C. STUDY OF FLOOR AND CEILING PRESSURES

This section presents the results of static pressure measurements made over the floor and ceiling of the test section. Figures IV-59 to 61 apply to cylinders C_1, C_2, and C_3 respectively both with and without separation wires. The general characteristics to be noted are as follows:

1. The addition of separation wires to the surface of the cylinders caused the static pressure coefficient to decrease, especially in the region aft of the cylinder.
2. The change in wall pressure coefficient tends to be zero in the region forward of the cylinder for all cases. This is in accord with the expectation that blockage effects would become negligible upstream of the models.
3. The change in wall pressure coefficient does not tend to become zero downstream of the cylinder. This is in accord with fact that the effects of wake blockage should be perceptible downstream of the model.

The floor and ceiling static pressure measurements may be put into the form of velocity perturbations. These velocity perturbations are a result of the solid and wake blockage effects. The velocity change at the walls as a result of wake blockage effects is obtained by subtracting the theoretical solid blockage component from the measured velocity perturbations. Note that the blockage corrections at the wall include the effects of the model and its images outside the tunnel.

In accord with the original purpose of these investigations, a correlation is made between the experimentally determined and the predicted [1] values of wake blockage. Reference 1 presents the wake blockage correction to velocity at a tunnel station corresponding to the model axis, and since this correction is constant in a vertical direction, the predicted blockage correction may be compared with the value as obtained experimentally at the walls. The equation that predicts the wake blockage is a function of the uncorrected drag coefficient, which form is desirable since the wake correction would be expected to increase with drag. The equation with which comparison is to be made indirectly is presented in the Introduction and is:

$$\varepsilon_{ww} = \frac{C_D}{4} \cdot \frac{d}{a} \qquad \ldots(1.1)$$

Reference 1 also suggests a modification to this equation, which for the case of a circular cylinder is not negligible and hence is used herein. The modified equation is:

$$\varepsilon_{ww} = C_D \frac{d}{a} \left[\frac{1}{4} + \frac{3}{16} \left(\mu \frac{d}{a} \right)^{1/2} - \frac{\pi}{36} \cdot \frac{d}{a} \right] \qquad \ldots(1.1a)$$

where ε_{ww} = blockage due to wake and its images at wall ($x/d = 0$)

C_D = drag coefficient

d = cylinder diameter

a = tunnel height

μ = body shape parameter

= 10 (as suggested by reference 1)

In these investigations the total drag coefficient is unknown for the circular cylinders; therefore a pressure drag coefficient will be employed in equation 1.1a. The determination of total drag by considering the momentum defects [4] as indicated by the wake data could not be made since the static pressure variation in a vertical direction behind the model was not known accurately. In addition the approximations assumed in obtaining the drag force from wake measurements no longer apply when the wake blockage is perceptible.

The correlation is made only for those cases where sufficient data are available, namely for those configurations in which data are available for the circular cylinder with separation strips at two or more locations. No correlation is being made for the cases of cylinders without separation strips since wake measurements indicated a three-dimensional flow pattern for those cases.

Table 2

Configuration	$(\frac{u}{U})_w - 1$	ε_{sw}	ε_{ww} (EXPT.)	C_D (EXPT.)	$\varepsilon_{ww}^{(1)}$
$C_1 + T_3$ (a)	0.0226	0.0095	0.0131	0.445	0.0130
$C_1 + T_4$ (b)	0.0287	"	0.0192	0.740	0.0189
(b) ÷ (a)			1.47		1.45
$C_2 + T_{11}$ (c)	0.065	0.038	0.027	0.550	0.031
$C_2 + T_{12}$ (d)	0.076	"	0.038	1.139	0.063
(d) ÷ (c)			1.41		2.03

In Table 2, the column headings are:

$(\frac{u}{U})_w - 1$ = change in velocity at wall (x/d = 0)

ε_{sw} = change in velocity at wall due to solid blockage effects of model and images (x/d = 0)

$\varepsilon_{ww(EXPT.)} = (\frac{u}{U})_w - 1 - \varepsilon_{sw}$

C_D = experimental determination of pressure drag coefficient

$\varepsilon_{ww}^{(1)}$ = calculated wake blockage at wall (x/d = 0) from equation 1.1a

It will be noted in Table 2 that good correlation between experimental and theoretical values of wake blockage were obtained in the case of the small cylinder, C_1. Reasonable correlation is shown in only one of the two cases available for the larger cylinder, C_2; the reason for the discrepancy in the second case is unknown. It is unfortunate that only four of the approximate dozen cases originally contemplated could be investigated, making it impossible to draw conclusions from the results. The results seem to indicate, however, that the theory is satisfactory if the wakes are not too large. Hence the theory seems to be satisfactory for airfoils; because an airfoil with, say, the same volume and hence the same solid blockage of the small cylinder C_1 would have a much smaller wake, below the stall, than has the cylinder C_1.

The floor-ceiling pressures at the downstream end of the test section often approximate with sufficient accuracy the wake blockage effects at infinity. This is particularly true for airfoils, for which a single source placed at the trailing edge is a first approximation

to wake effects [5]. This would have provided a means of checking the ratio of wake blockage at the model to that at infinity, as given by theory, had it held true for the cylinders as well. However, for the large wakes obtained from cylinders, a single source representation is not adequate. In Appendix A, following the general method of reference 1, it is shown that a more complicated array of sources and sinks can be used behind a cylinder to give adequate representation of its effects as measured at the walls. However, this array approaches too closely to the end of the test section for conditions at infinity to be adequately represented there. These calculations showed that it was necessary to place four singularities downstream of the cylinder in order to obtain a reasonable matching of the experimental curves. Figures IV-62 and 63 show the agreement obtained when the sources and sinks were arbitrarily placed at four downstream stations. The perturbation velocities as measured at the wall are presented in addition to the separate contributions of solid and wake blockage velocities.

V. SUMMARY OF RESULTS

The more important results of the test are summarized below:

1. The sensitivity of the flow over circular cylinders to surface irregularities is quite pronounced.
2. The interference effects arising from the endplates supporting the circular cylinders in the two-dimensional test section are also quite pronounced, and influence the flow some distance from the vertical walls.
3. The aforementioned interferences may be circumvented when the point of flow separation over the aft portion of the circular cylinders is made uniform in a spanwise direction. Devices such as separation strips fastened to the cylinder forward of the point of maximum thickness promote this uniformity and provide an essentially two-dimensional wake pattern.
4. Good correlation with two experimental results was obtained when the wake blockage corrections were determined by the method of reference 1 for the condition of small sized cylinder (C_1) with separation strips. The correlation of two other results with a larger cylinder (C_2) were fair to poor. While no conclusions may be drawn from these four results, it is indicated that the simple theory of wake blockage is adequate when applied to the smaller wakes normally obtained with airfoils.

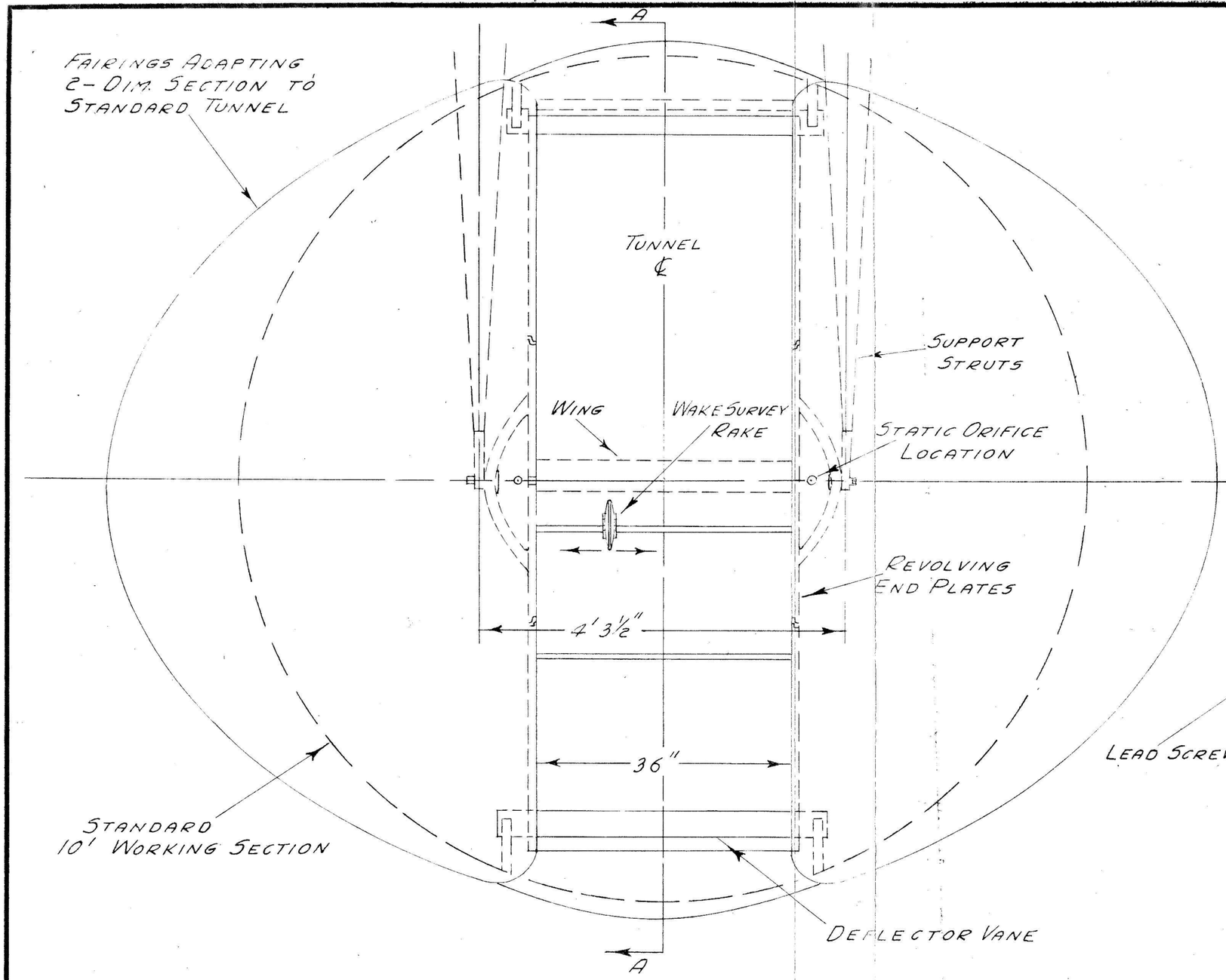

DOWNSTREAM VIEW

SKETCH SHOWING TWO-DIMENSIONAL WORKING SECTION

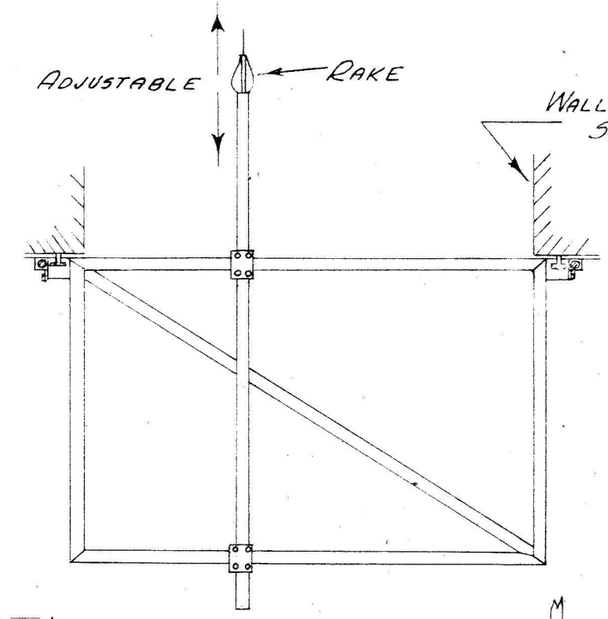

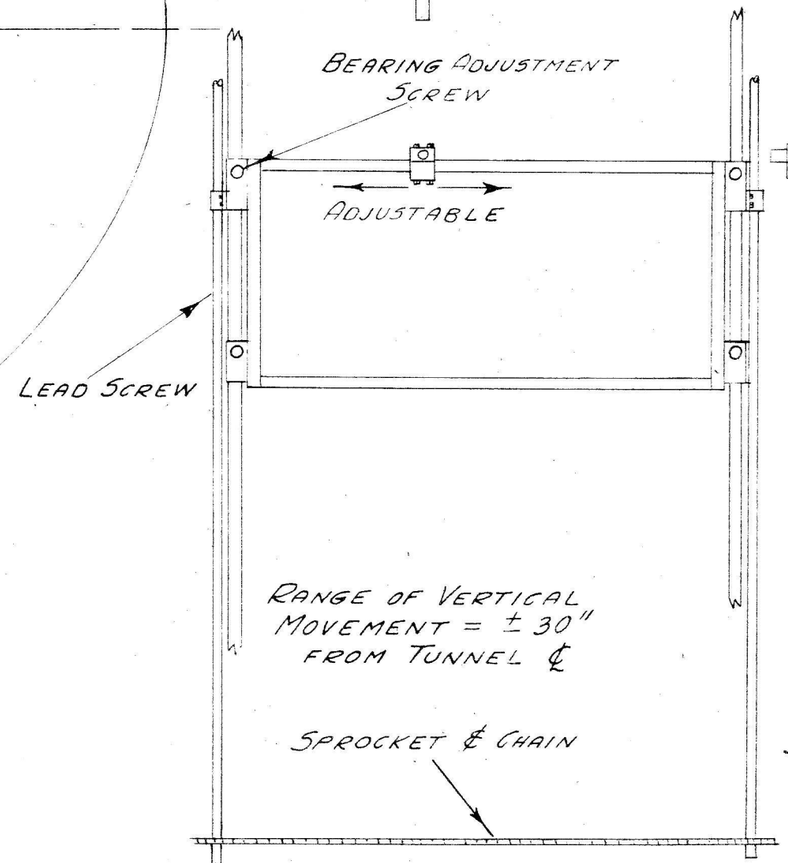

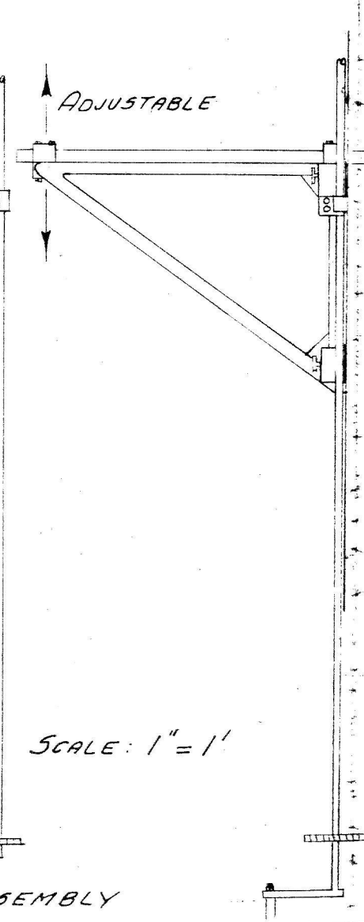

SCALE: 1" = 1'

RAKE FRAME ASSEMBLY

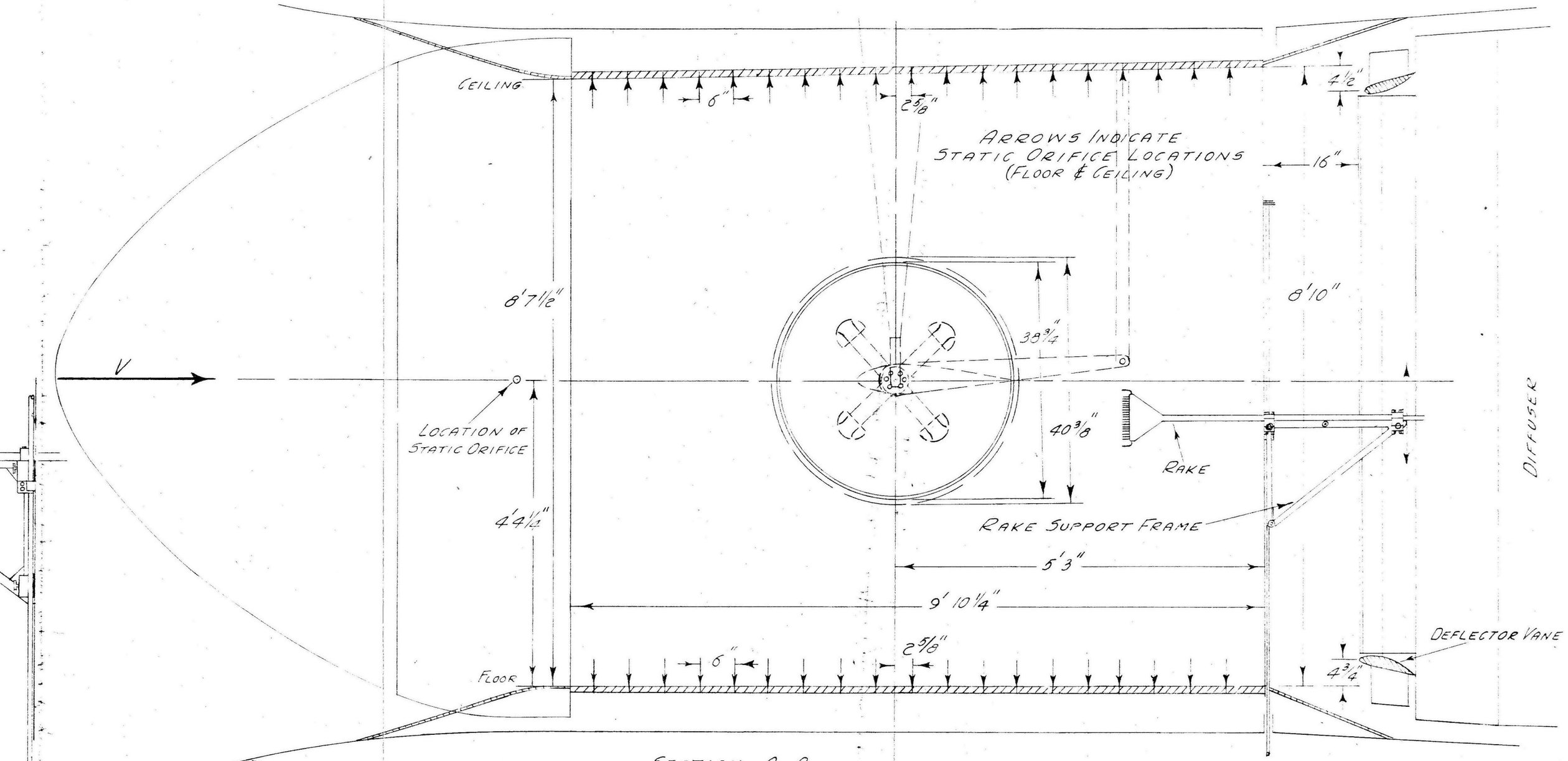

SECTION A-A

REF. GALCIT DWG.
5-253-4
-6

			8/5/48				TOLERANCES ± .010 OR ± .4 UNLESS OTHERWISE NOTED
			Ki FROM F.HF 9/22/42				SCALE: 3/4" = 1" AND NOTED
MATERIAL	FINISH	HEAT TREAT	DRAFTSMAN	CHECKED	APPROVED	ENGINEER	
GUGGENHEIM AERONAUTICAL LABORATORY CALIFORNIA INSTITUTE OF TECHNOLOGY			GALCIT TWO-DIMENSIONAL TUNNEL				
			NAME				DRAWING NO.

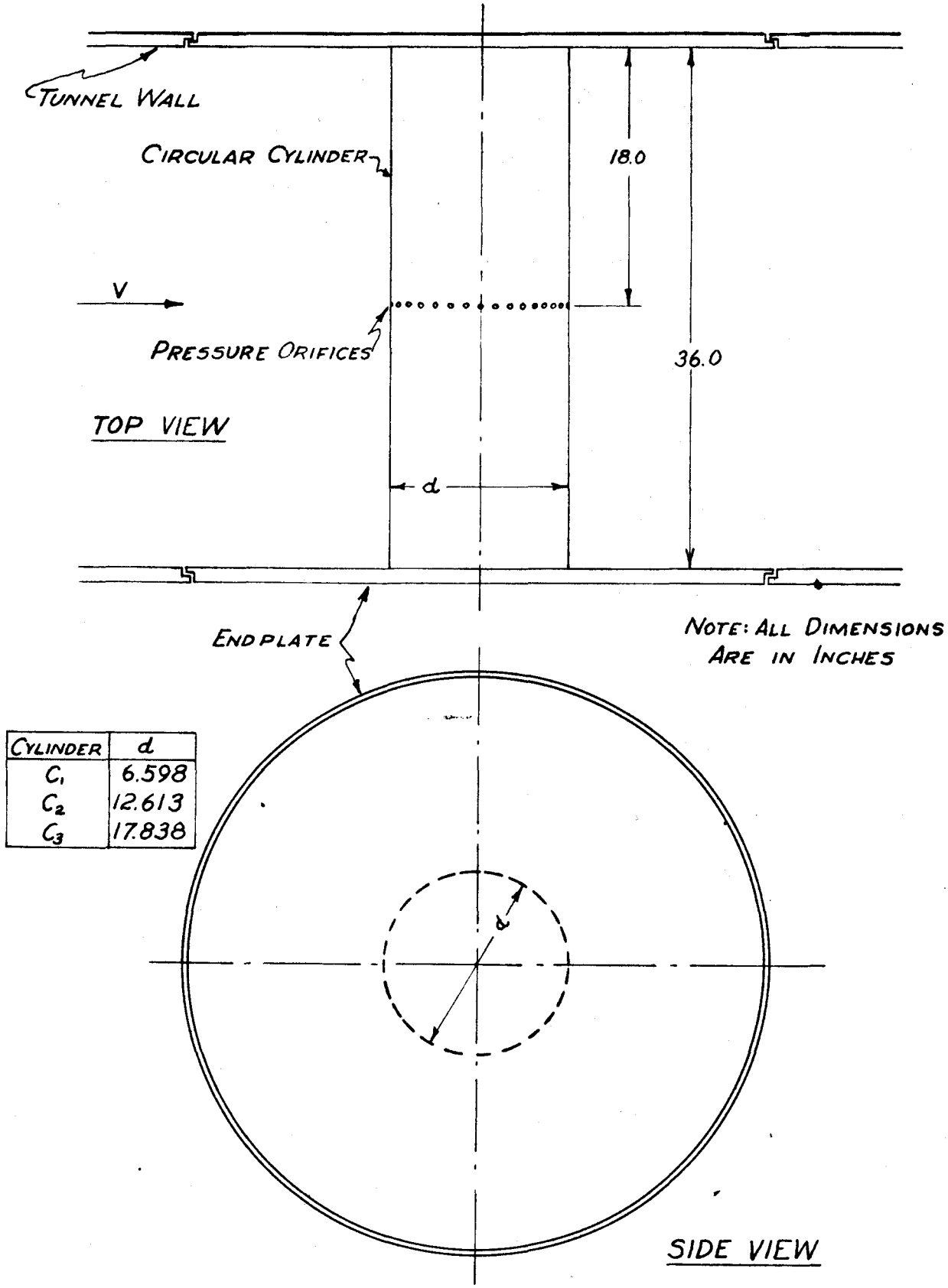

Fig. II-2 Sketch of Circular Cylinders

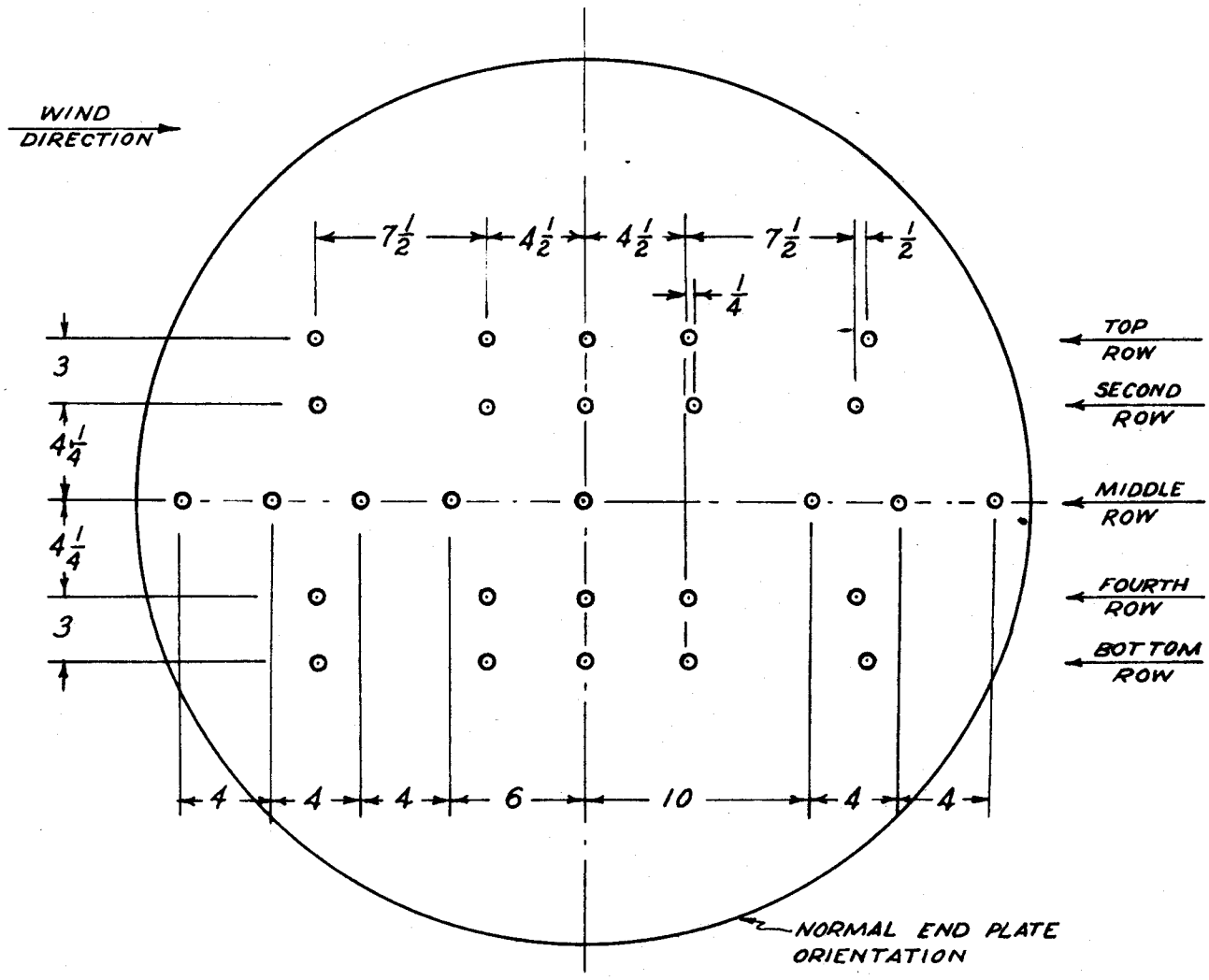

Fig. II-3 Sketch Showing Endplate Orifice Locations

PAGE
FIG.

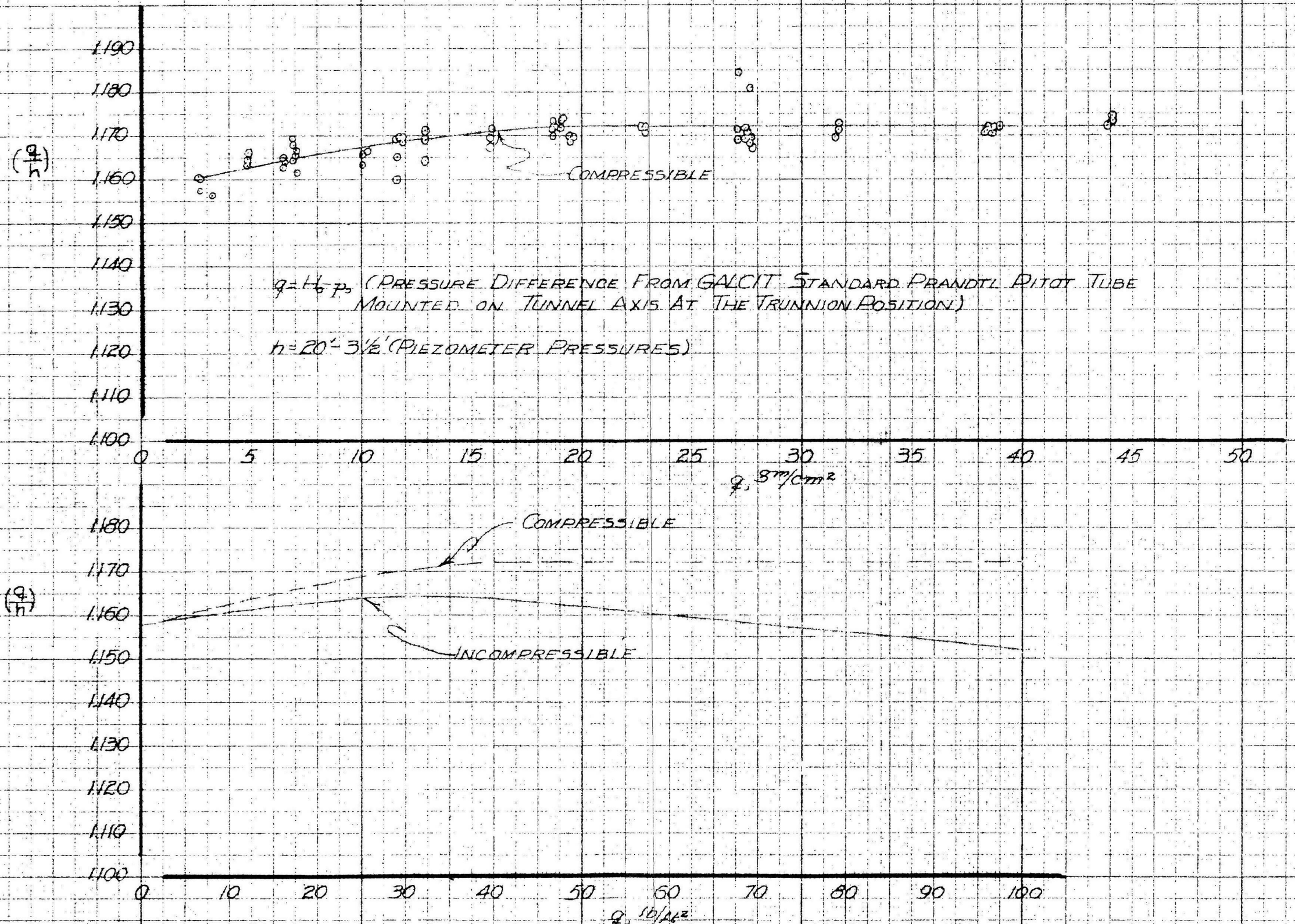

6-BLADED FAN, LONG DIFFUSER, TUNNEL WIDTH = 36.0", HEIGHT = 9.5'

FIG. II-4 TWO-DIMENSIONAL TUNNEL VELOCITY CALIBRATION
CALIBRATED 2-26-48

H_0 & p_3 = PITOT TUBE PRESSURES, PITOT ON TUNNEL AXIS AT TRUNNIONS

$\frac{q}{q_{INC}} = \frac{H_0 - p_0}{1+\delta}$ WHERE $1+\delta$ IS COMPRESSIBILITY CORRECTION

$p_{\mathcal{L}}$ = STATIC PRESSURE ALONG TUNNEL AXIS

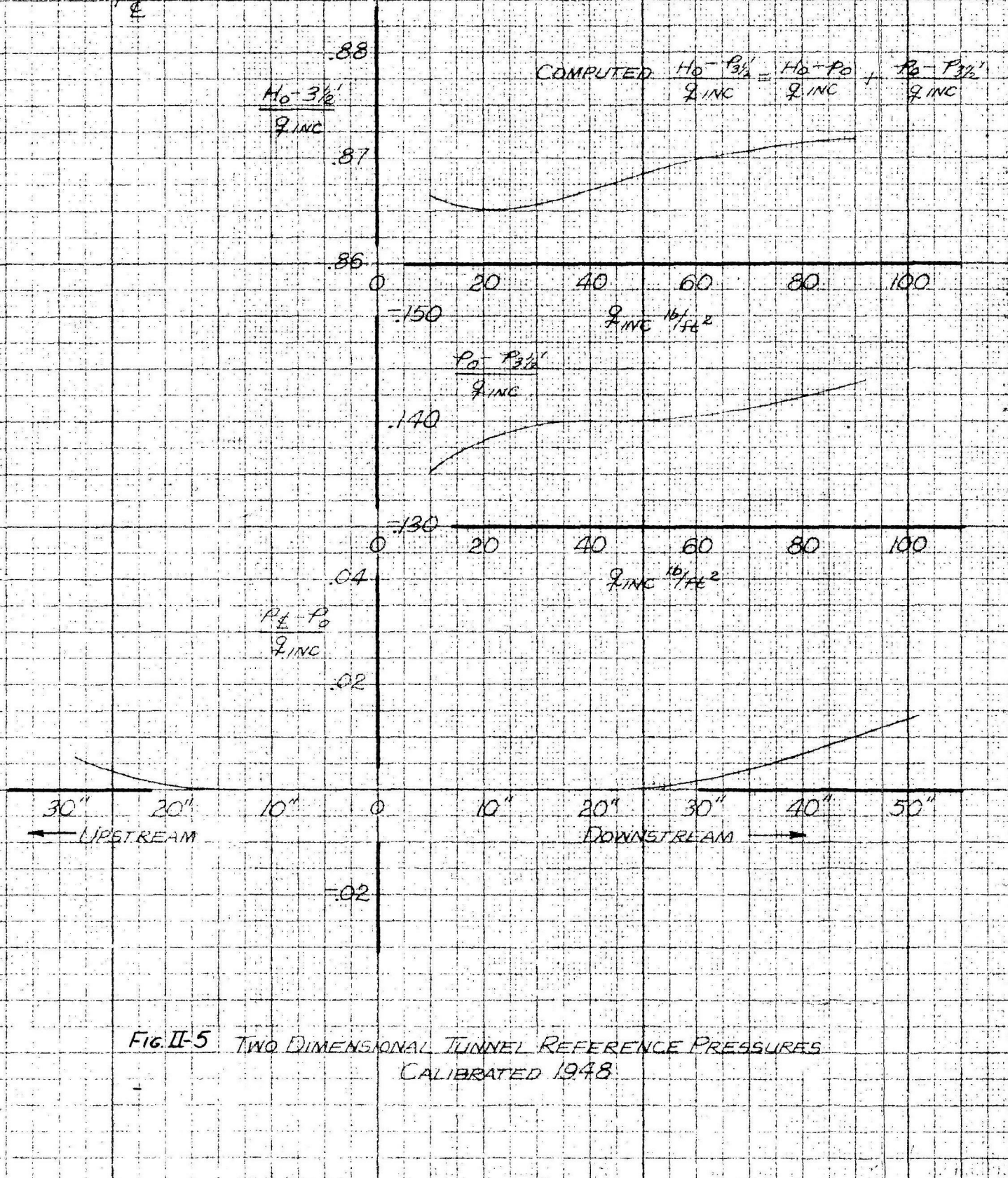

FIG. II-5 TWO DIMENSIONAL TUNNEL REFERENCE PRESSURES
CALIBRATED 1948

GALCIT REP 534

⊙ CLEAR TUNNEL, q_o = 40 LB/FT.^{2} RUN 6

STATIC PRESSURE TRAVERSE USING GALCIT STANDARD PRANDTL PITOT TUBE MOUNTED ON TRAVERSE FRAME

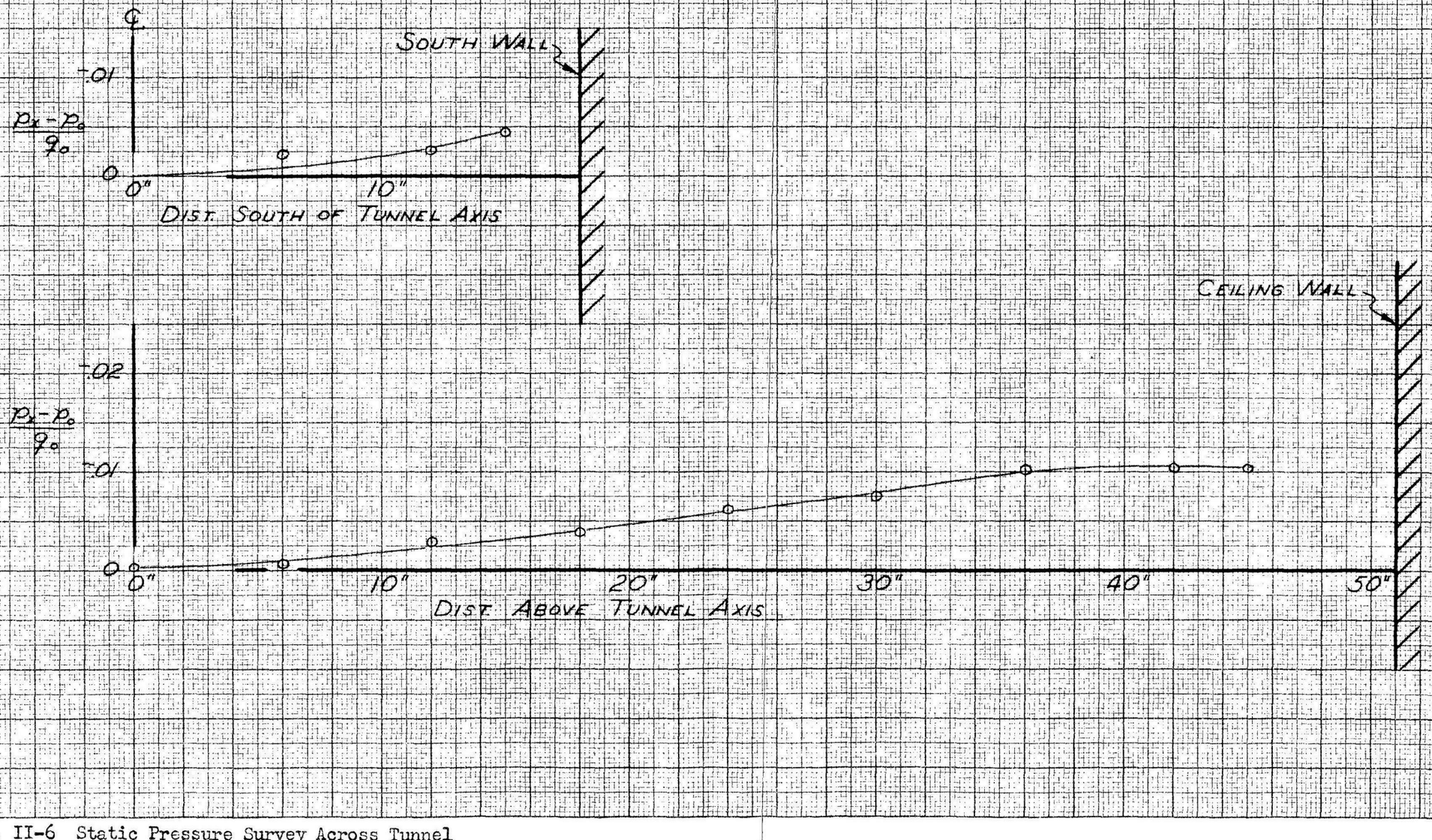

Fig. II-6 Static Pressure Survey Across Tunnel

GALCIT REP. 534

PAGE
FIG

AVERAGE OF FLOOR & CEILING AXIAL STATIC PRESSURES (CLEAR TUNNEL)

- ○ q_{t_0} = 10 LB/FT², RUNS 1, 27
- △ q_{t_0} = 20 LB/FT², " 2, 27
- □ q_{t_0} = 80 LB/FT², " 4, 27

p_{w_0} = STATIC PRESSURE AT FLOOR & CEILING, CLEAR TUNNEL
p_0 = " " " INTERSECTION OF TRUNNION AND TUNNEL AXES, CLEAR TUNNEL
q_{t_0} = DYNAMIC PRESSURE AT INTERSECTION OF TRUNNION AND TUNNEL AXES, CLEAR TUNNEL

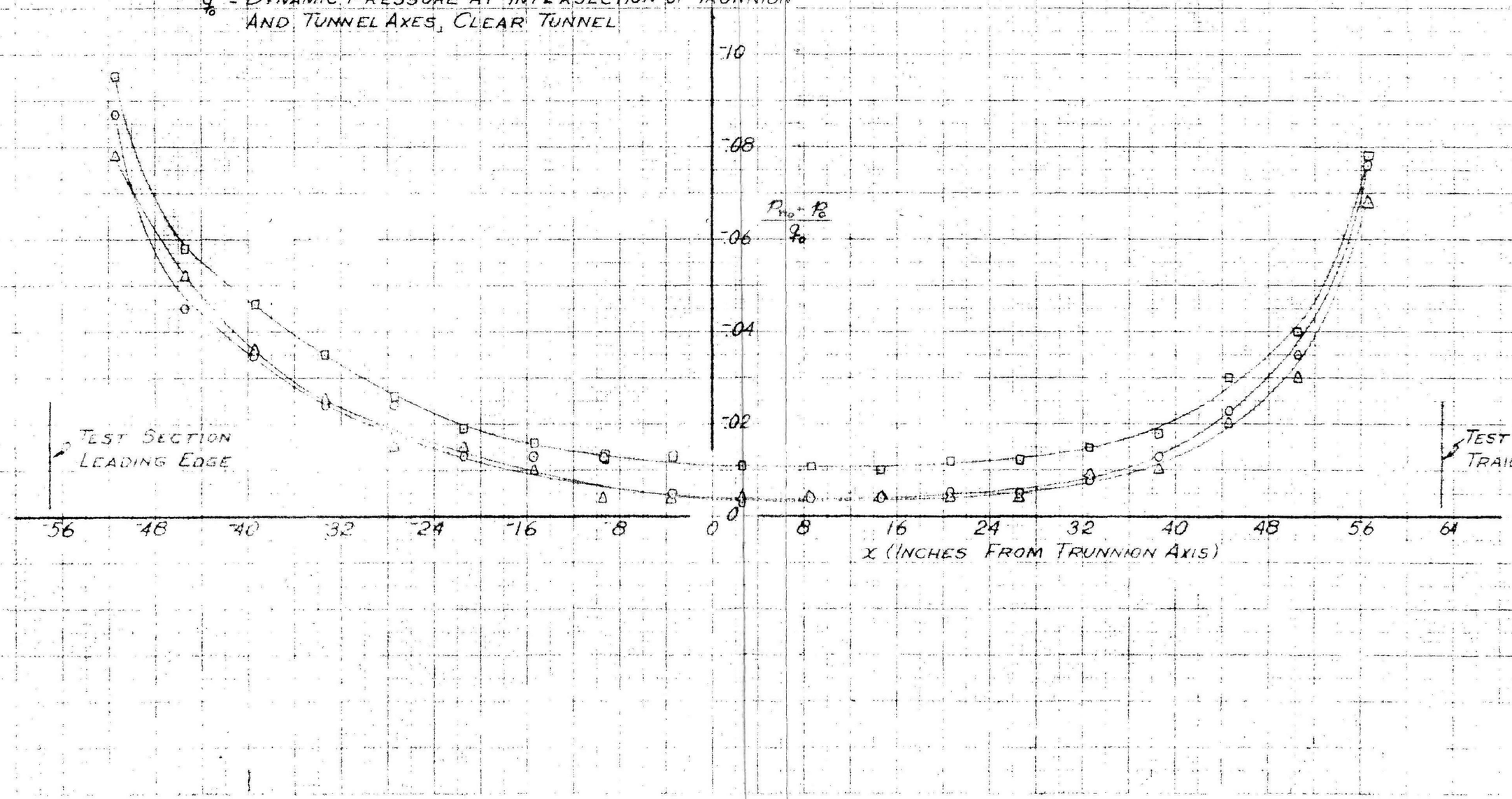

Fig. II-7 Static Pressure Survey Along Floor and Ceiling

GALCIT REP. 534

WAKE RAKE STATIC PRESSURE ORIFICE CALIBRATION (RUN 39)

$\Delta p = p_x - p_{TRUE}$

p_x = RAKE STATIC PRESSURE READING

p_{TRUE} = TRUE " " ON TUNNEL AXIS

q_o = DYNAMIC PRESSURE (CLEAR TUNNEL)

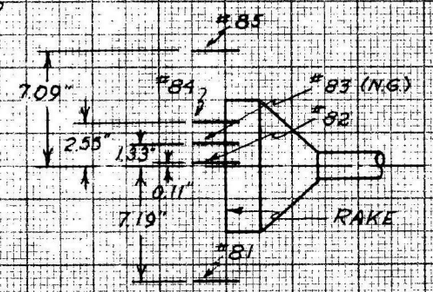

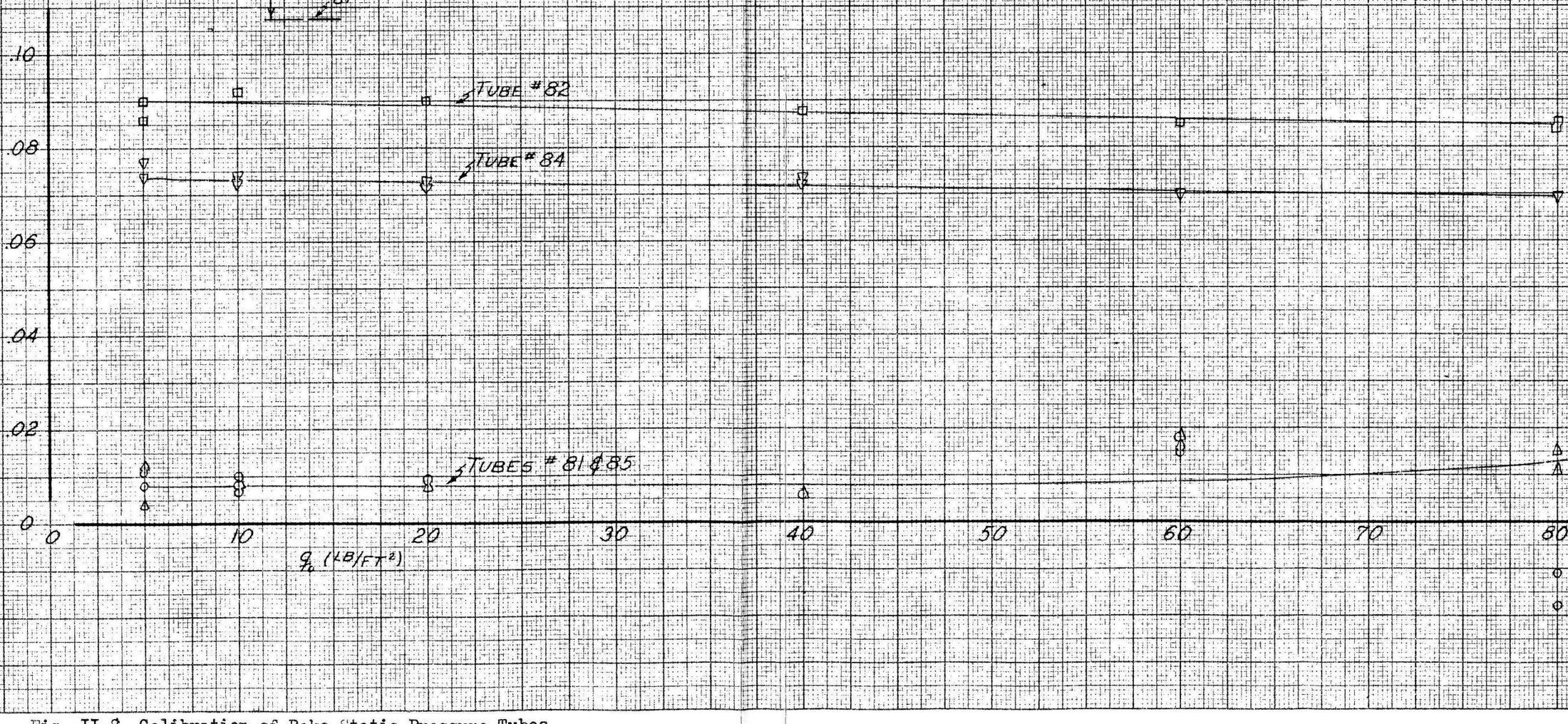

Fig. II-8 Calibration of Rake Static Pressure Tubes

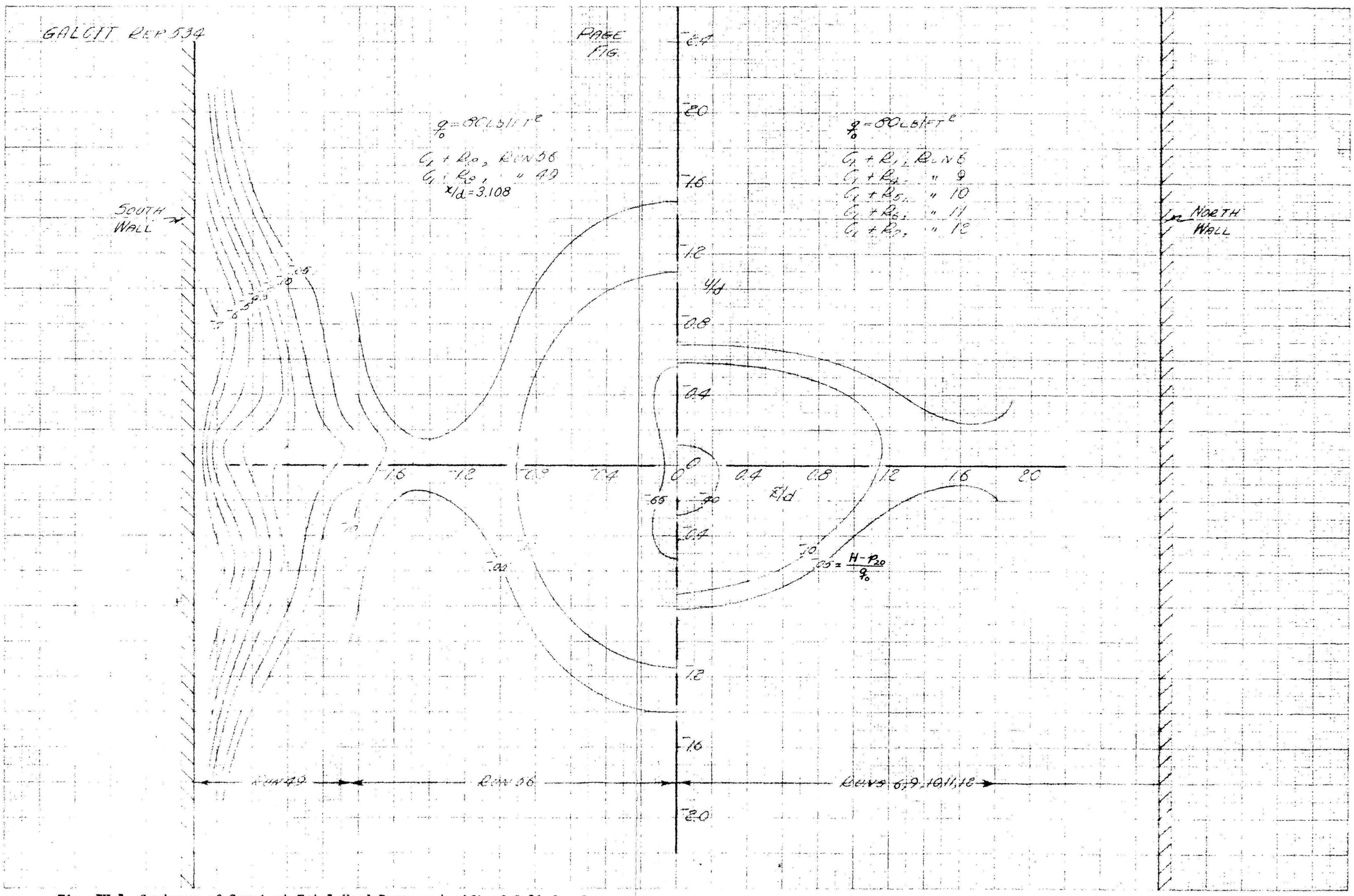

Fig. IV-1 Contours of Constant Total Head Decrements Aft of Cylinder C_1 without Separation Strips, x/d = 3.108

Fig. IV-2 Contours of Constant Total Head Decrements Aft of Cylinder C_1 without Separation Strips, x/d = 5.837

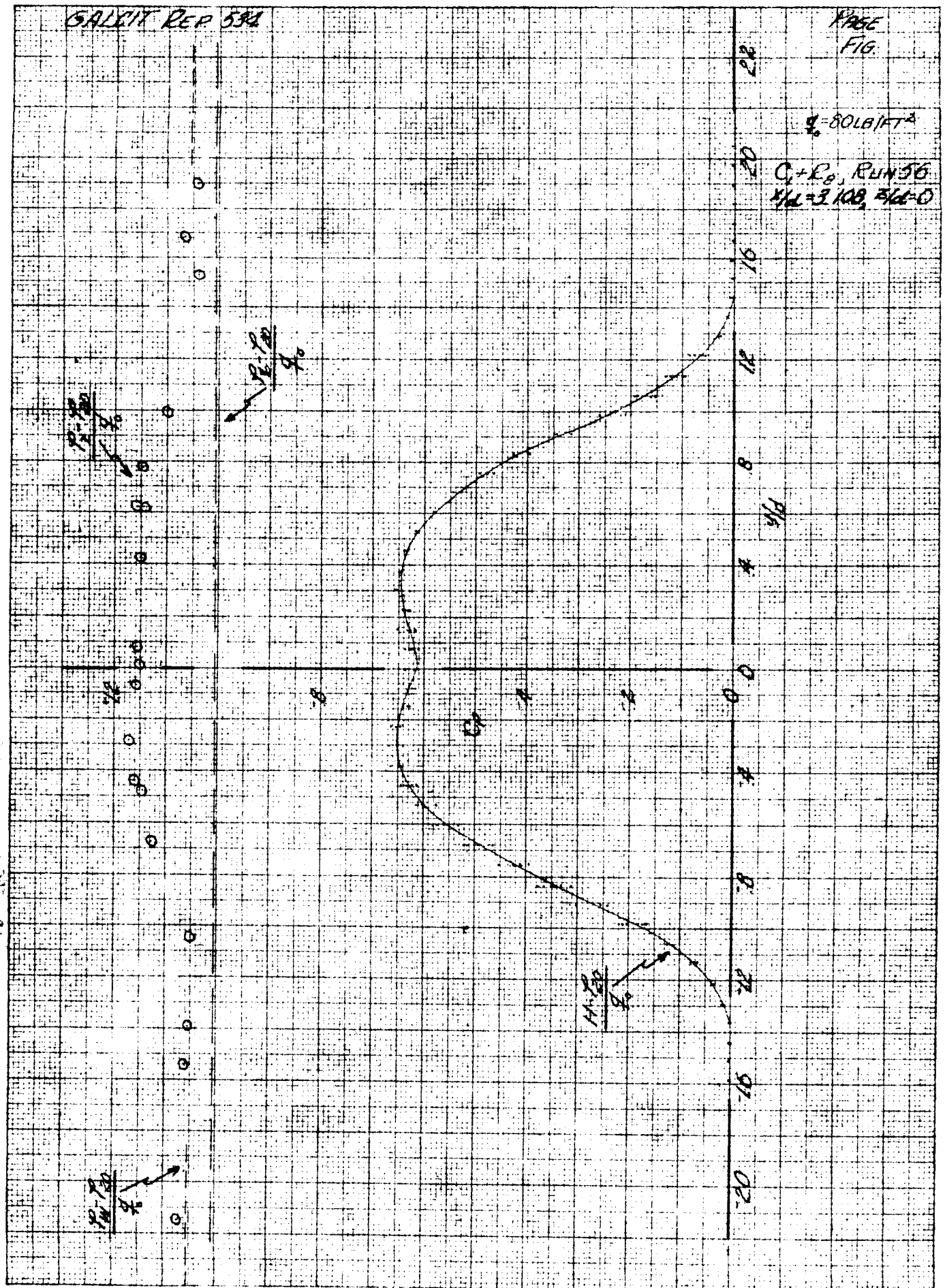

Fig. IV-3 Wake Pattern Aft of Cylinder C_1, x/d = 3.108, z/d = 0

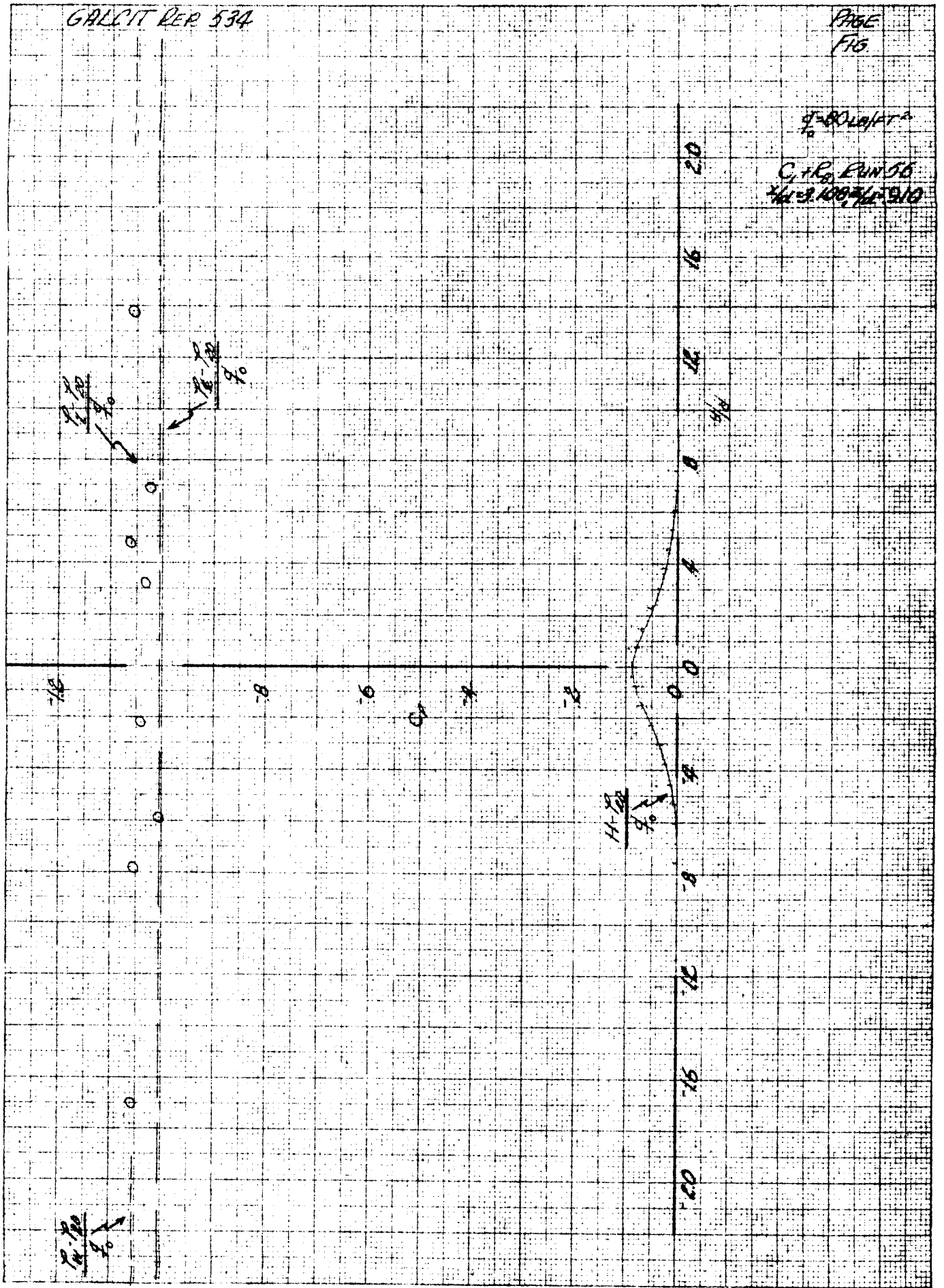

Fig. IV-4 Wake Pattern Aft of Cylinder C_1, x/d = 3.108, z/d = -0.910

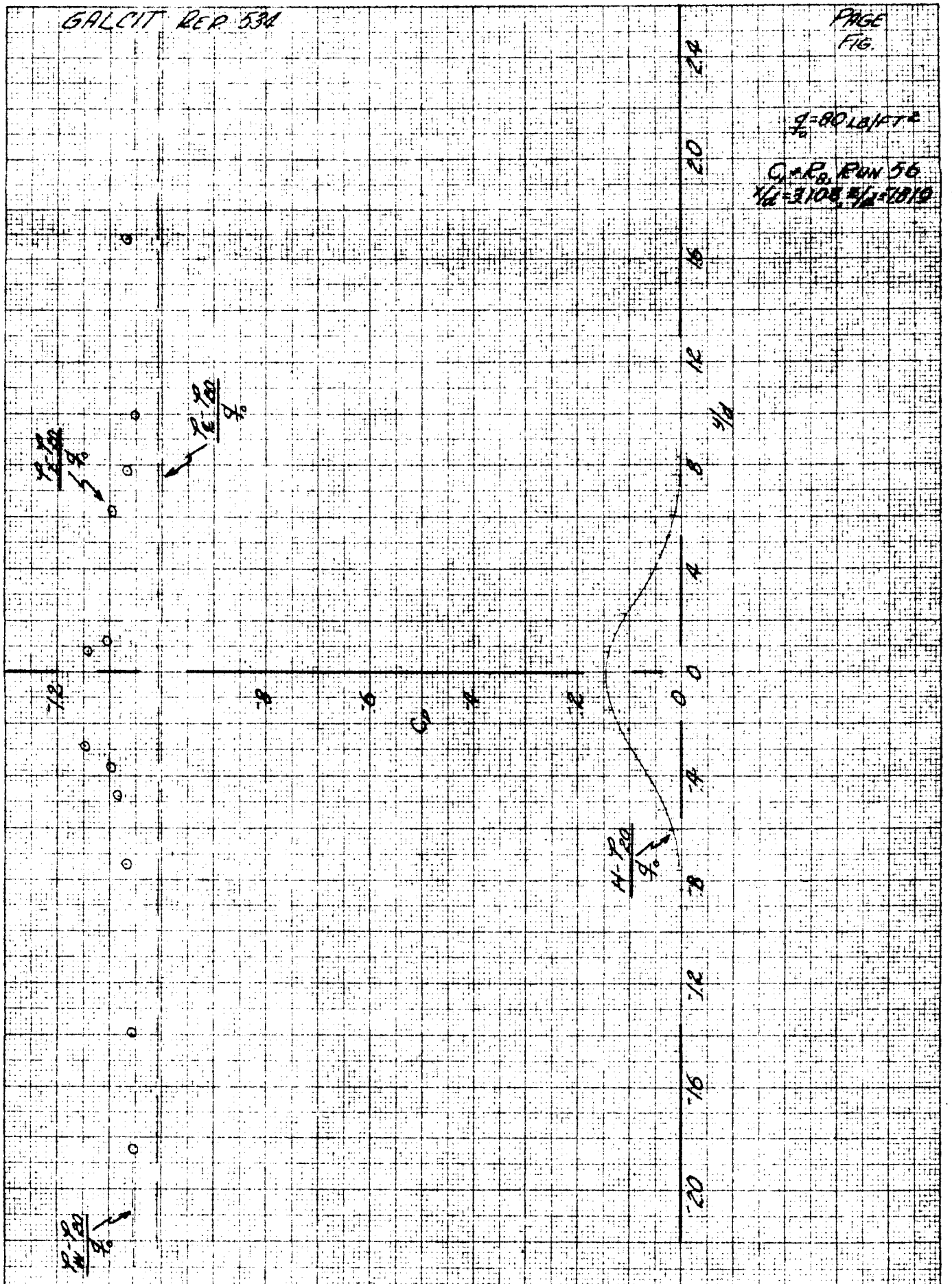

Fig. IV-5 Wake Pattern Aft of Cylinder C_1, x/d = 3.108, z/d = -1.819

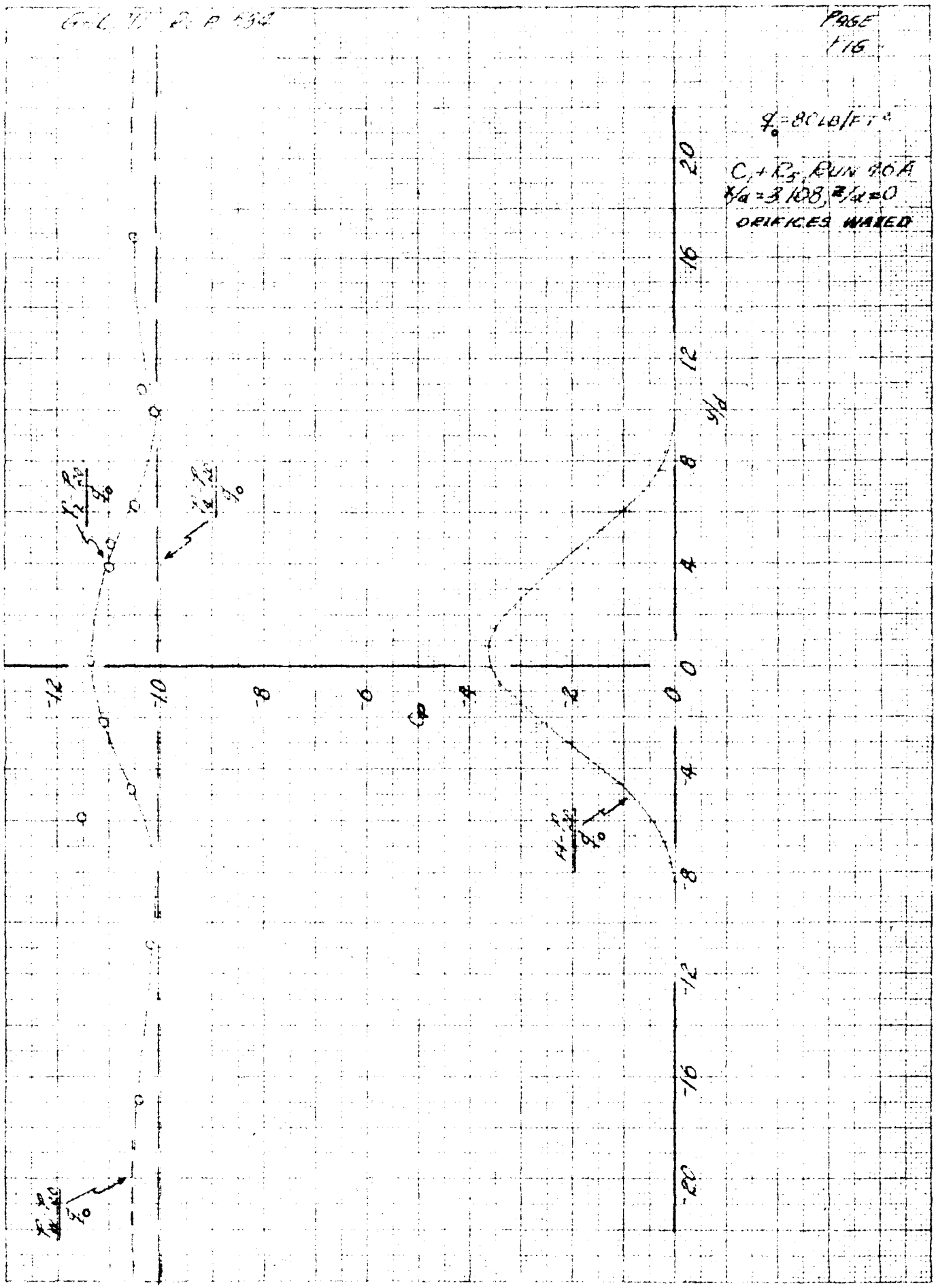

Fig. IV-6 Wake Pattern Aft of Cylinder C_1, Orifices Waxed, x/d = 3.108, z/d = 0

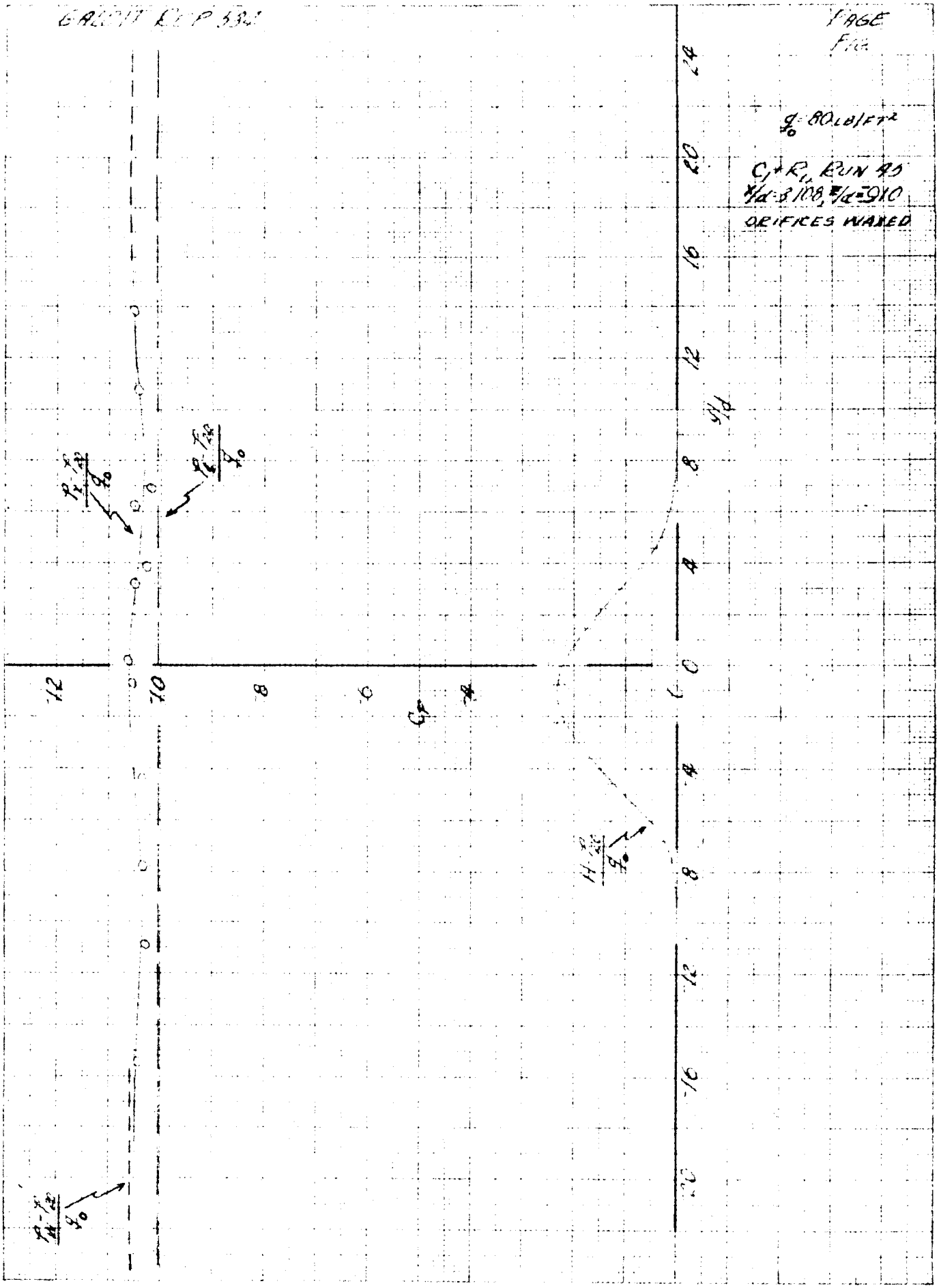

Fig. IV-7 Wake Pattern Aft of Cylinder C_1, Orifices Waxed, $x/d = 3.108$, $z/d = -0.910$

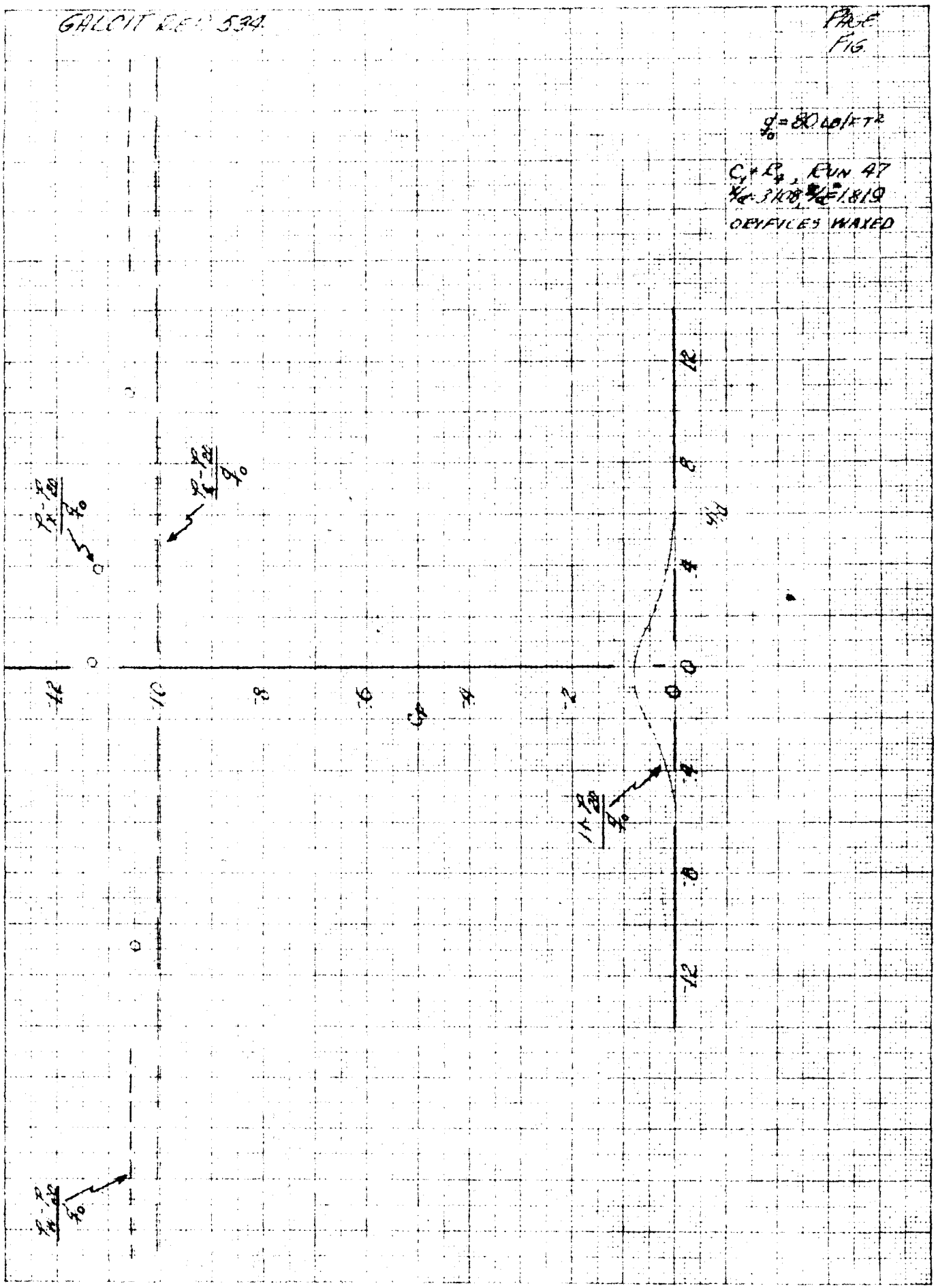

Fig. IV-8 Wake Pattern Aft of Cylinder C_1, Orifices Waxed, $x/d = 3.108$, $z/d = -1.819$

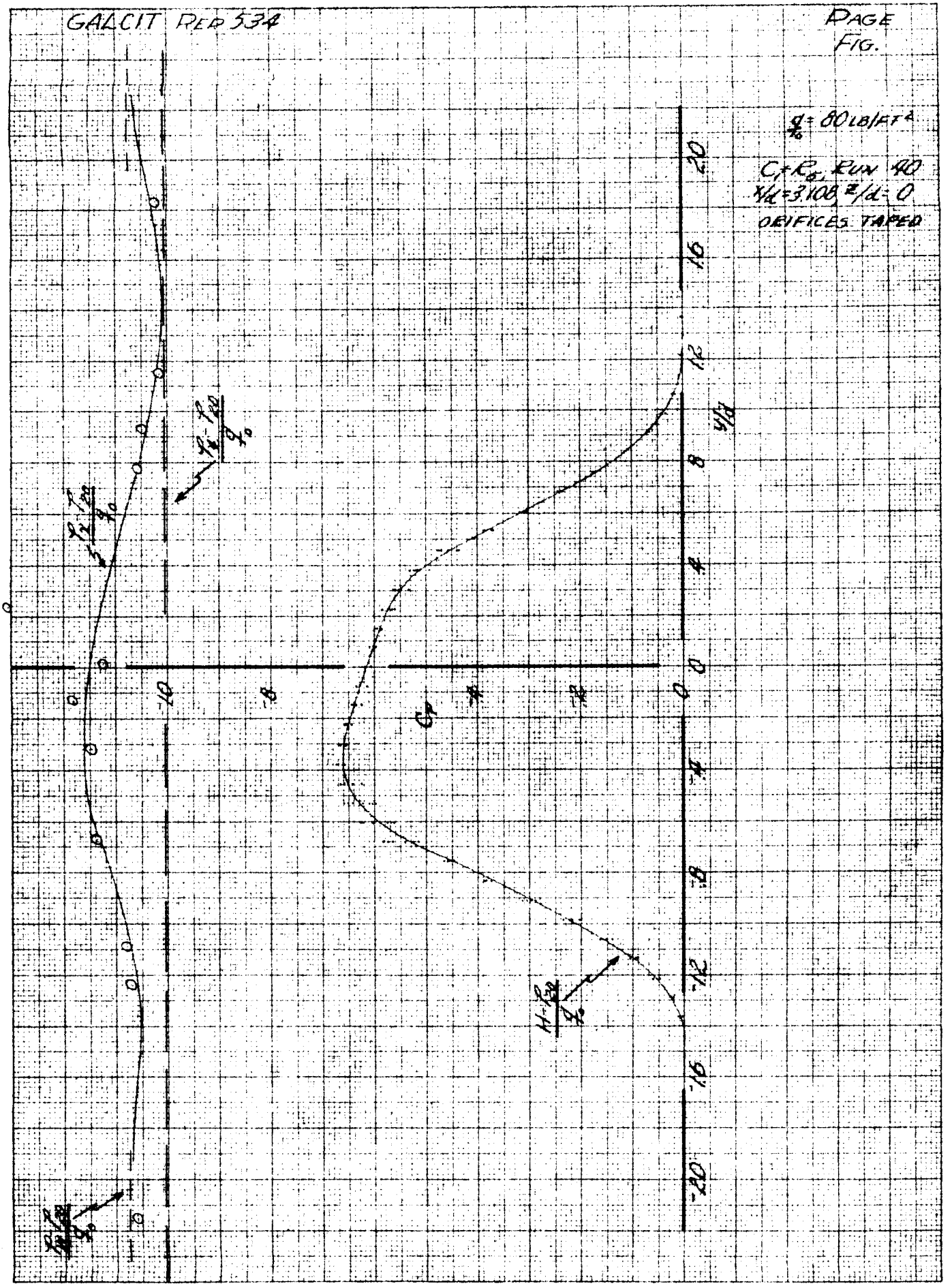

Fig. IV-9 Wake Pattern Aft of Cylinder C_1, Orifices Taped, x/d = 3.108, z/d = 0

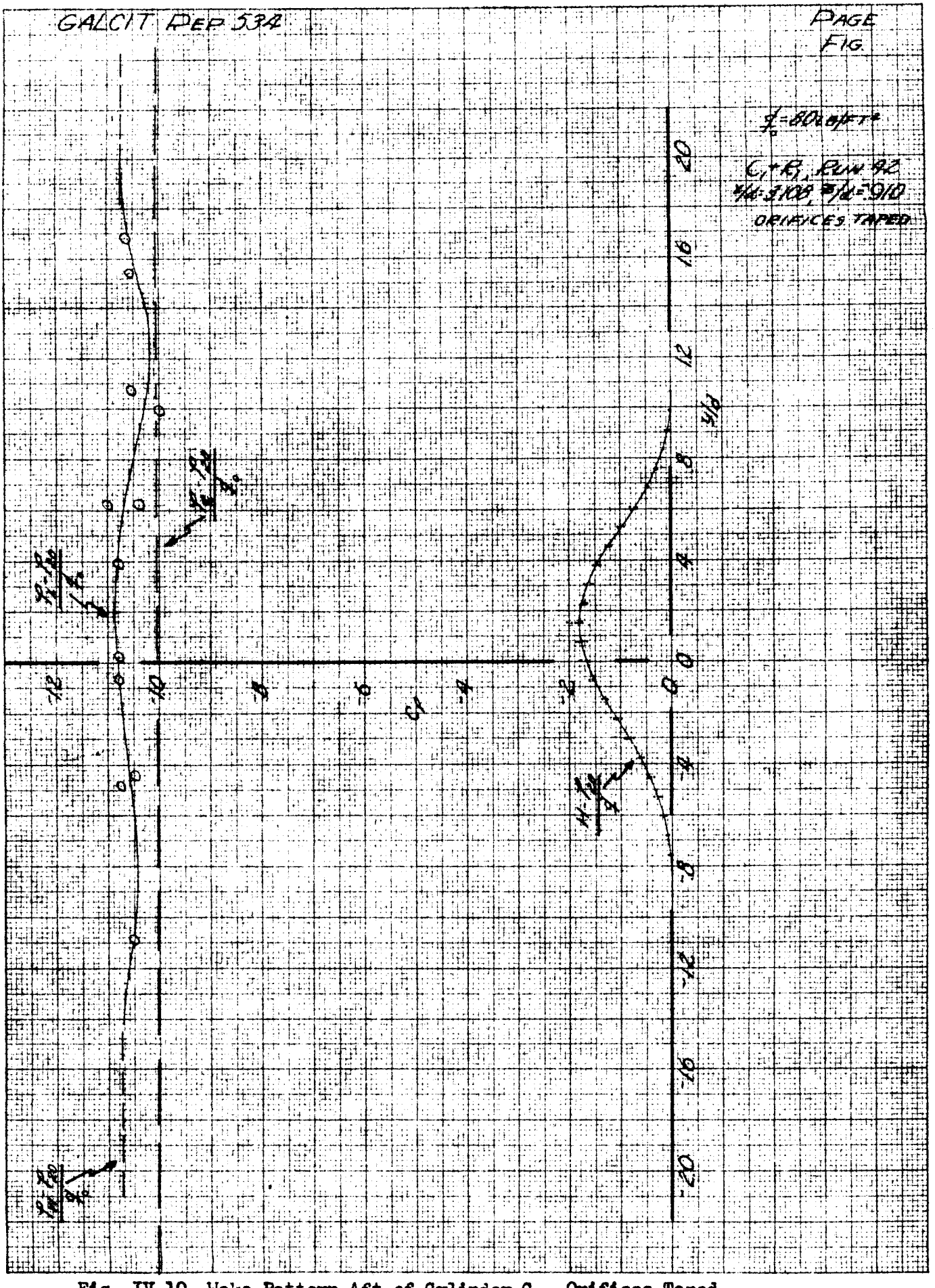

Fig. IV-10 Wake Pattern Aft of Cylinder C_1, Orifices Taped, x/d = 3.108, z/d = -0.910

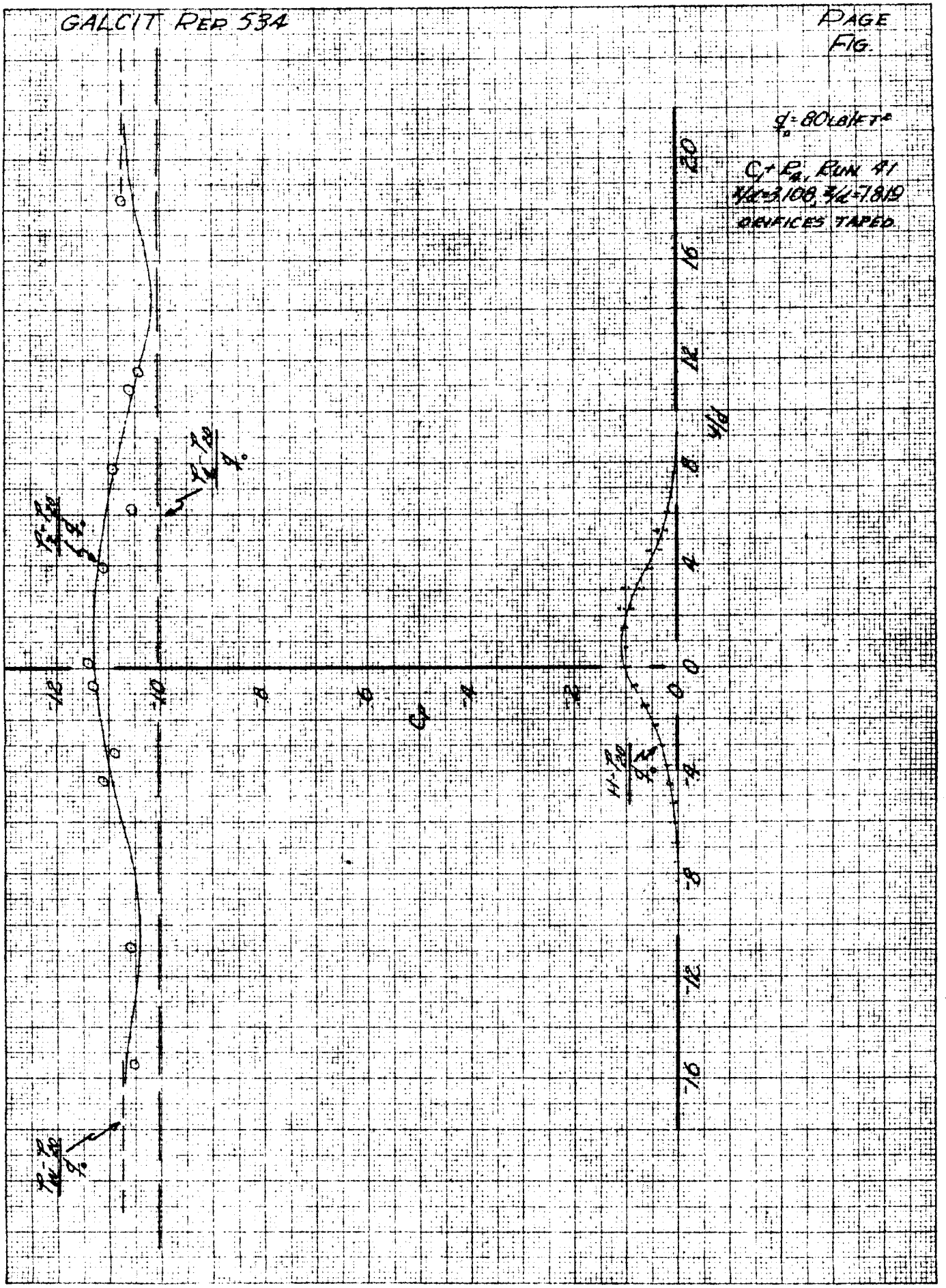

Fig. IV-11 Wake Pattern Aft of Cylinder C_l, Orifices Taped, x/d = 3.108, z/d = -1.819

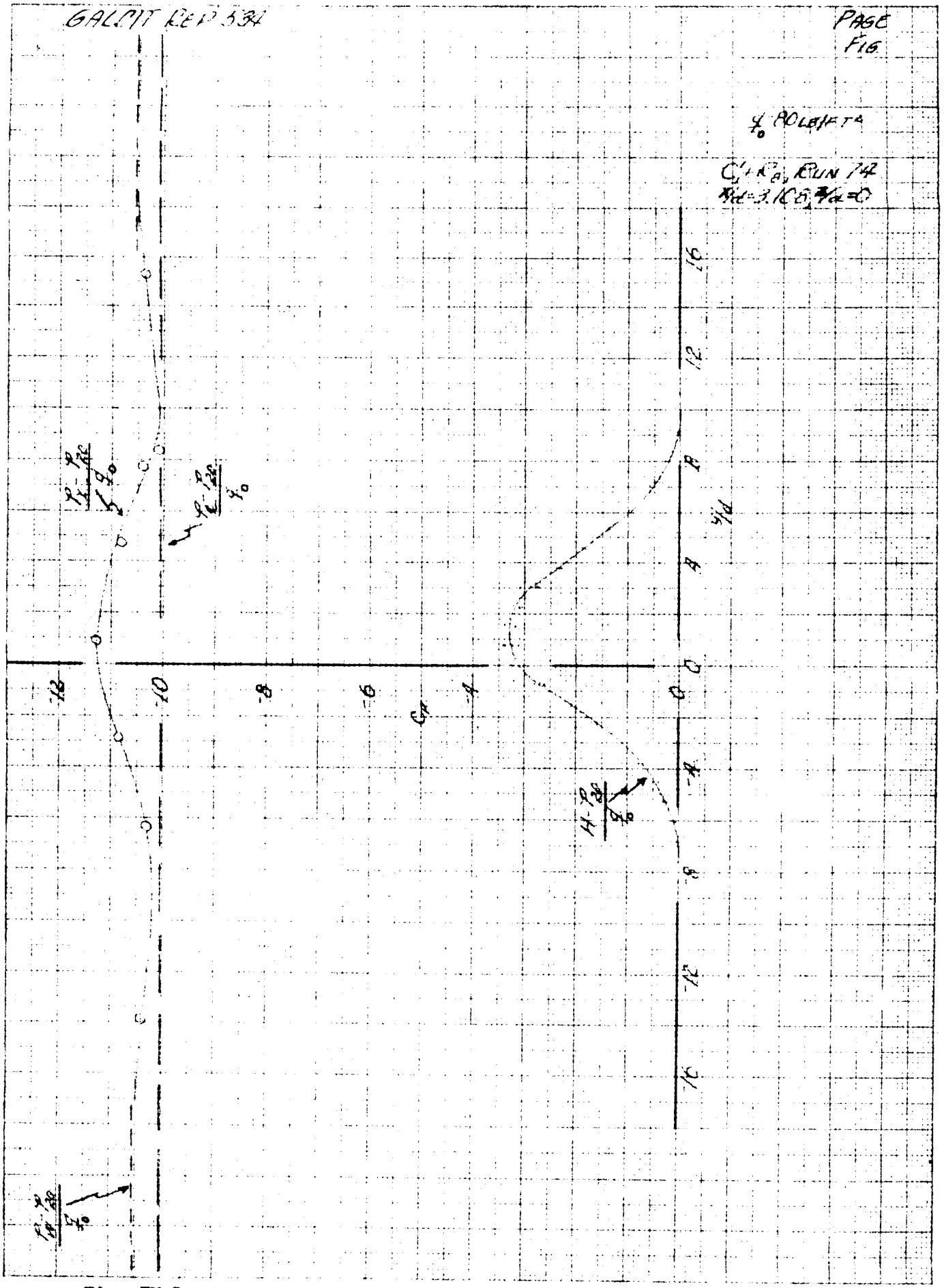

Fig. IV-12 Wake Pattern Aft of Cylinder C_1, Orifices Plugged, x/d = 3.108, z/d = 0

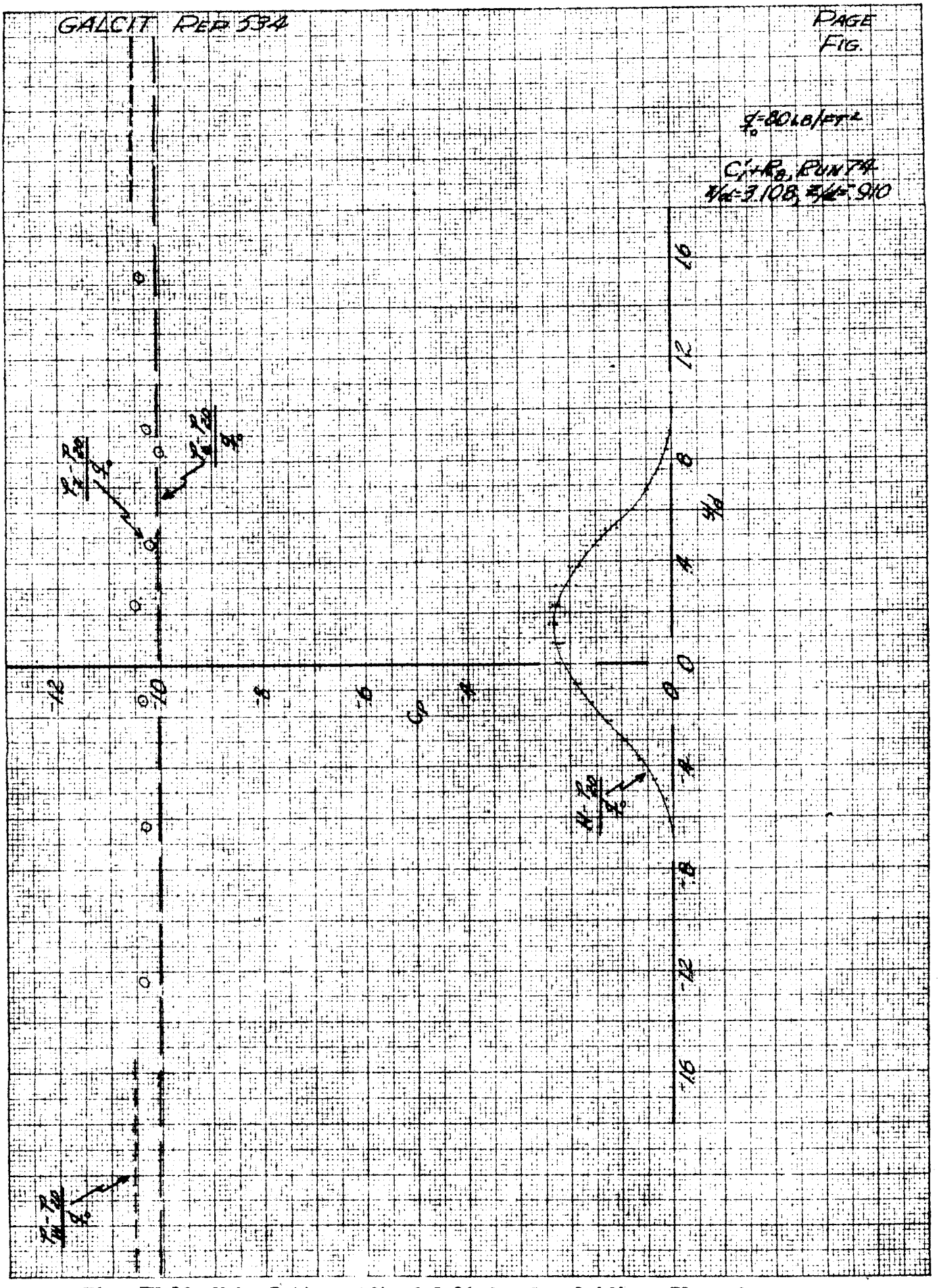

Fig. IV-13 Wake Pattern Aft of Cylinder C_1, Orifices Plugged, x/d = 3.108, z/d = -0.910

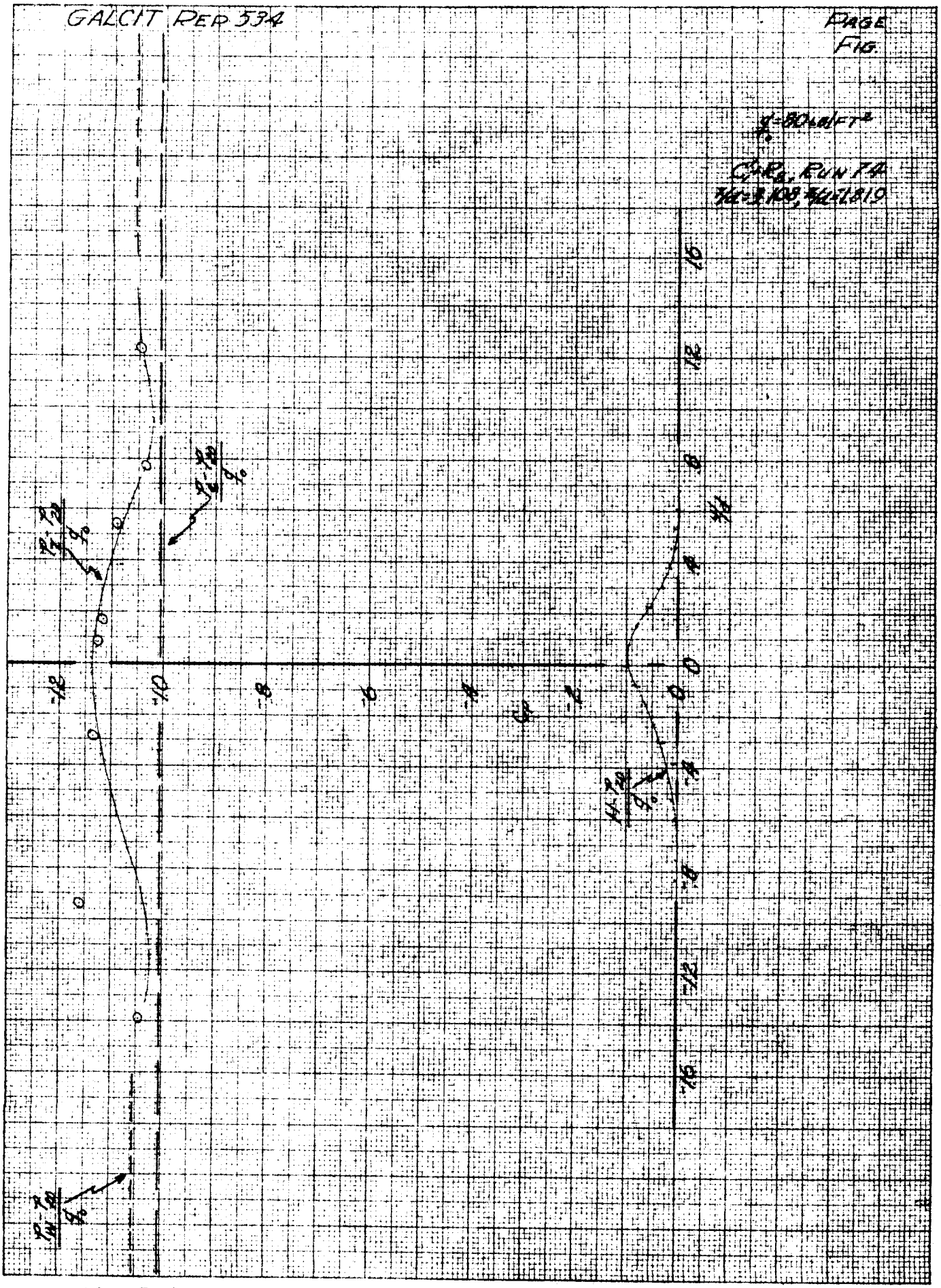

Fig. IV-14 Wake Pattern Aft of Cylinder C_1, Orifices Plugged, x/d = 3.108, z/d = -1.819

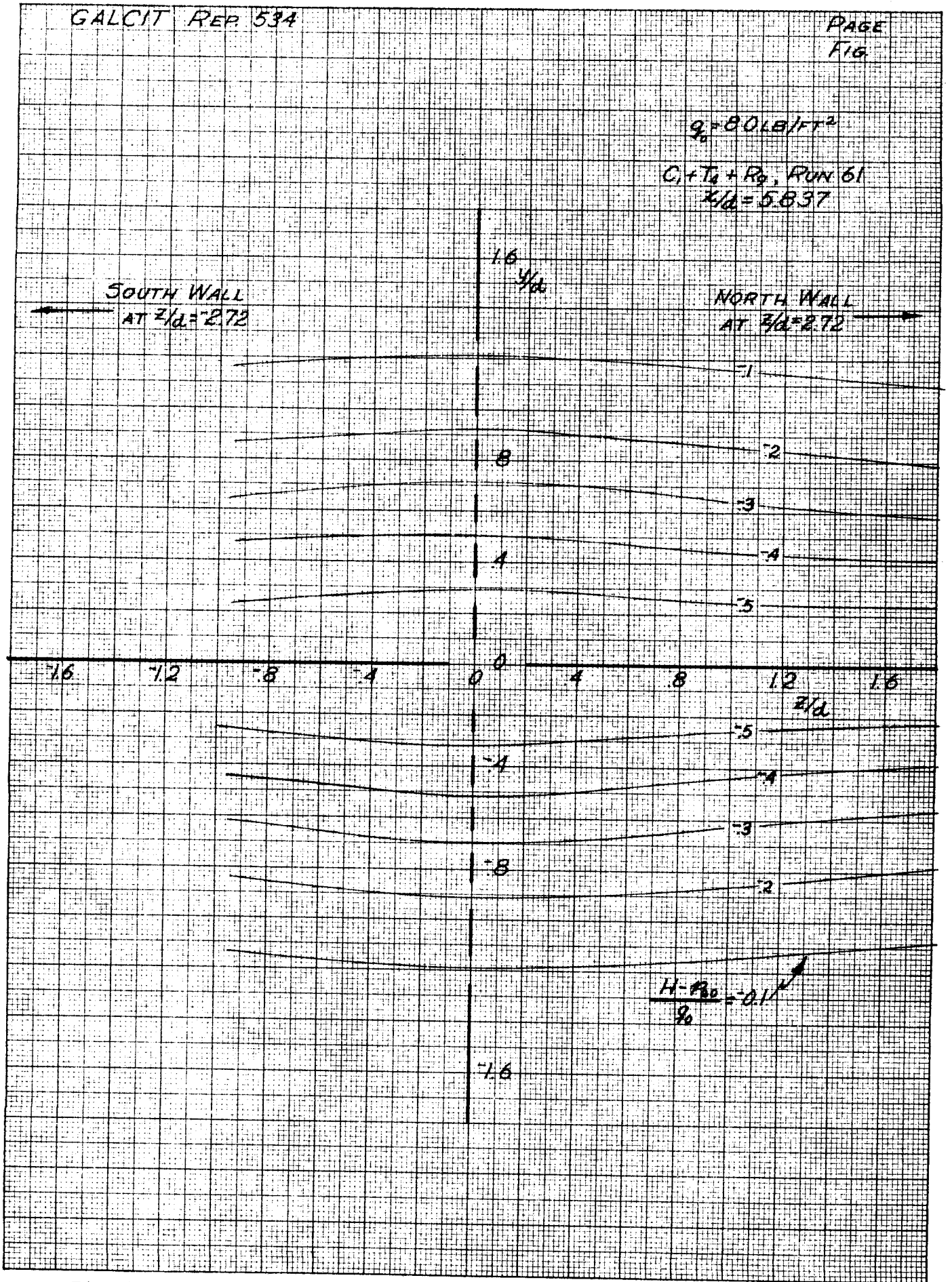

Fig. IV-15 Contours of Constant Total Head Decrements Aft of Cylinder C_1 with Separation Strips T_4, x/d = 5.837

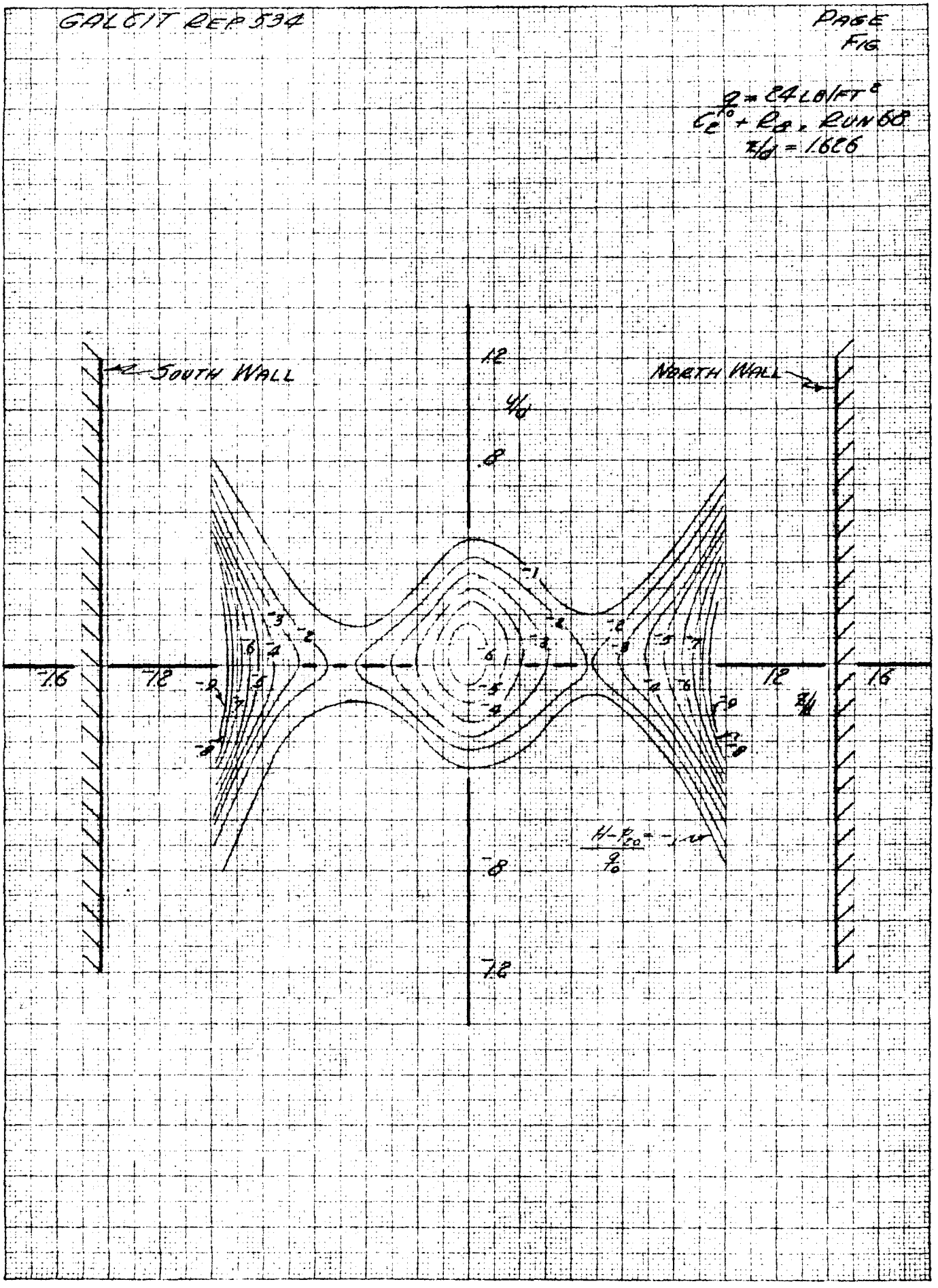

Fig. IV-16 Contours of Constant Total Head Decrements Aft of Cylinder C_2 without Separation Strips. x/d = 1.626

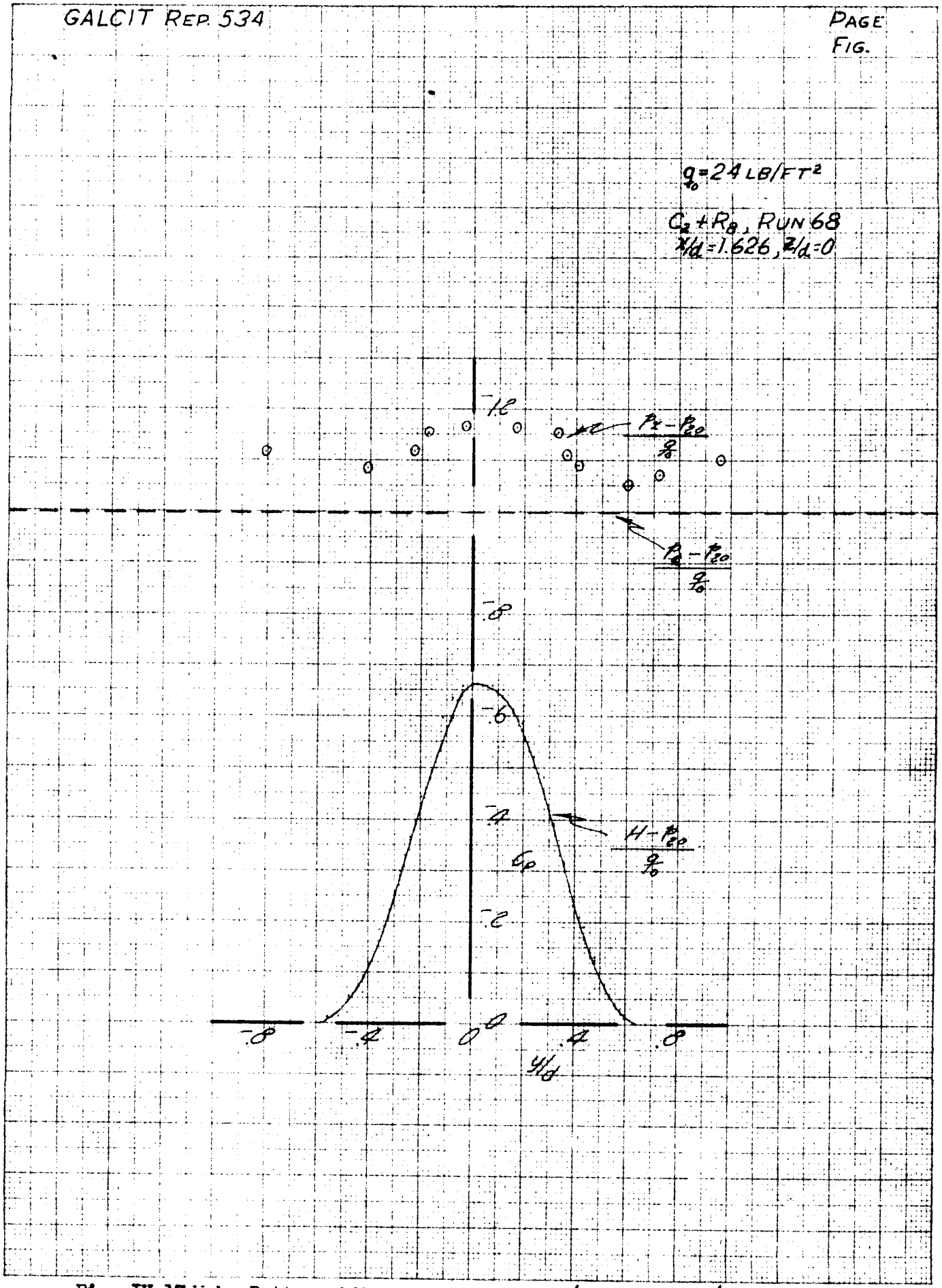

Fig. IV-17 Wake Pattern Aft of Cylinder C_2, x/d = 1.626, z/d = 0

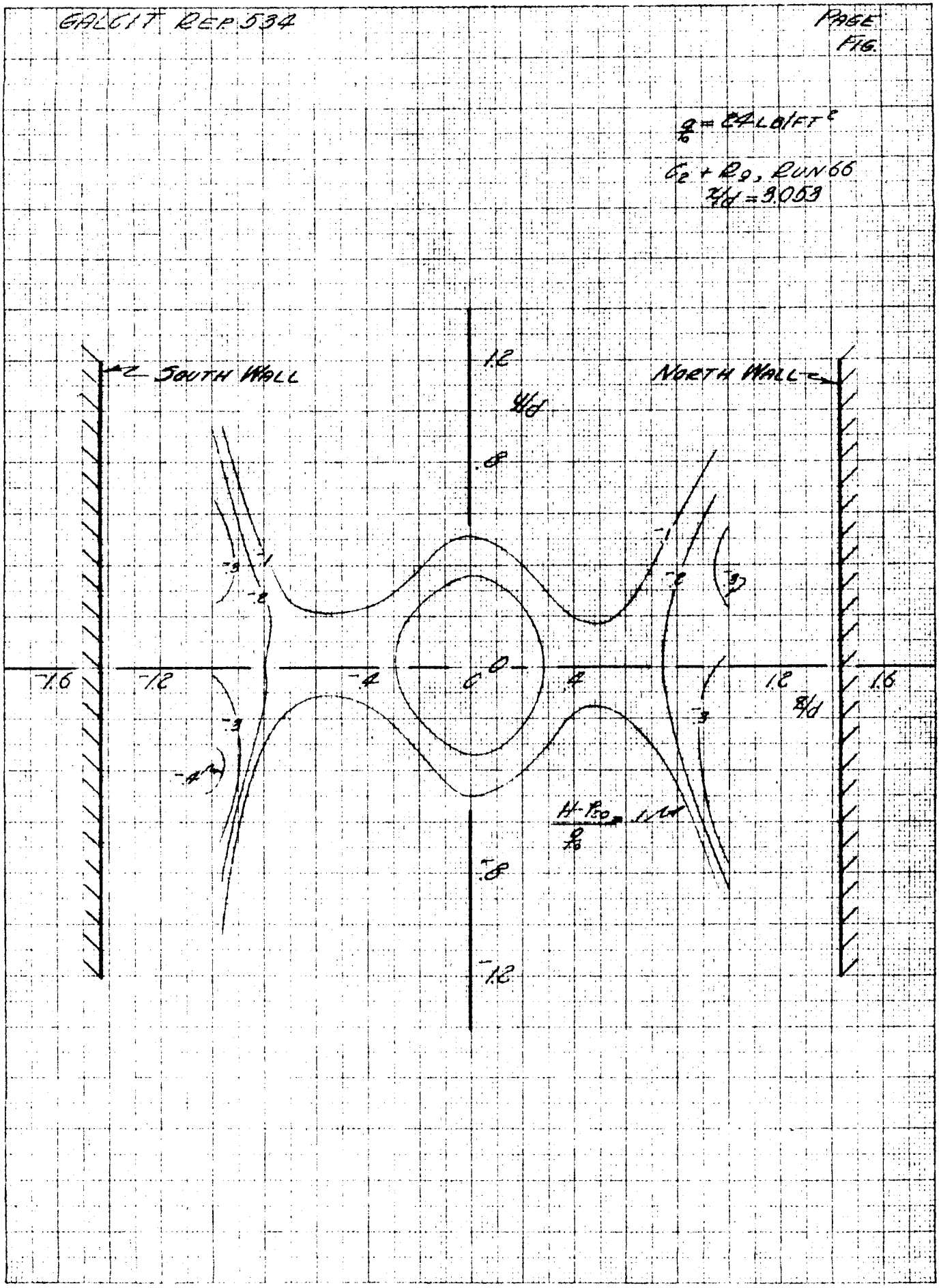

Fig. IV-18 Contours of Constant Total Head Decrements Aft of Cylinder C_2 without Separation Strips, x/d = 3.053

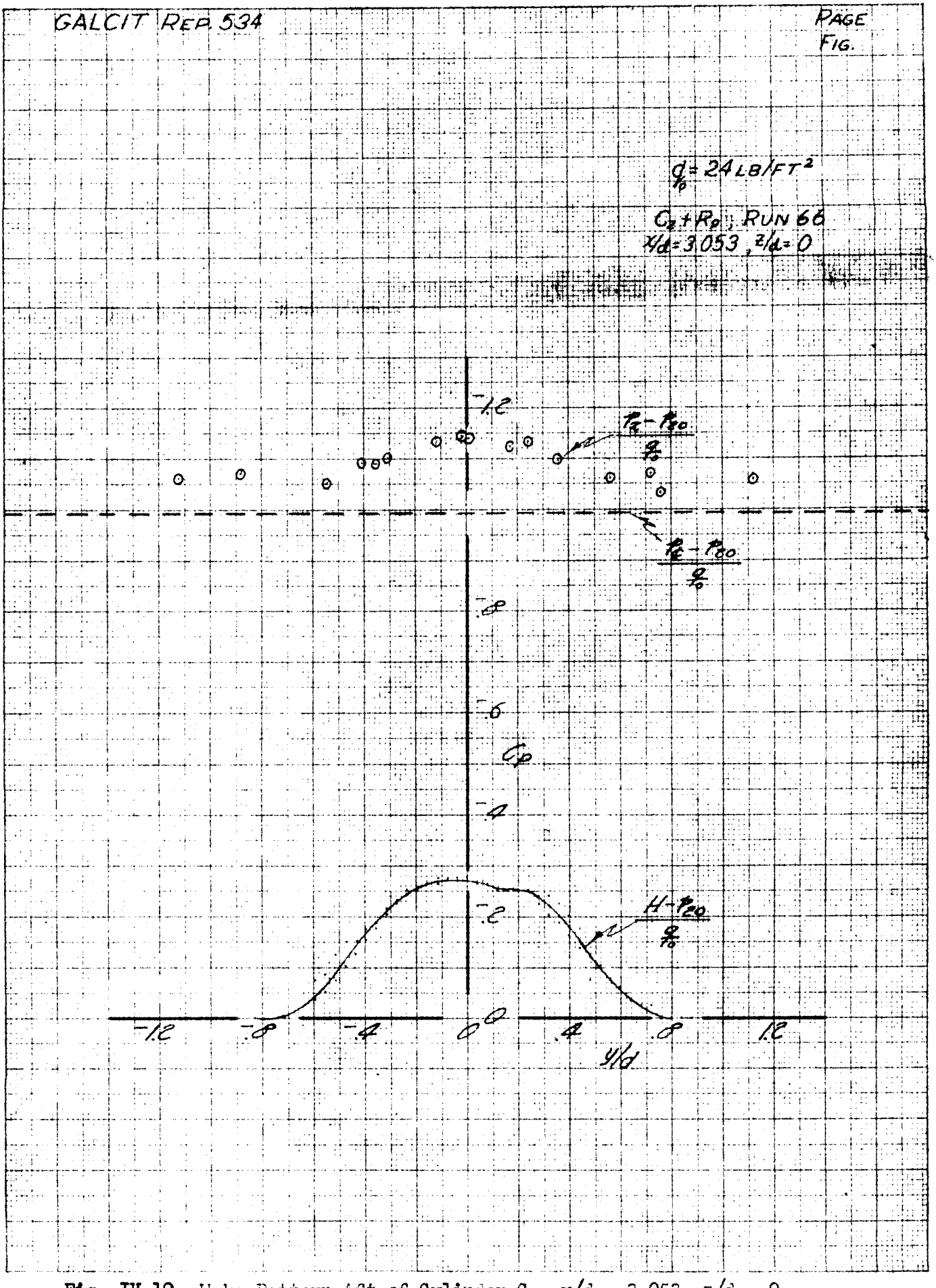

Fig. IV-19 Wake Pattern Aft of Cylinder C_2, x/d = 3.053, z/d = 0

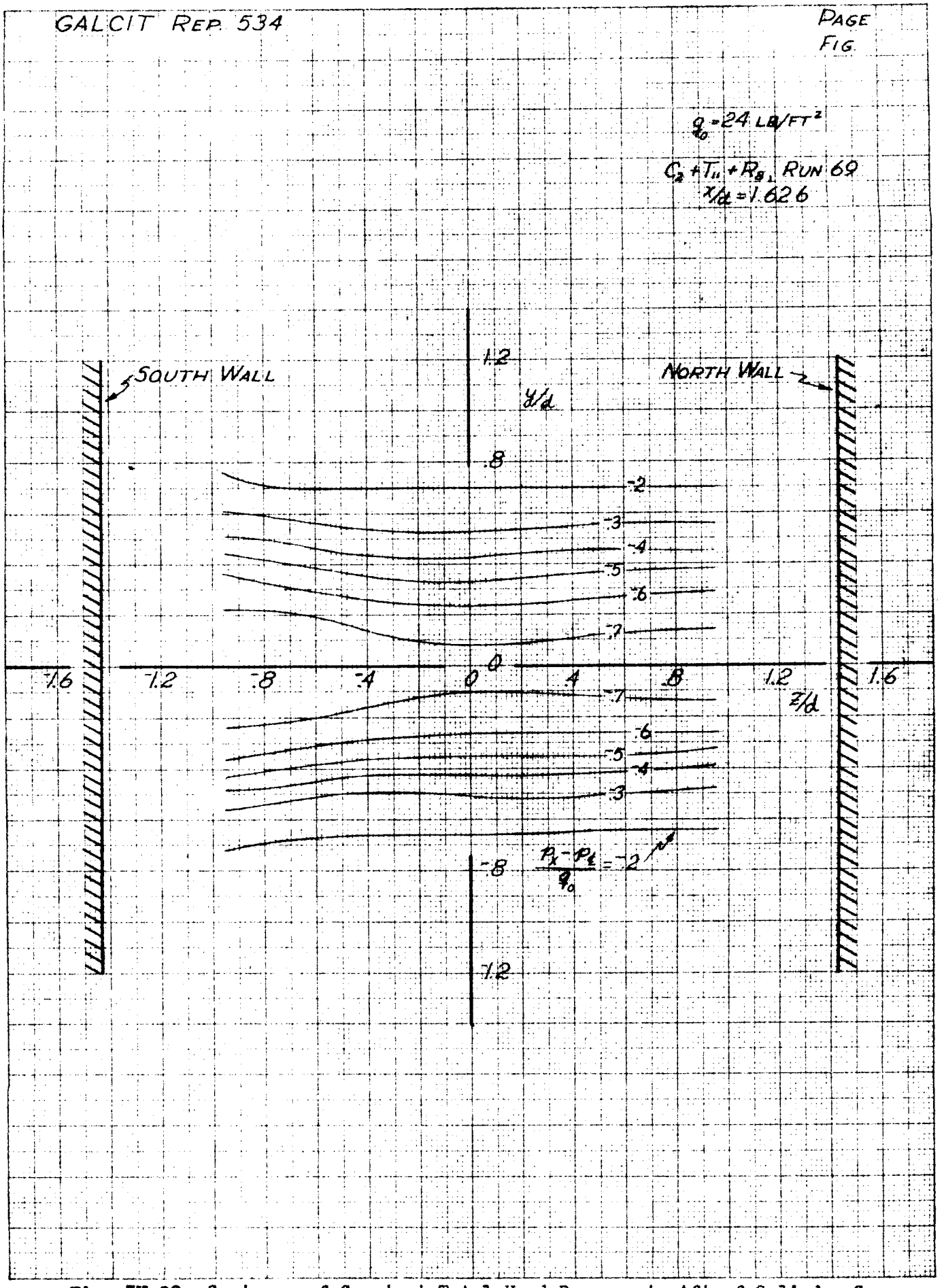

Fig. IV-20 Contours of Constant Total Head Decrements Aft of Cylinder C_2 with Separation Strips T_{11}, x/d = 1.626

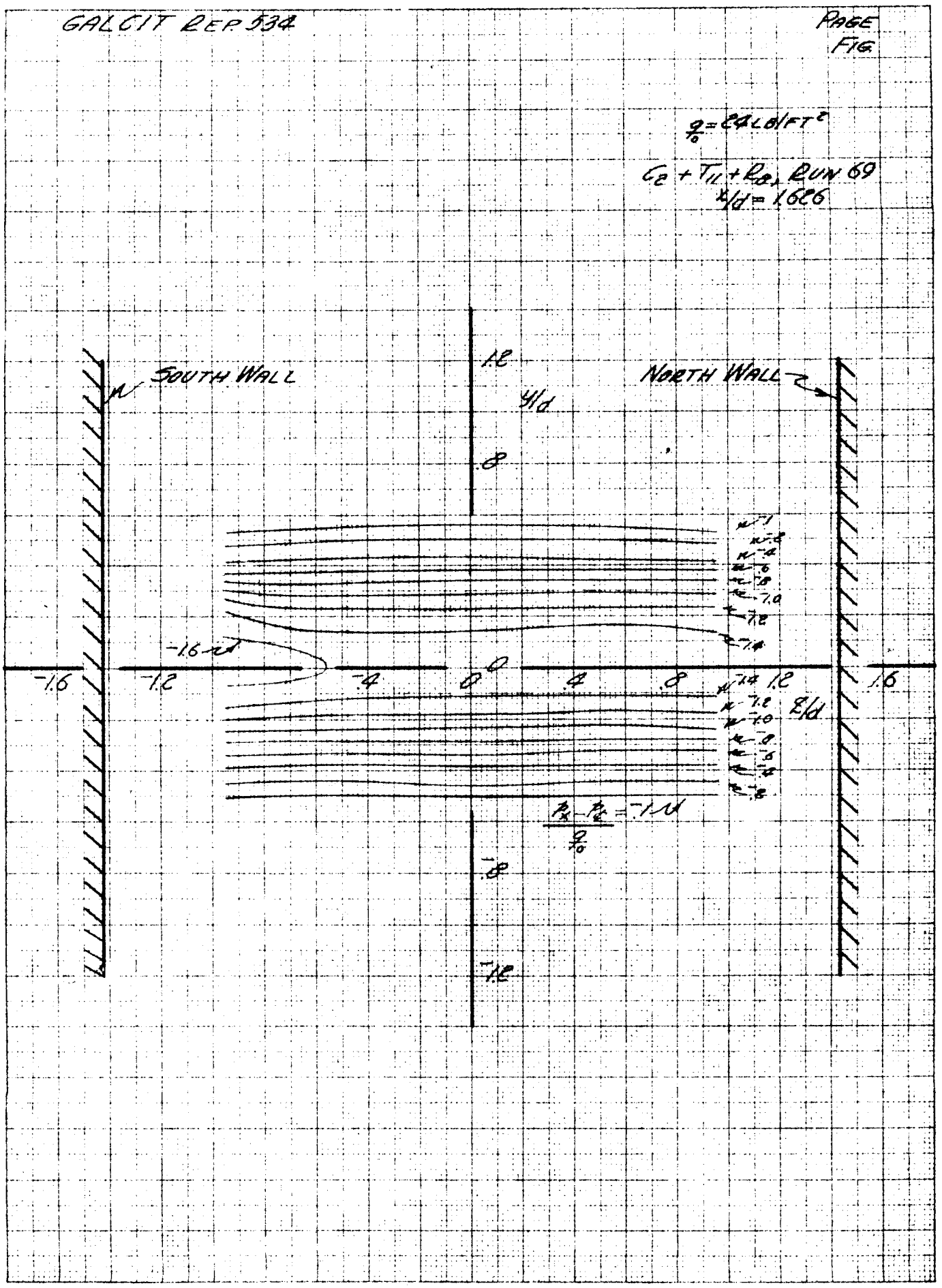

Fig. IV-21 Contours of Constant Static Pressure Decrements Aft of Cylinder C_2 with Separation Strips T_{11}, x/d = 1.626

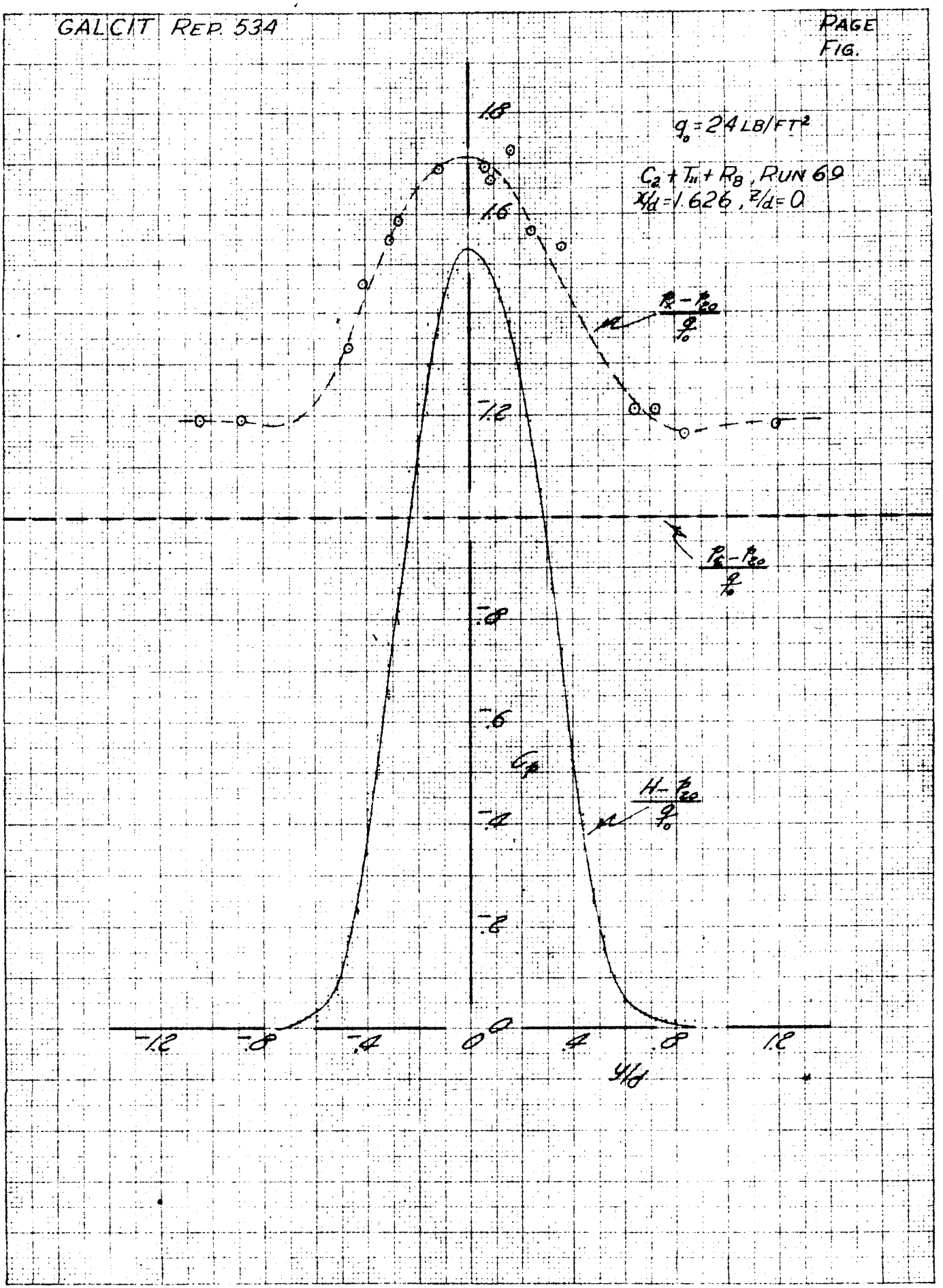

Fig. IV-22 Wake Pattern Aft of Cylinder C_2 with Separation Strips T_{11}, x/d = 1.626, z/d = 0

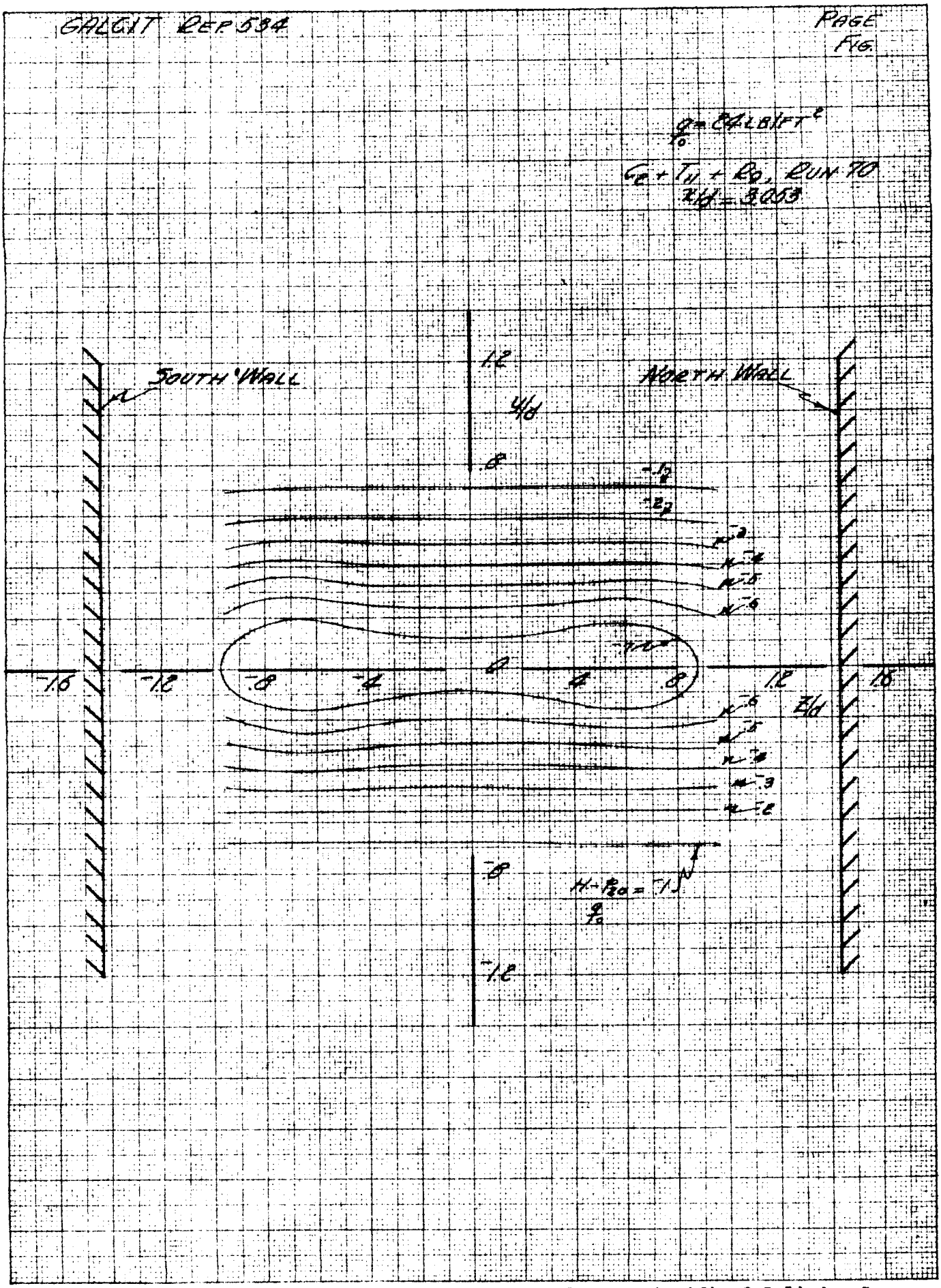

Fig. IV-23 Contours of Constant Total Head Decrements Aft of Cylinder C_2 with Separation Strips T_{11}, x/d = 3.053

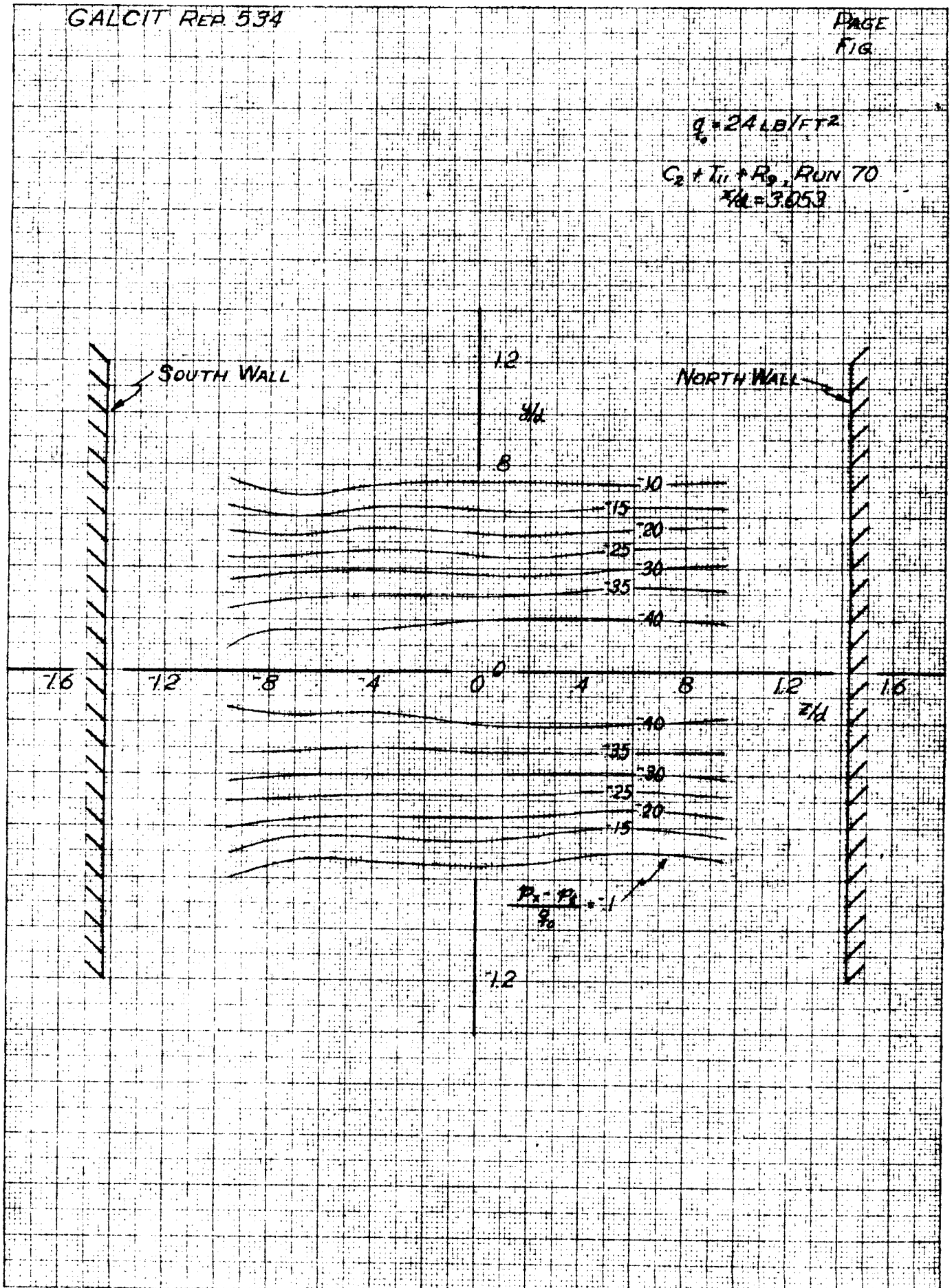

Fig. IV-24 Contours of Constant Static Pressure Decrements Aft of Cylinder C_2 with Separation Strips T_{11}, x/d = 3.053

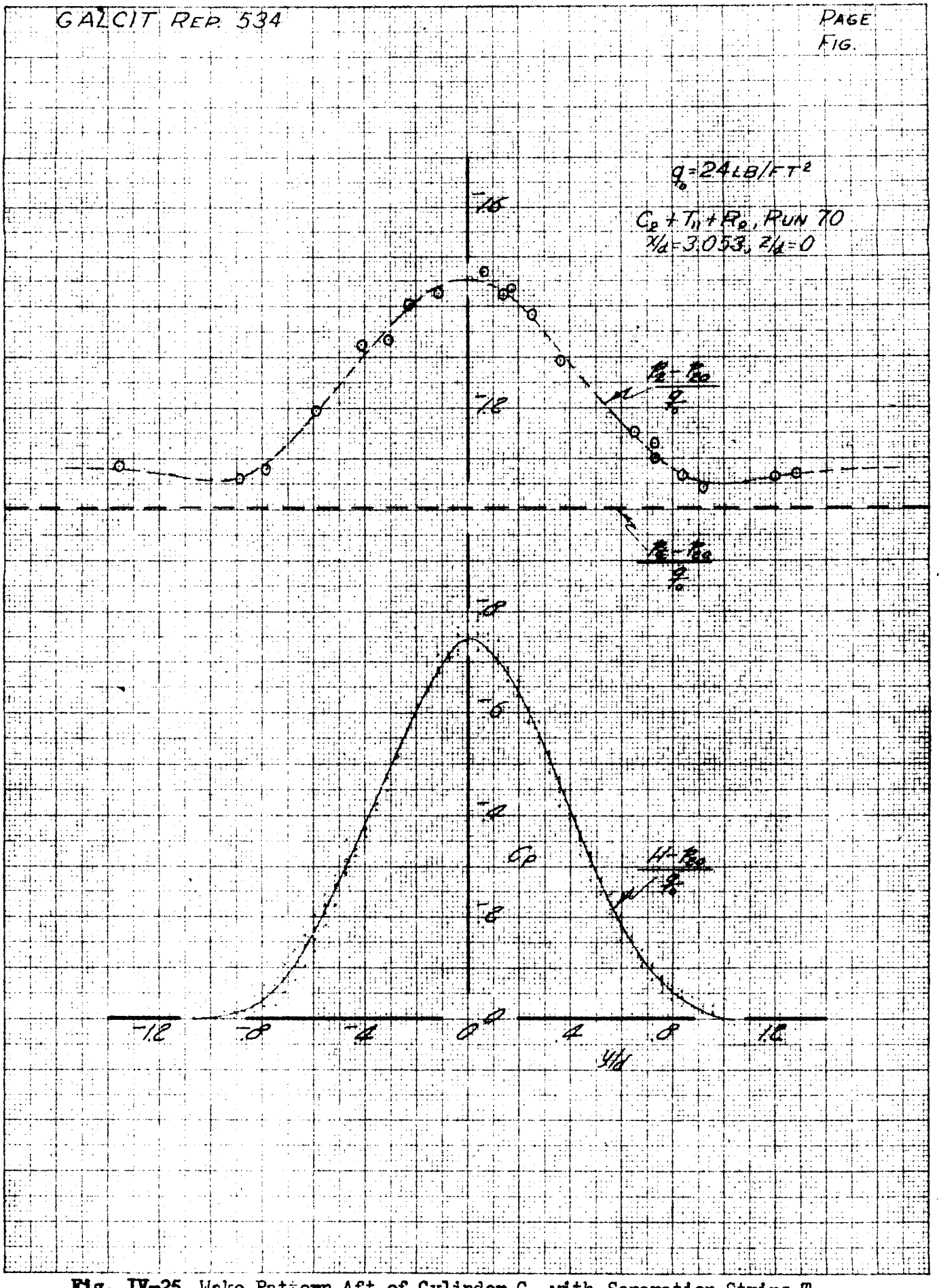

Fig. IV-25 Wake Pattern Aft of Cylinder C_2 with Separation Strips T_{11}, $x/d = 3.053$, $z/d = 0$

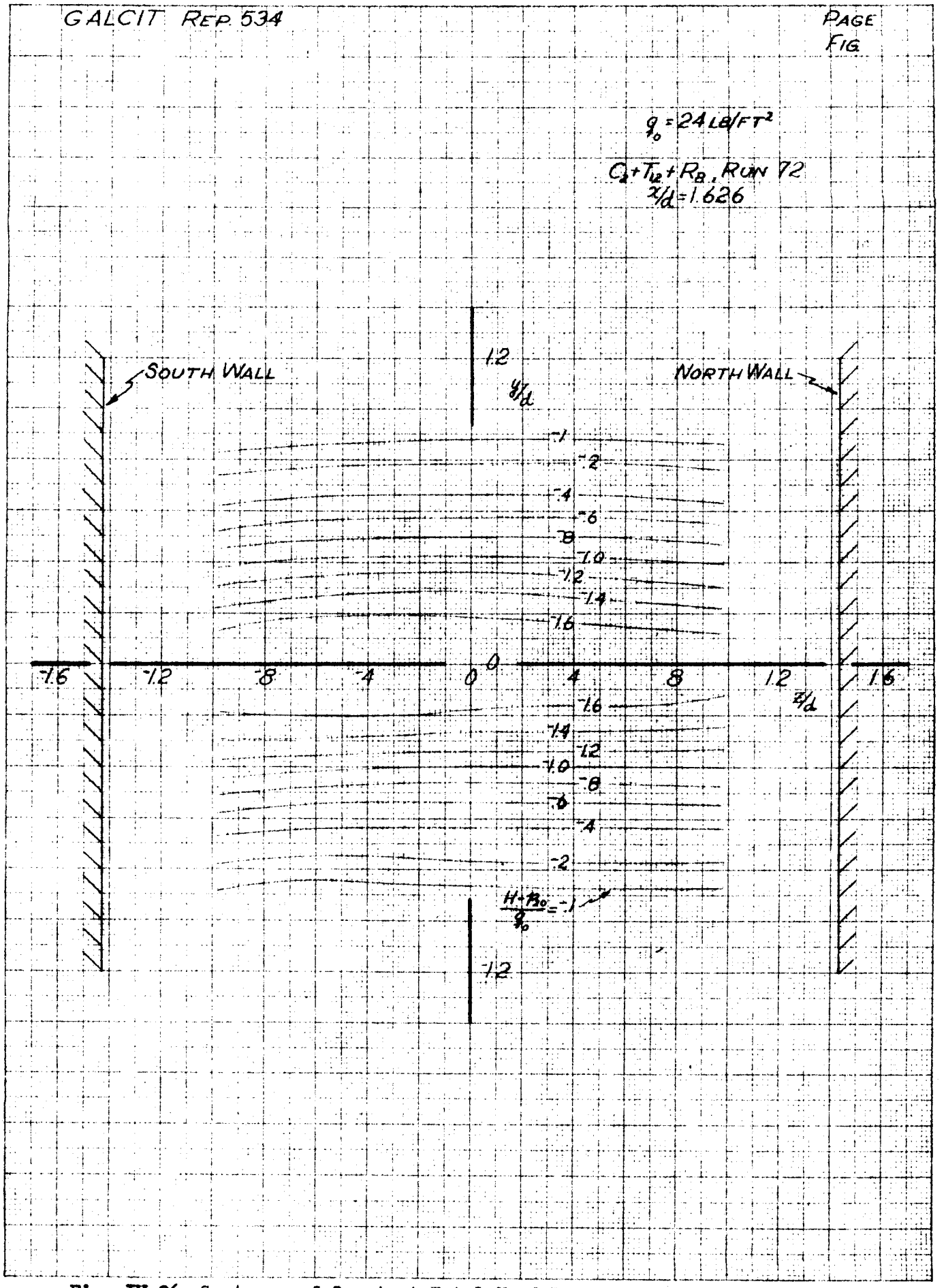

Fig. IV-26 Contours of Constant Total Head Decrements Aft of Cylinder C_2 with Separation Strips T_{12}, x/d = 1.626

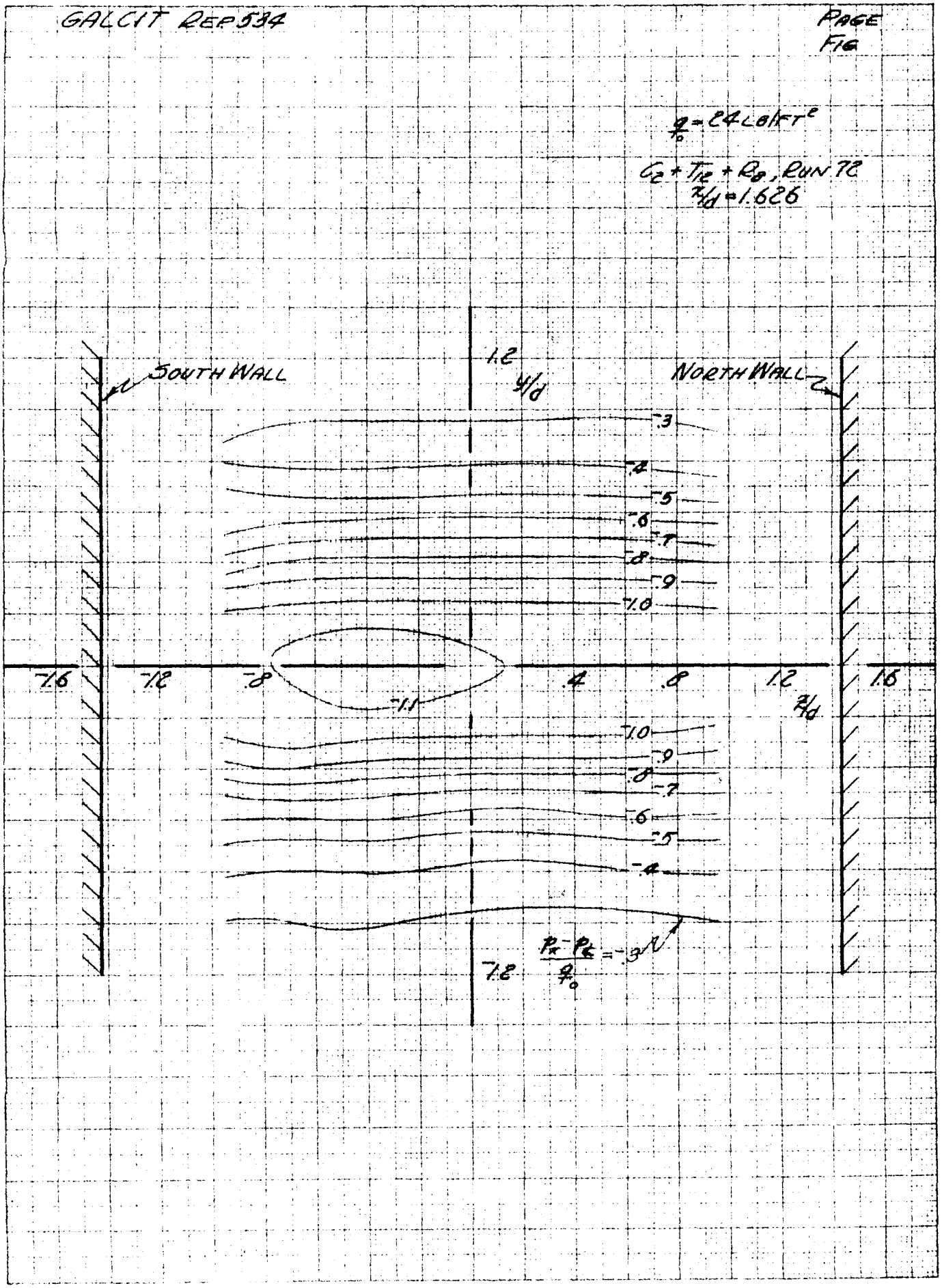

Fig. IV-27 Contours of Constant Static Pressure Decrements Aft of Cylinder C_2 with Separation Strips T_{12}, x/d = 1.626

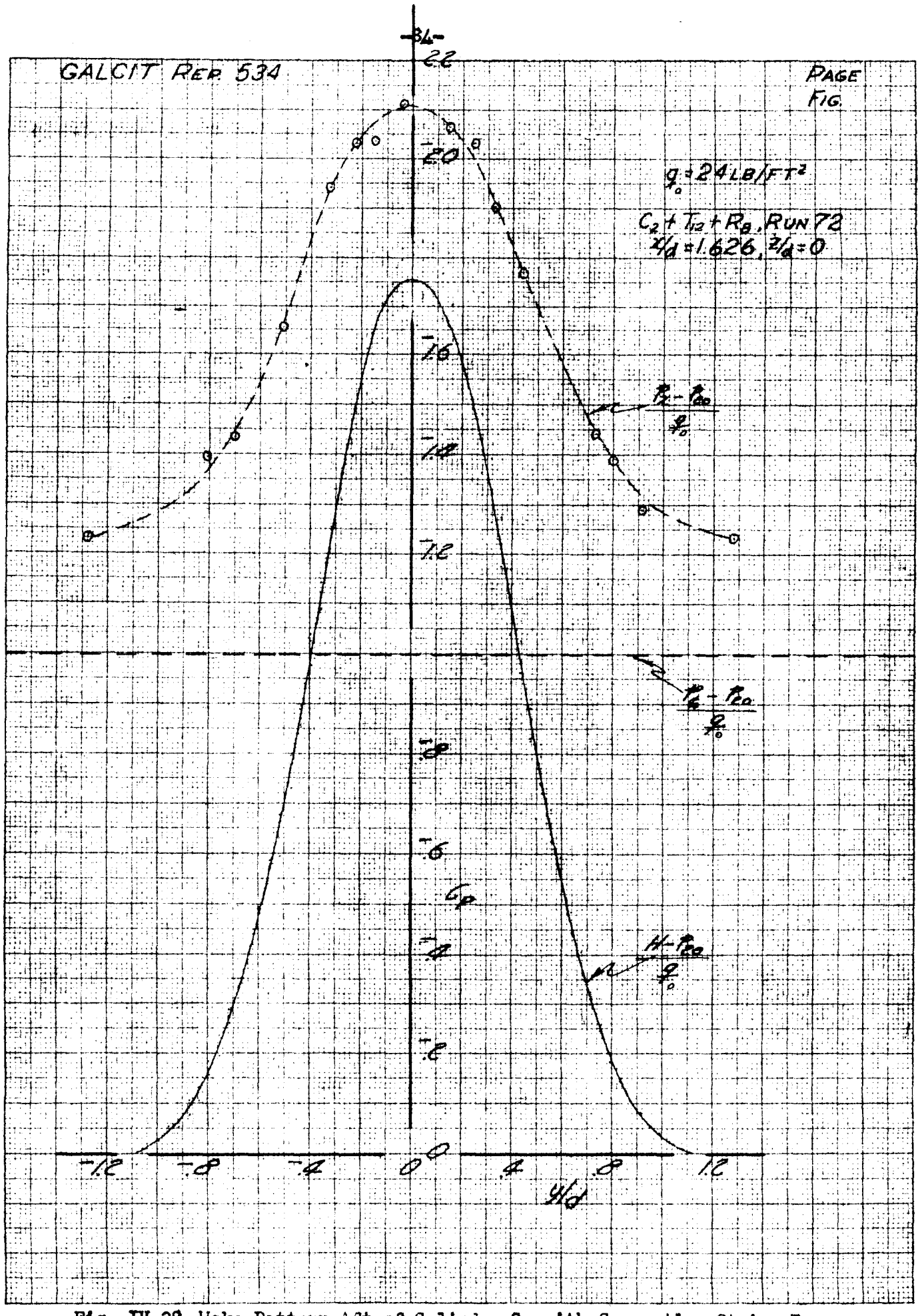

Fig. IV-28 Wake Pattern Aft of Cylinder C_2 with Separation Strips T_{12}, $x/d = 1.626$, $z/d = 0$

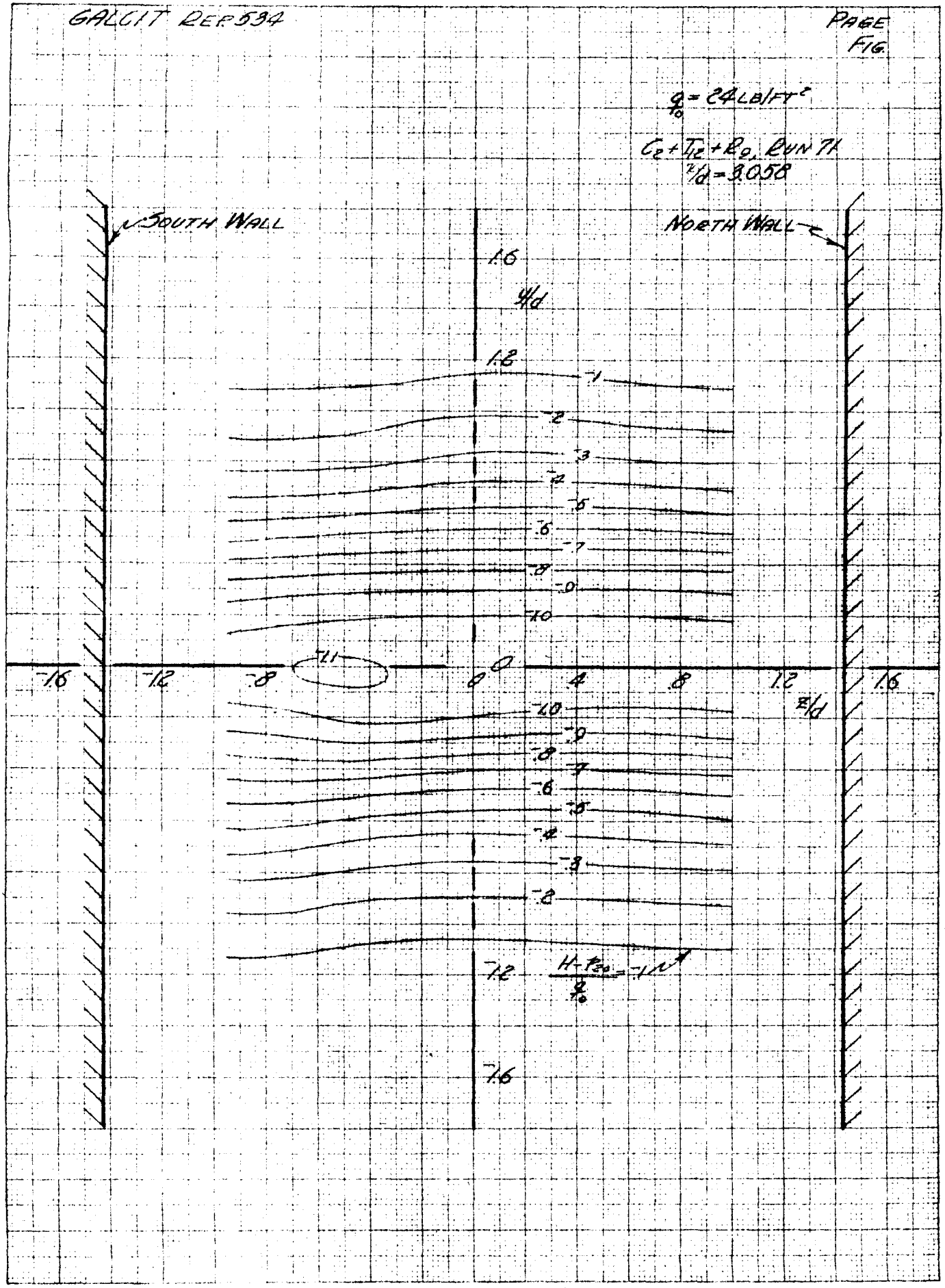

Fig. IV-29 Contours of Constant Total Head Decrements Aft of Cylinder C_2 with Separation Strips T_{12}, x/d = 3.053

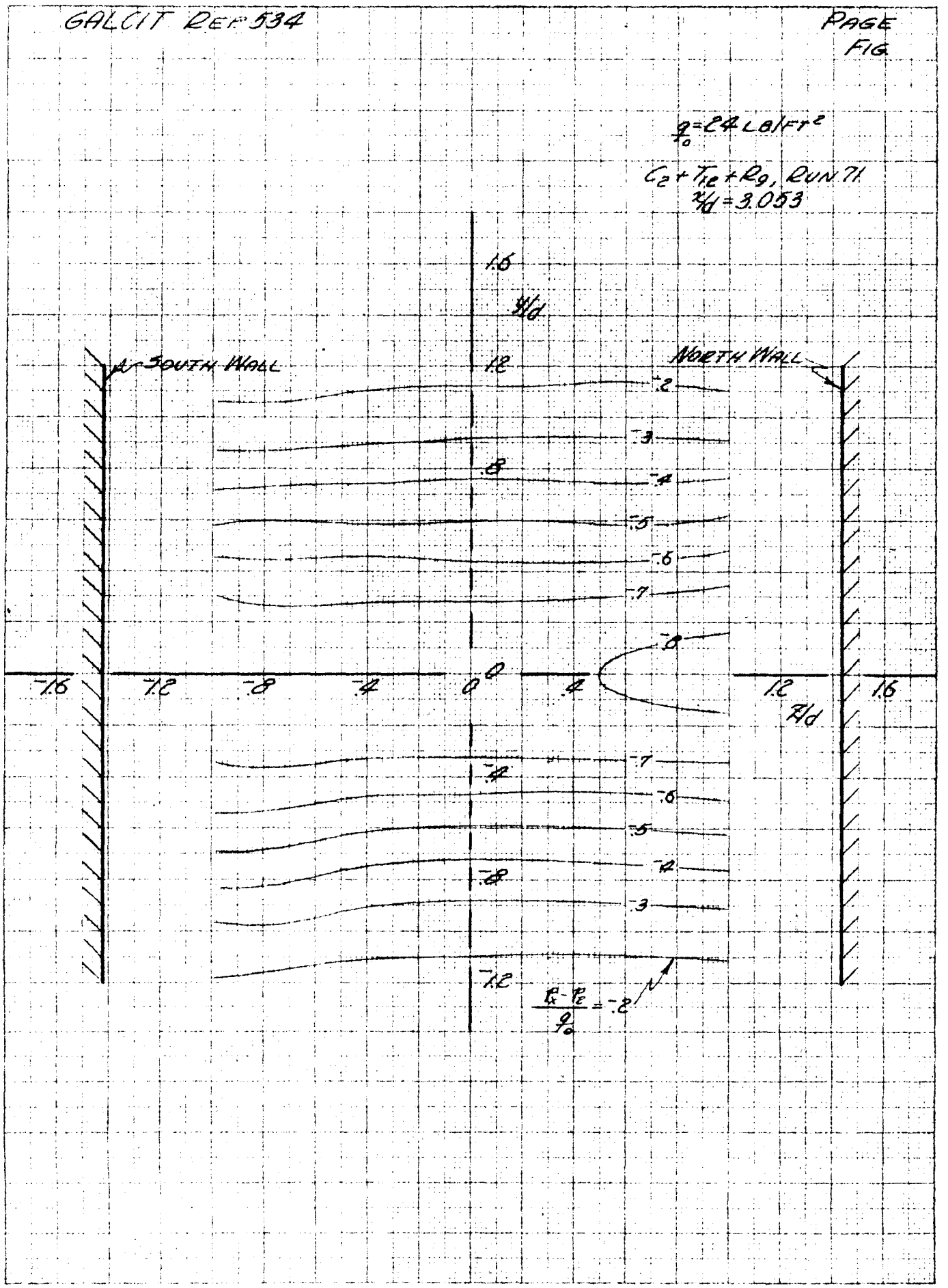

Fig. IV-30 Contours of Constant Static Pressure Decrements Aft of Cylinder C_2 with Separation Strips T_{12}, x/d = 3.053

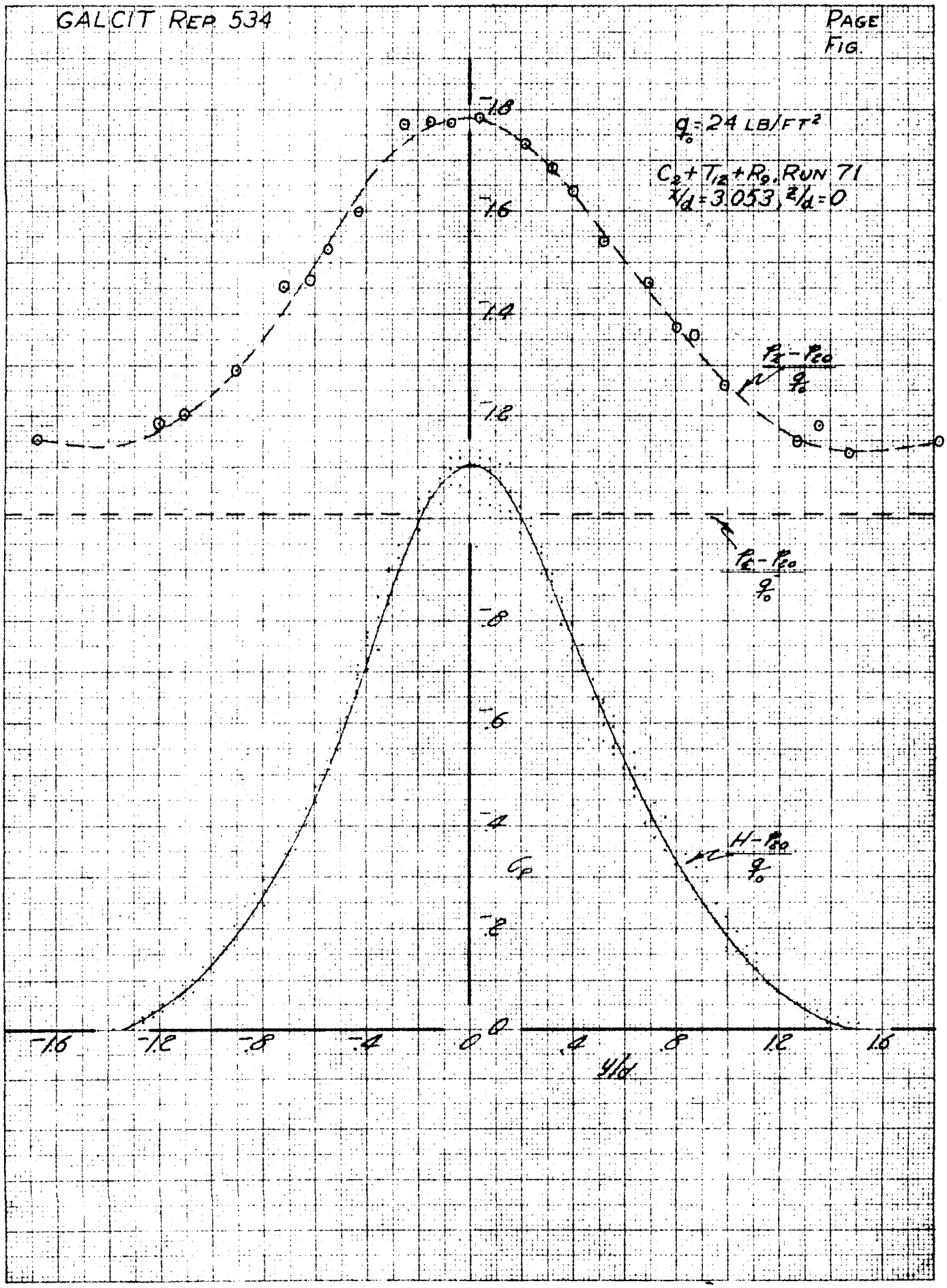

Fig. IV-31 Wake Pattern Aft of Cylinder C_2 with Separation Strips T_{12}, x/d = 3.053, z/d = 0

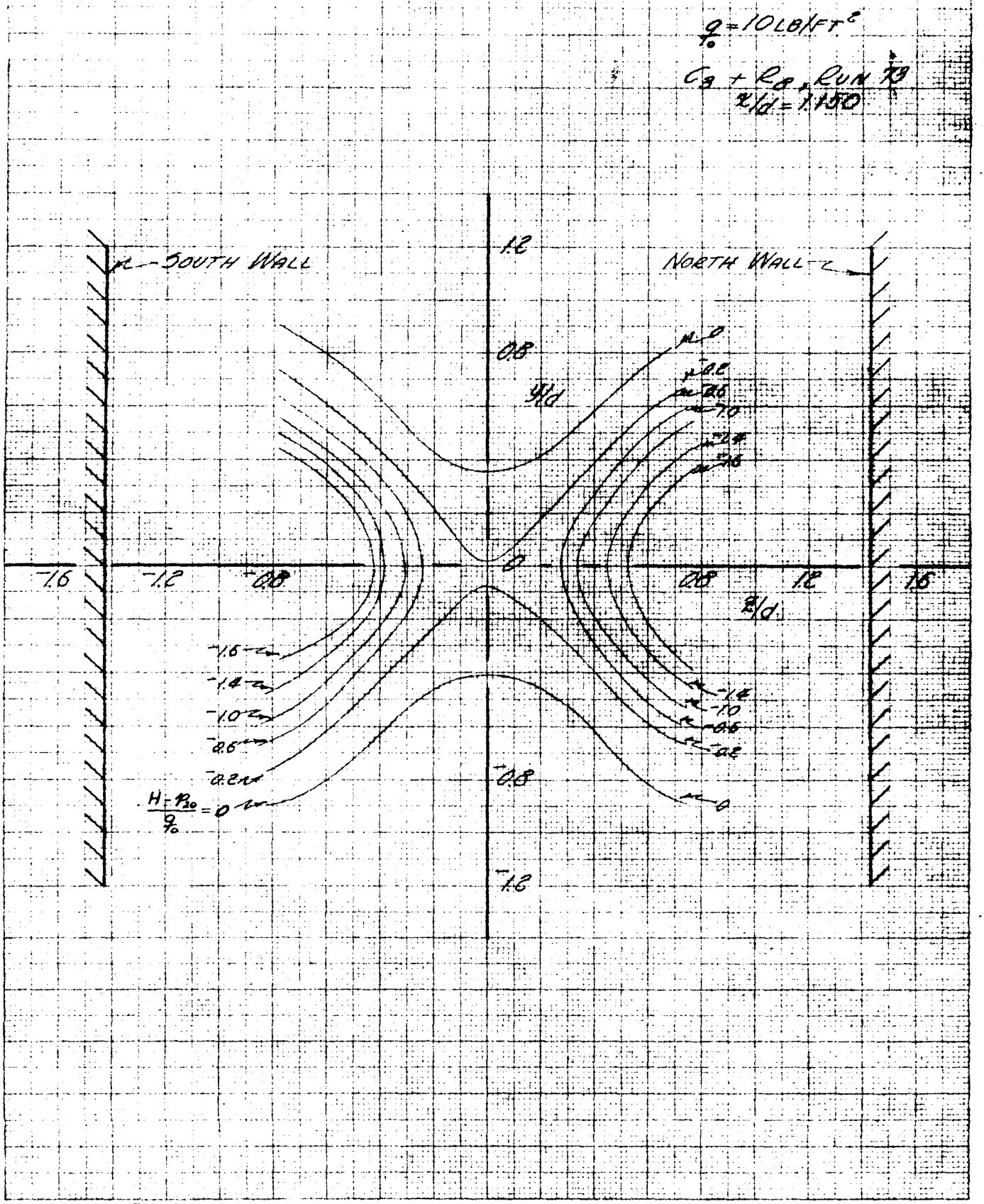

Fig. IV-32 Contours of Constant Total Head Decrements Aft of Cylinder C_3 without Separation Strips, x/d = 1.150

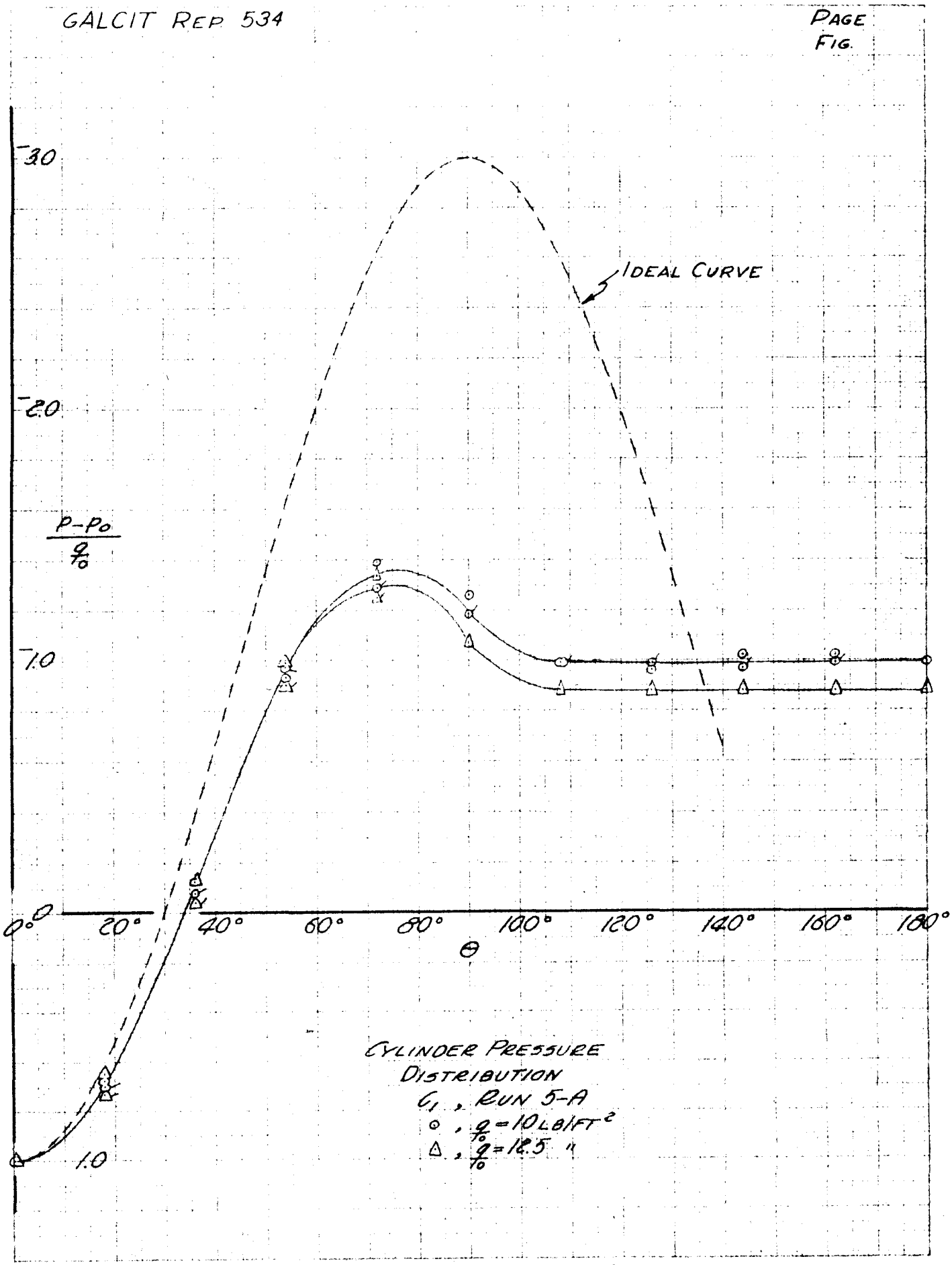

Fig. IV-33 Static Pressure Distribution over Cylinder C_1, q_o = 10 and 12.5 LB/FT^2

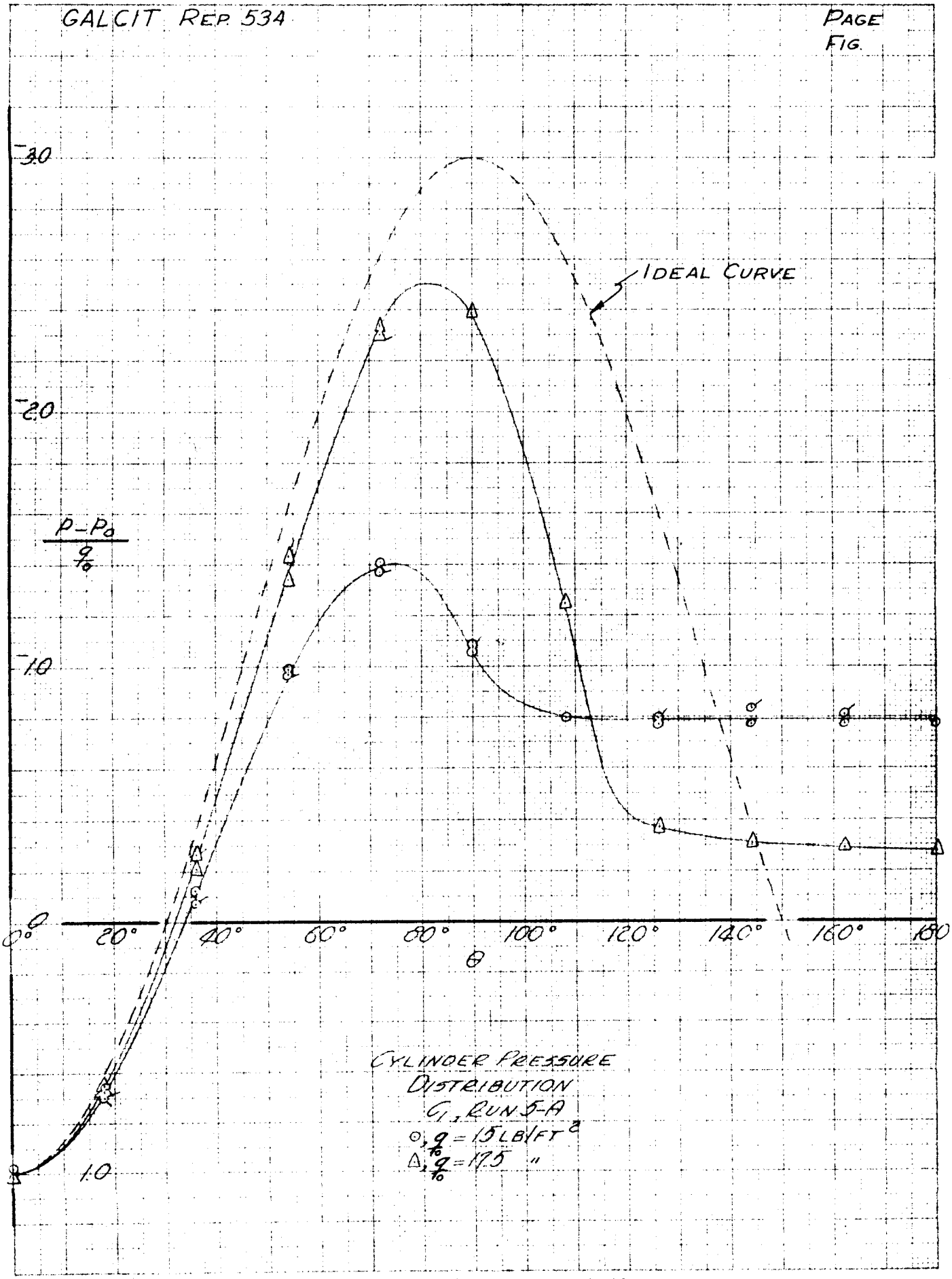

Fig. IV-34 Static Pressure Distribution over Cylinder C_1, q_o = 15 and 17.5 LB/FT^2

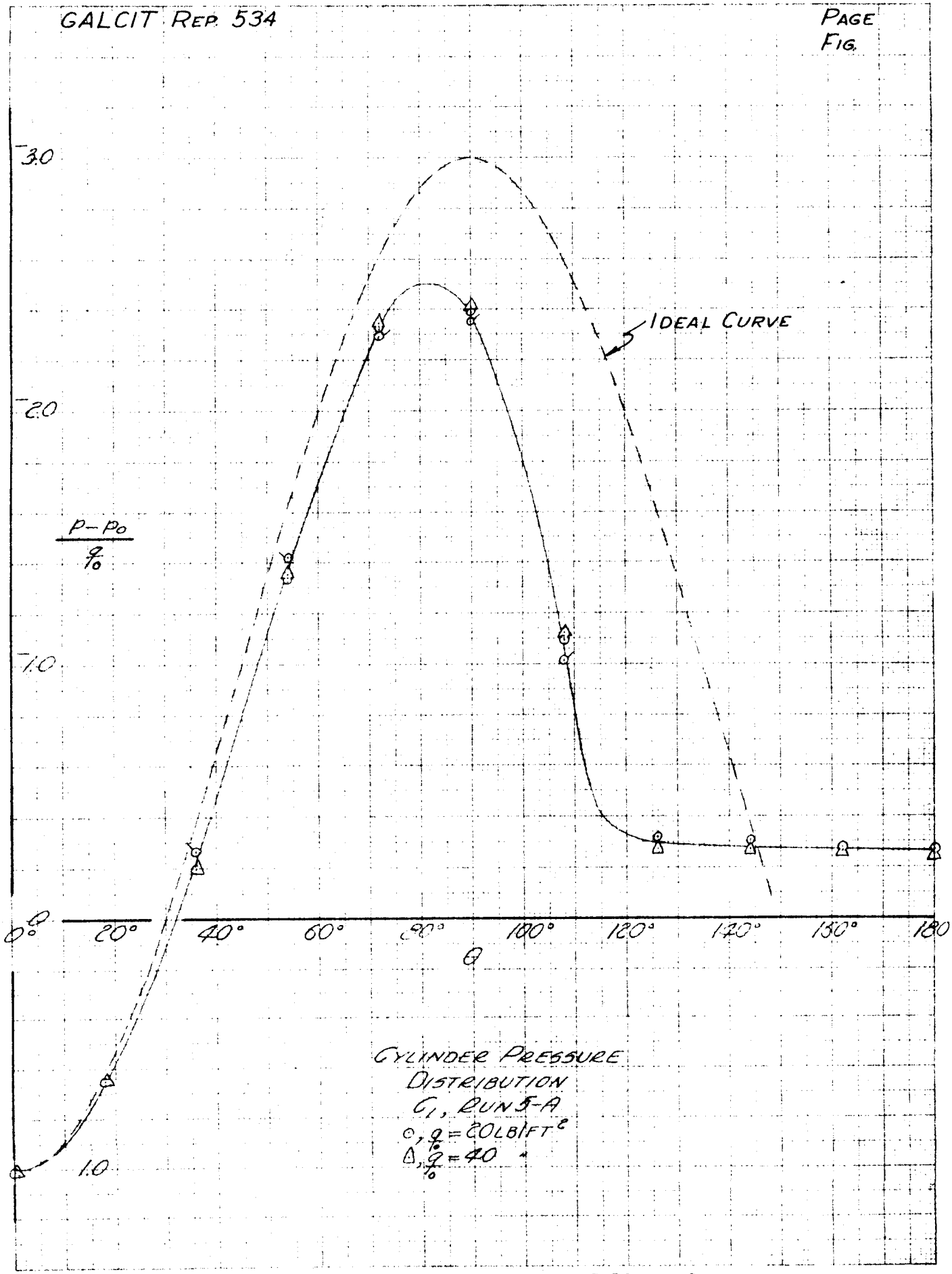

Fig. IV-35 Static Pressure Distribution over Cylinder C_1, q_o = 20 and 40 LB/FT^2

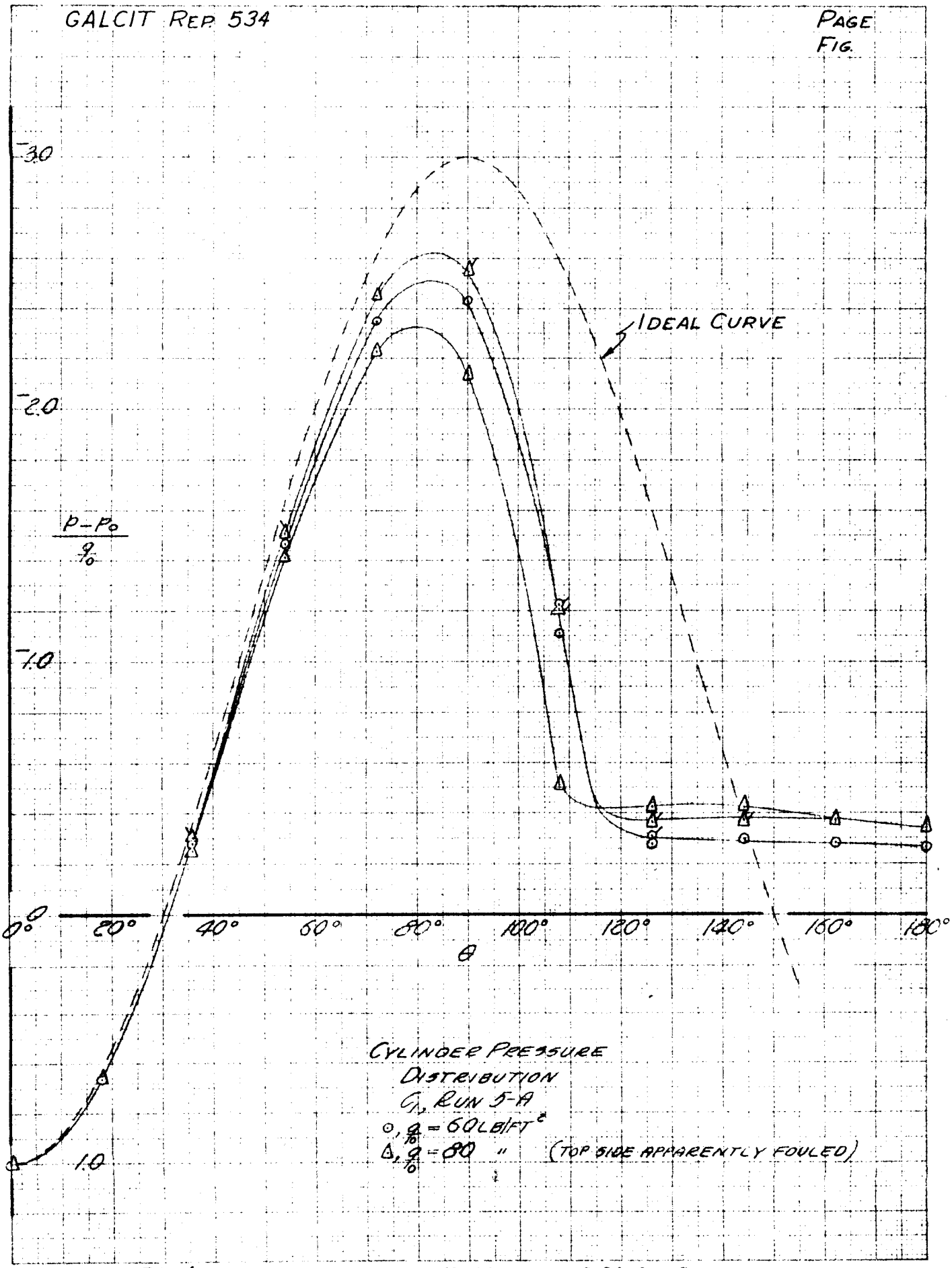

Fig. IV-36 Static Pressure Distribution over Cylinder C_1, q_o = 60 and 80 LB/FT^2

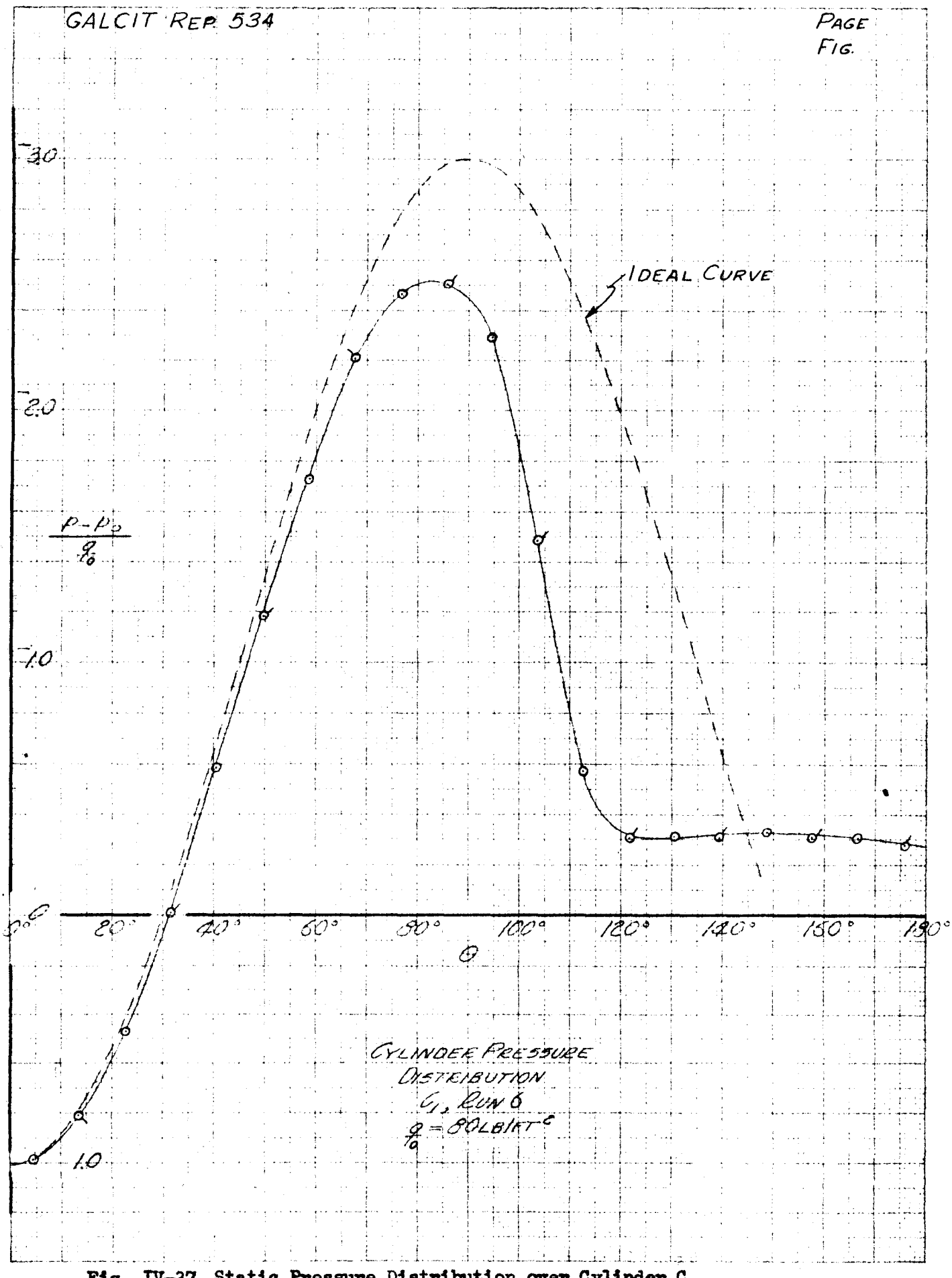

Fig. IV-37 Static Pressure Distribution over Cylinder C_1, q_0 = 80 LB/FT^2

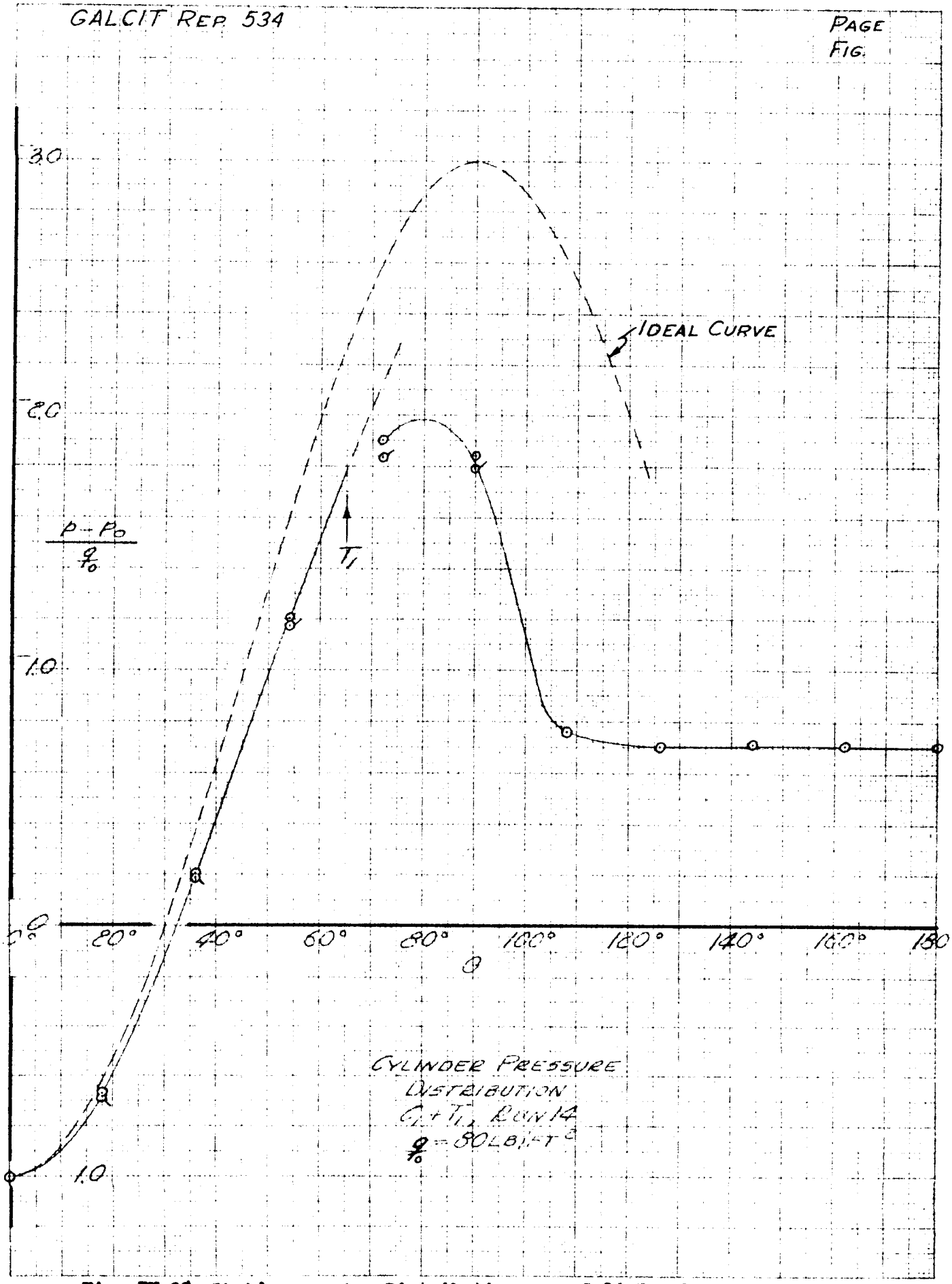

Fig. IV-38 Static pressure Distribution over Cylinder C_1 with Separation Strips T_1, q_0 = 80 LB/FT²

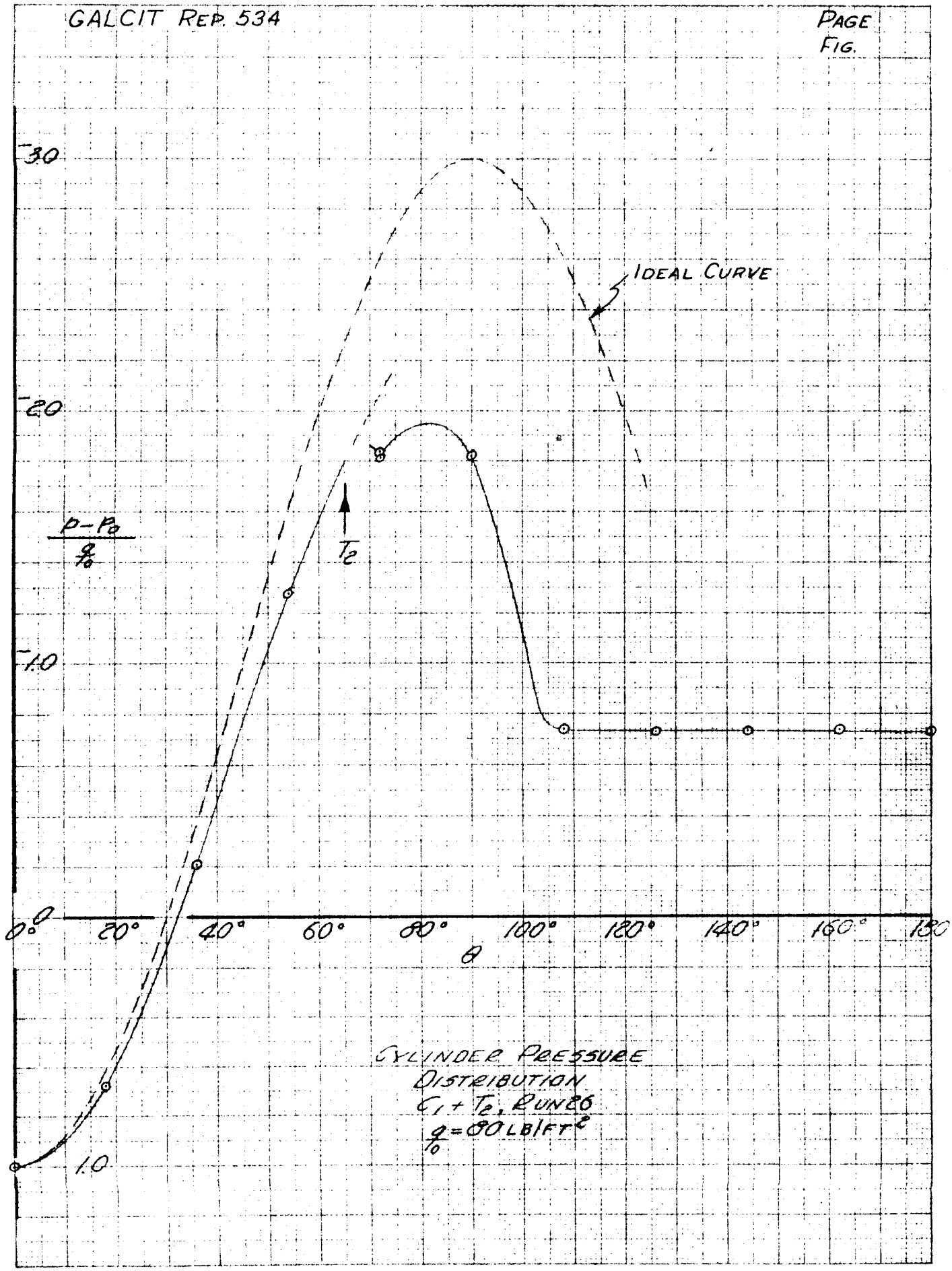

Fig. IV-39 Static Pressure Distribution over Cylinder C_1 with Separation Strips T_2, q_o = 80 LB/FT²

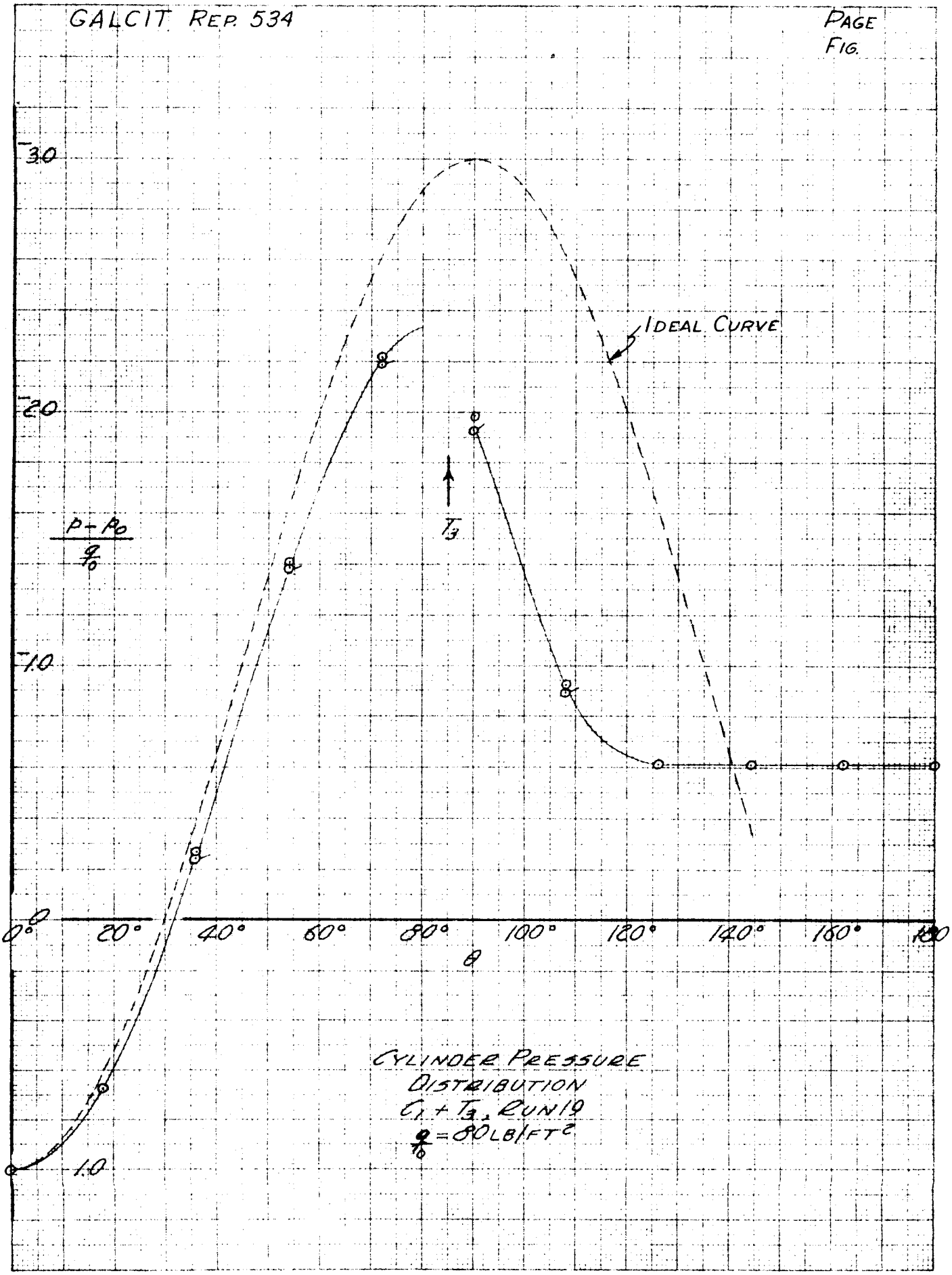

Fig. IV-40 Static Pressure Distribution over Cylinder C_1 with Separation Strips T_3, q_o = 80 LB/FT^2

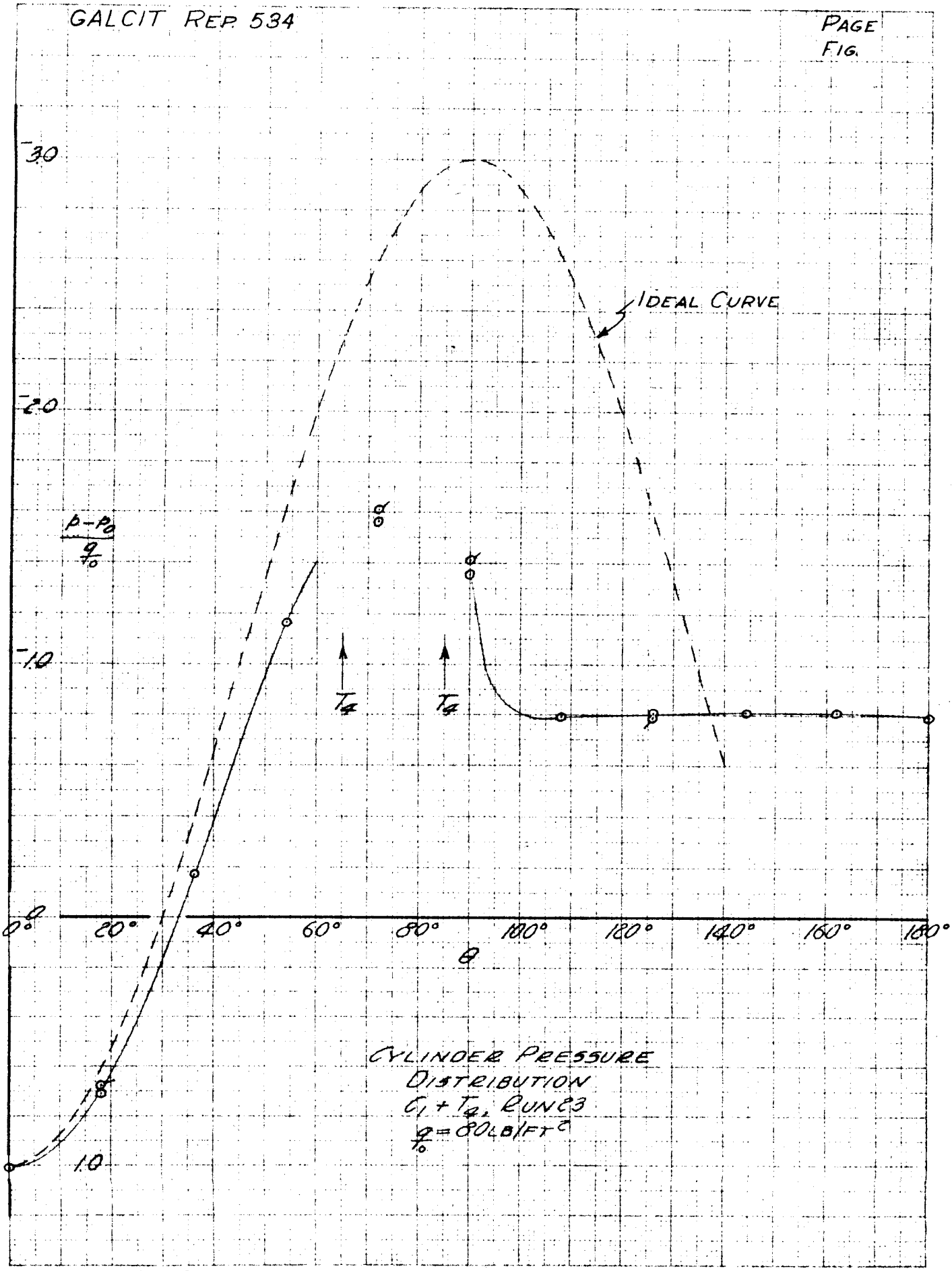

Fig. IV-41 Static Pressure Distribution over Cylinder C_1 with Separation Strips T_4, q_0 = 80 LB/FT²

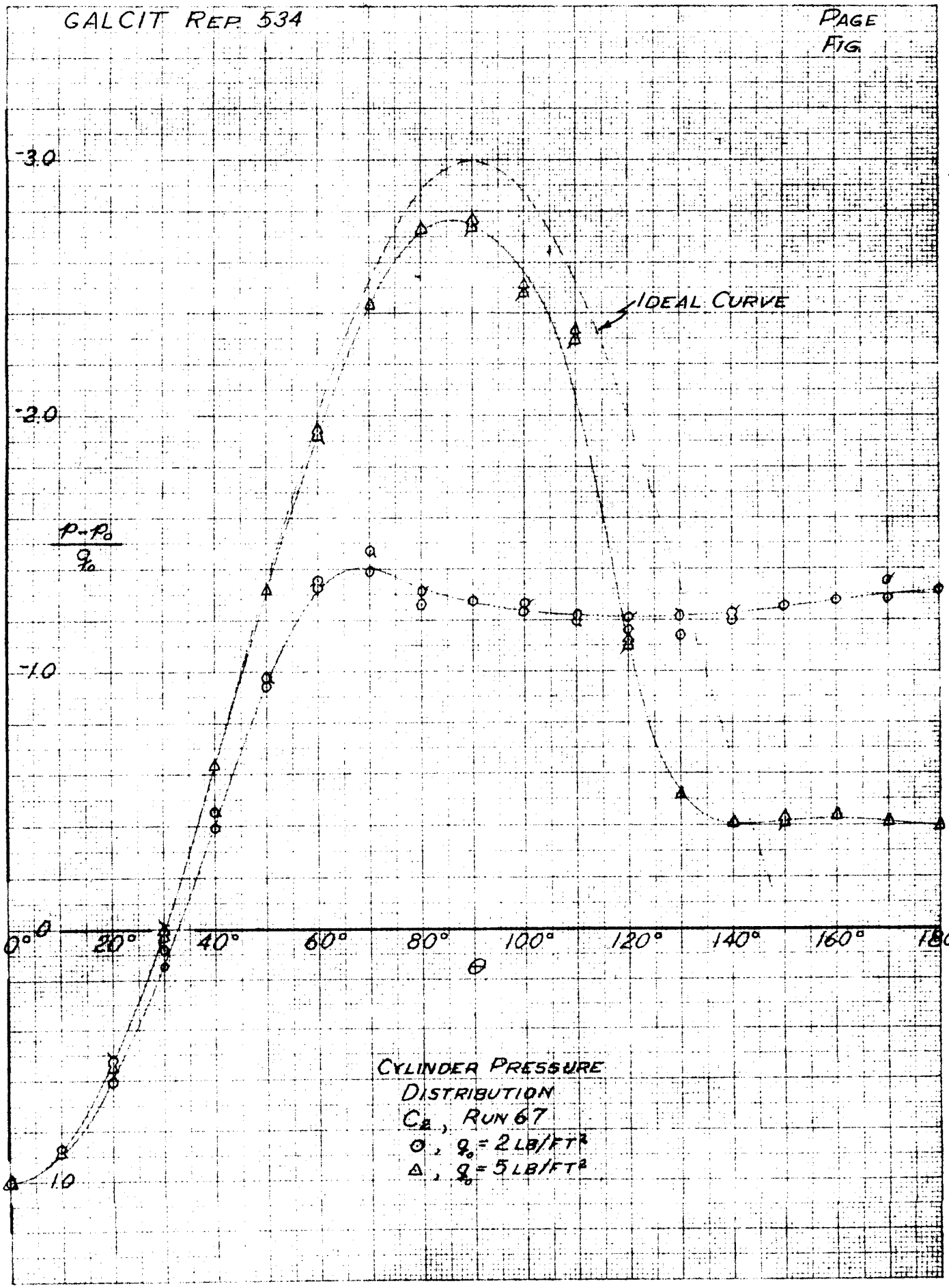

Fig. IV-42 Static Pressure Distribution over Cylinder C_2, q_o = 2 and 5 LB/FT2

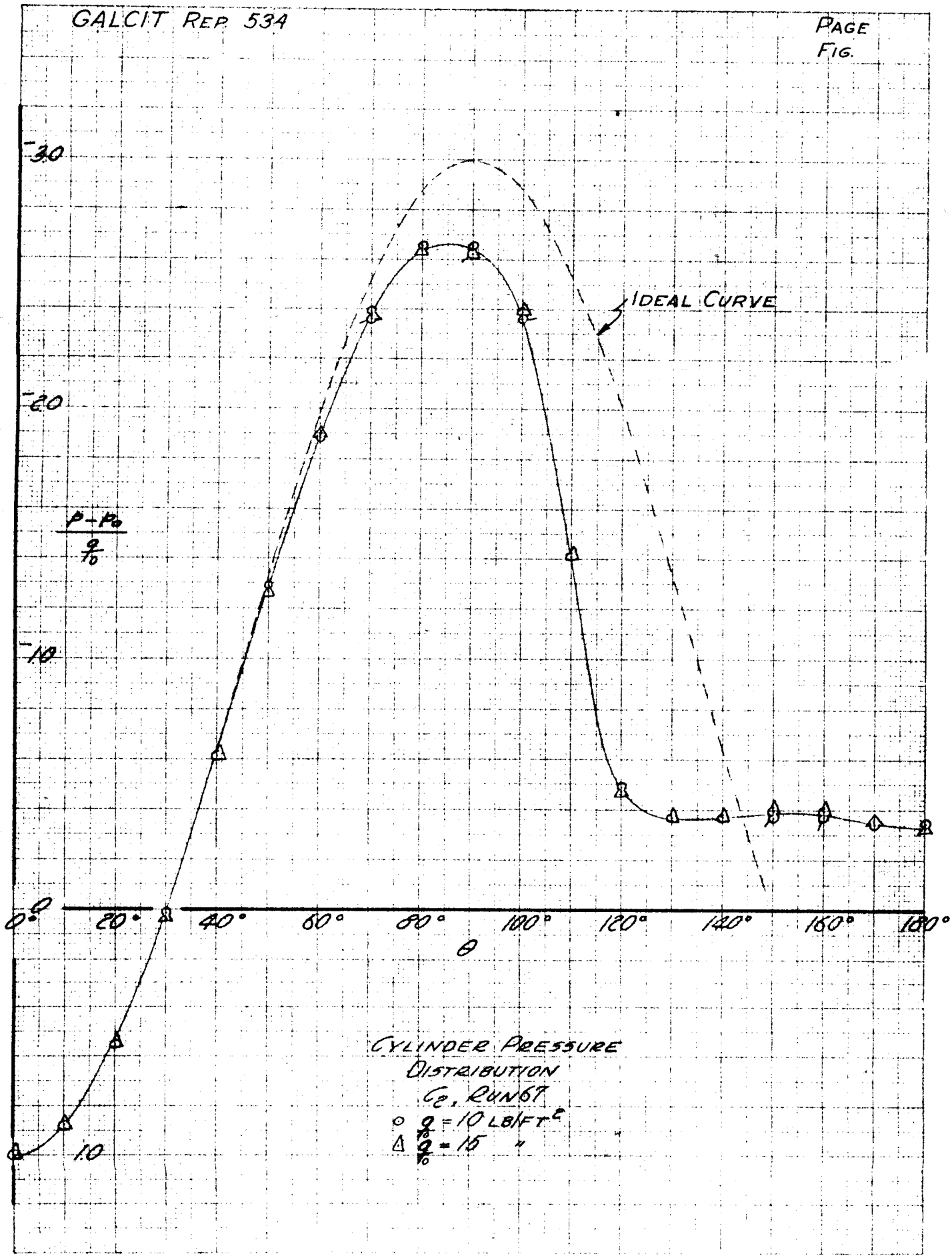

Fig. IV-43 Static Pressure Distribution over Cylinder C_2, q_o = 10 and 15 LB/FT^2

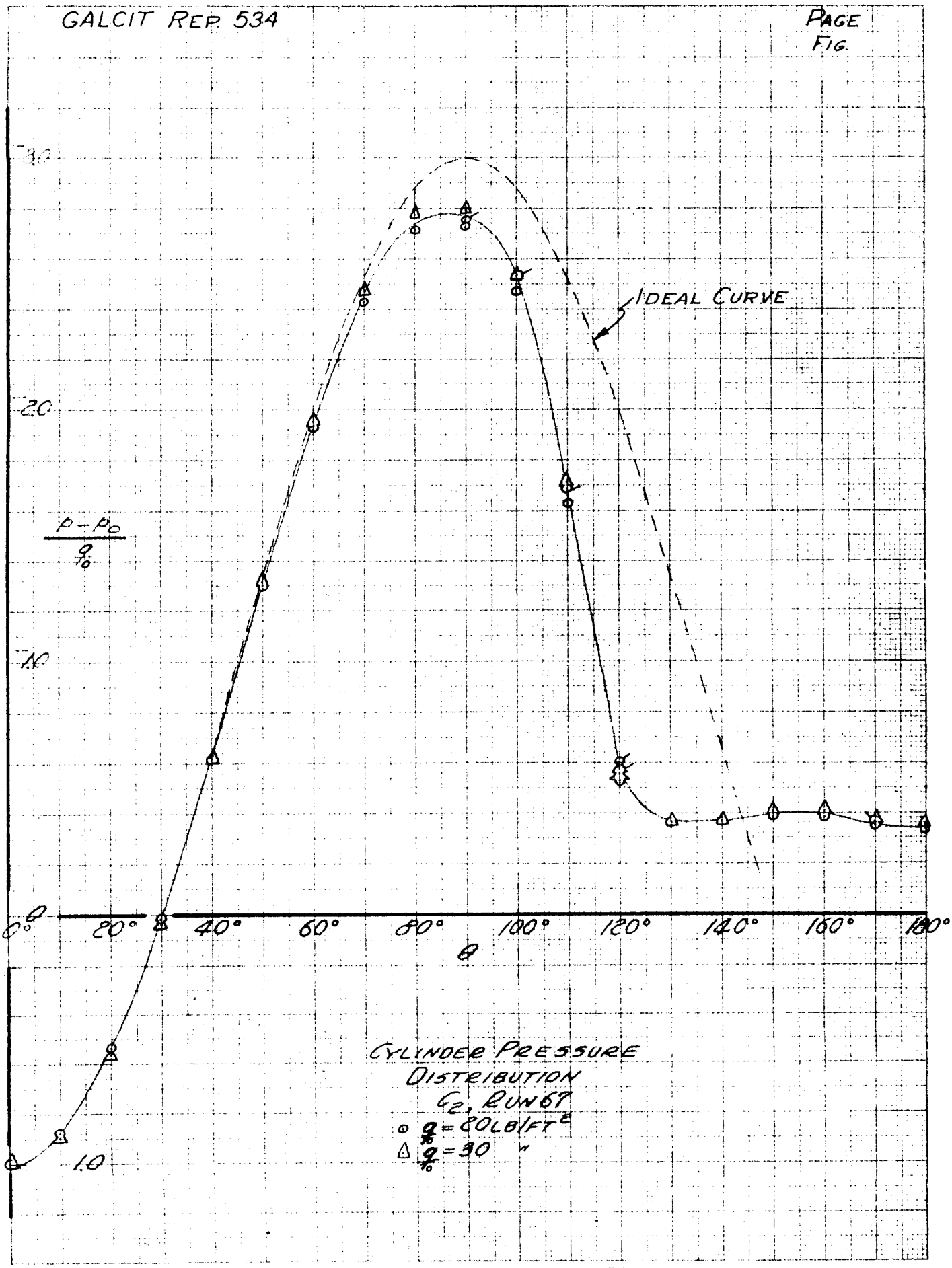

Fig. IV-44 Static Pressure Distribution over Cylinder C_2, q_o = 20 and 30 LB/FT^2

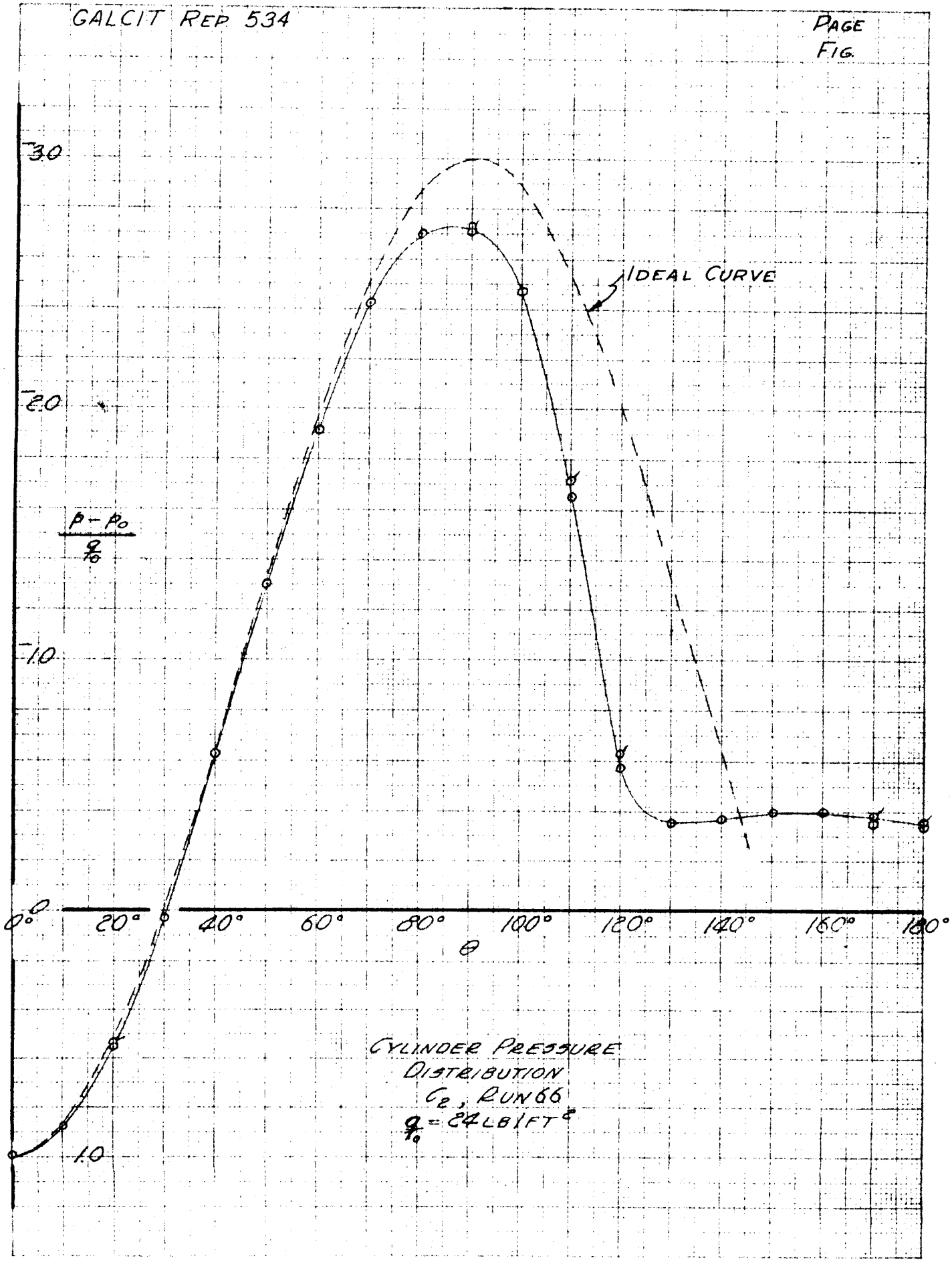

Fig. IV-45 Static Pressure Distribution over Cylinder C_2, q_0 = 24 LB/FT^2

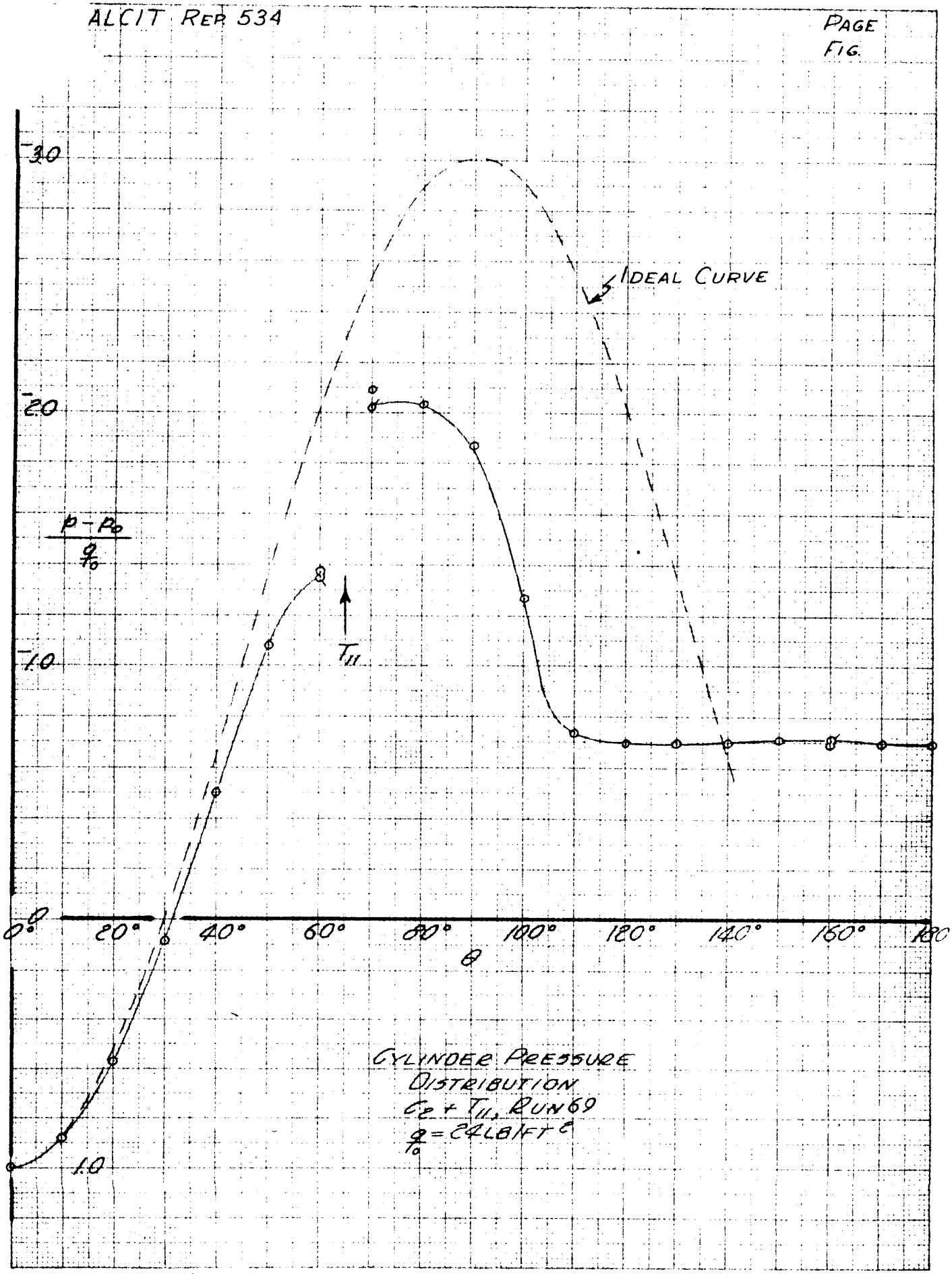

Fig. IV-46 Static Pressure Distribution over Cylinder C_2 with Transition Strips T_{11}, q_0 = 24 LB/FT^2

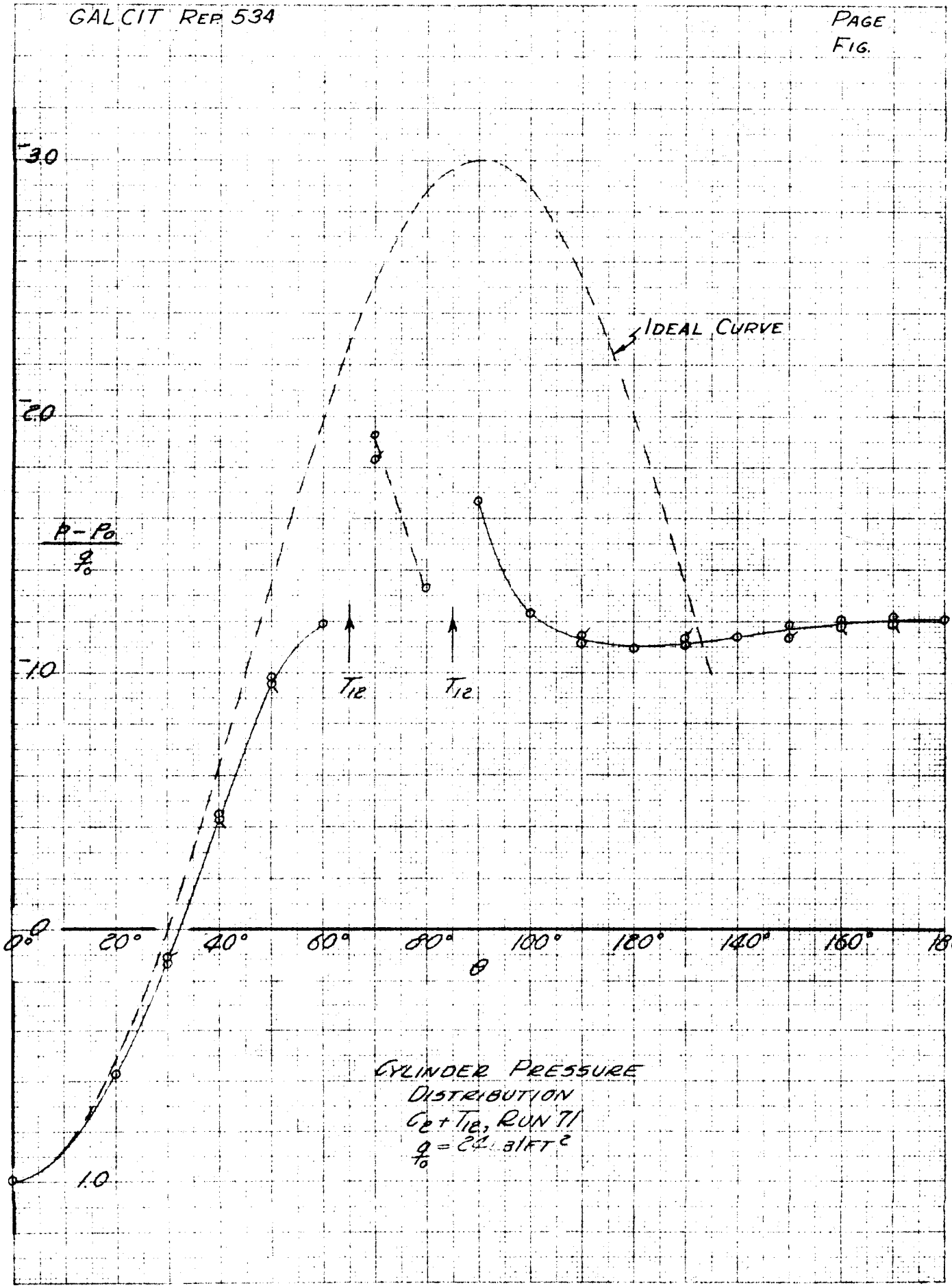

Fig. IV-47 Static Pressure Distribution over Cylinder C_2 with Separation Strips T_{12}, q_0 = 24 LB/FT^2

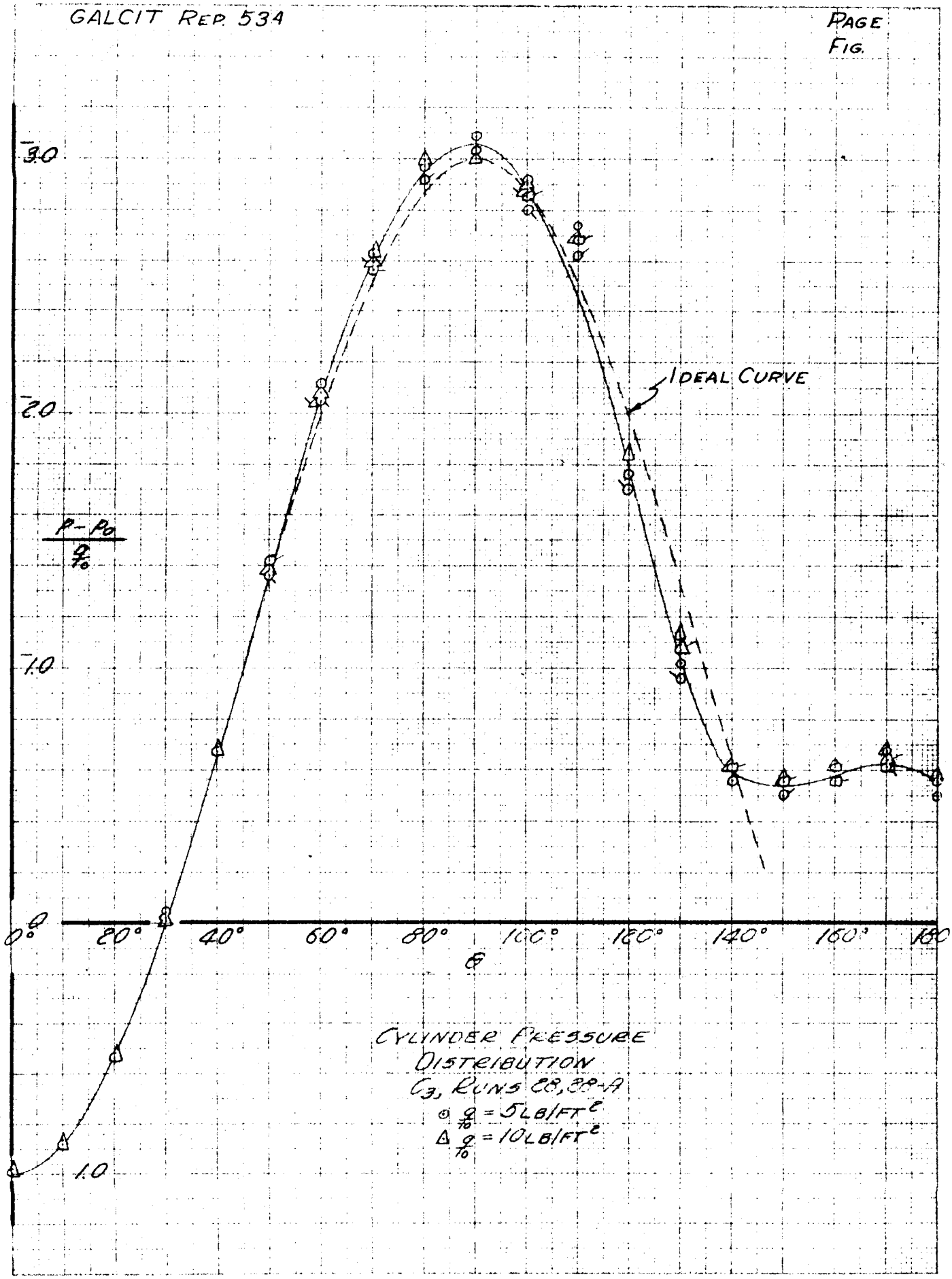

Fig. IV-48 Static Pressure Distribution over Cylinder C_3, q_0 = 5 and 10 LB/FT²

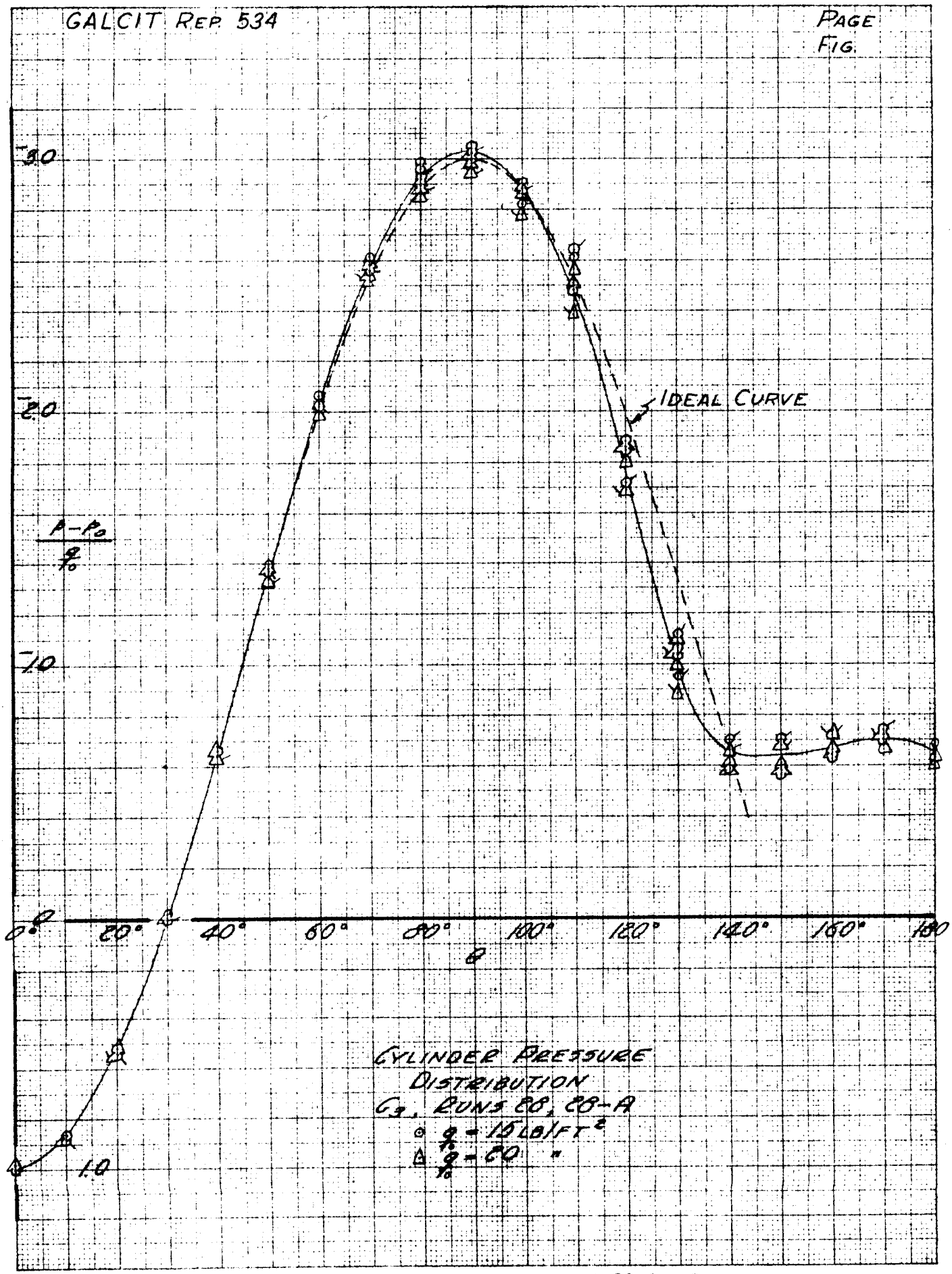

Fig. IV-49 Static Pressure Distribution over Cylinder C_3, q_o = 15 and 20 LB/FT^2

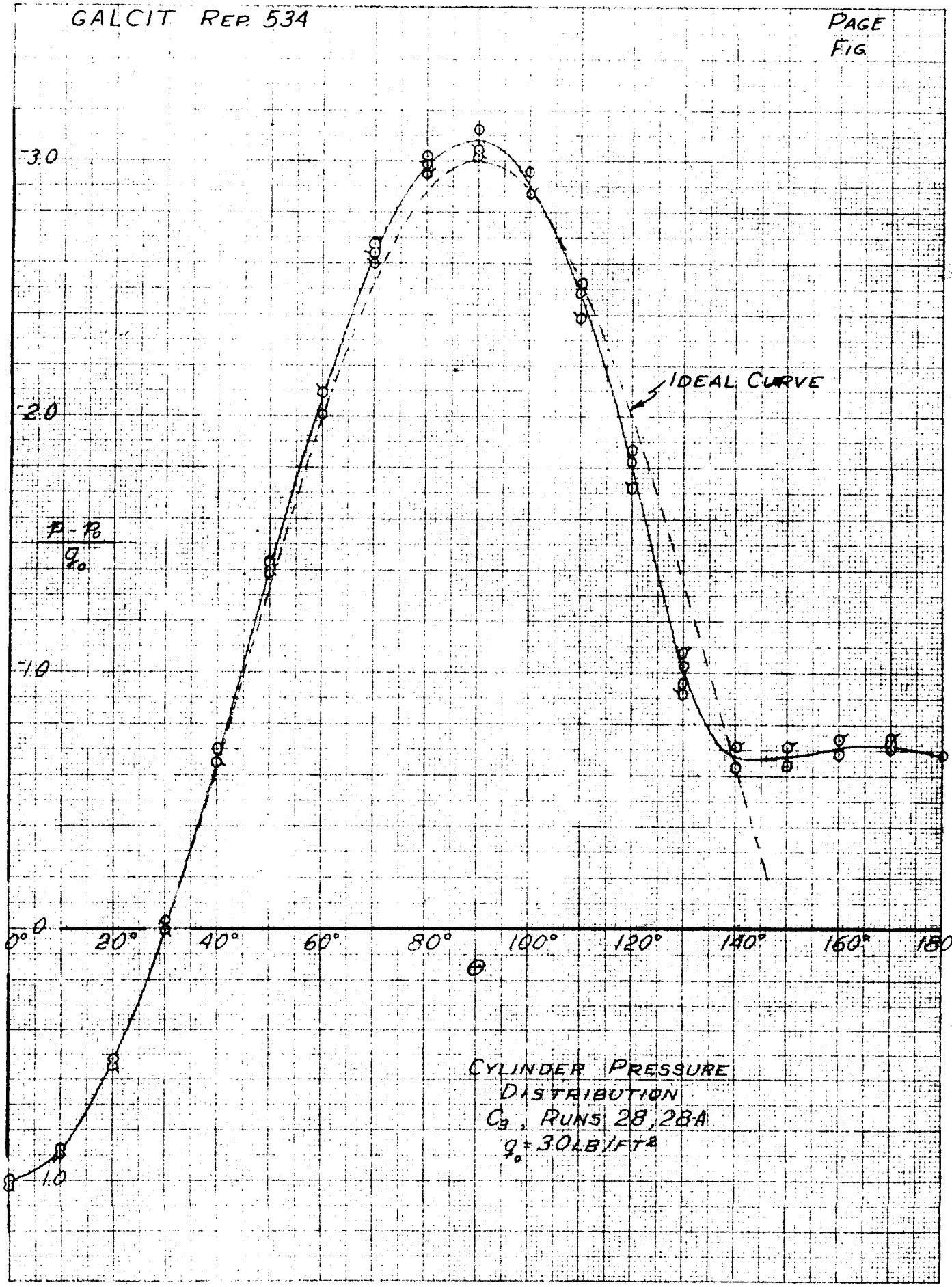

Fig. IV-50 Static Pressure Distribution over Cylinder C_3, q_o = 30 LB/FT^2

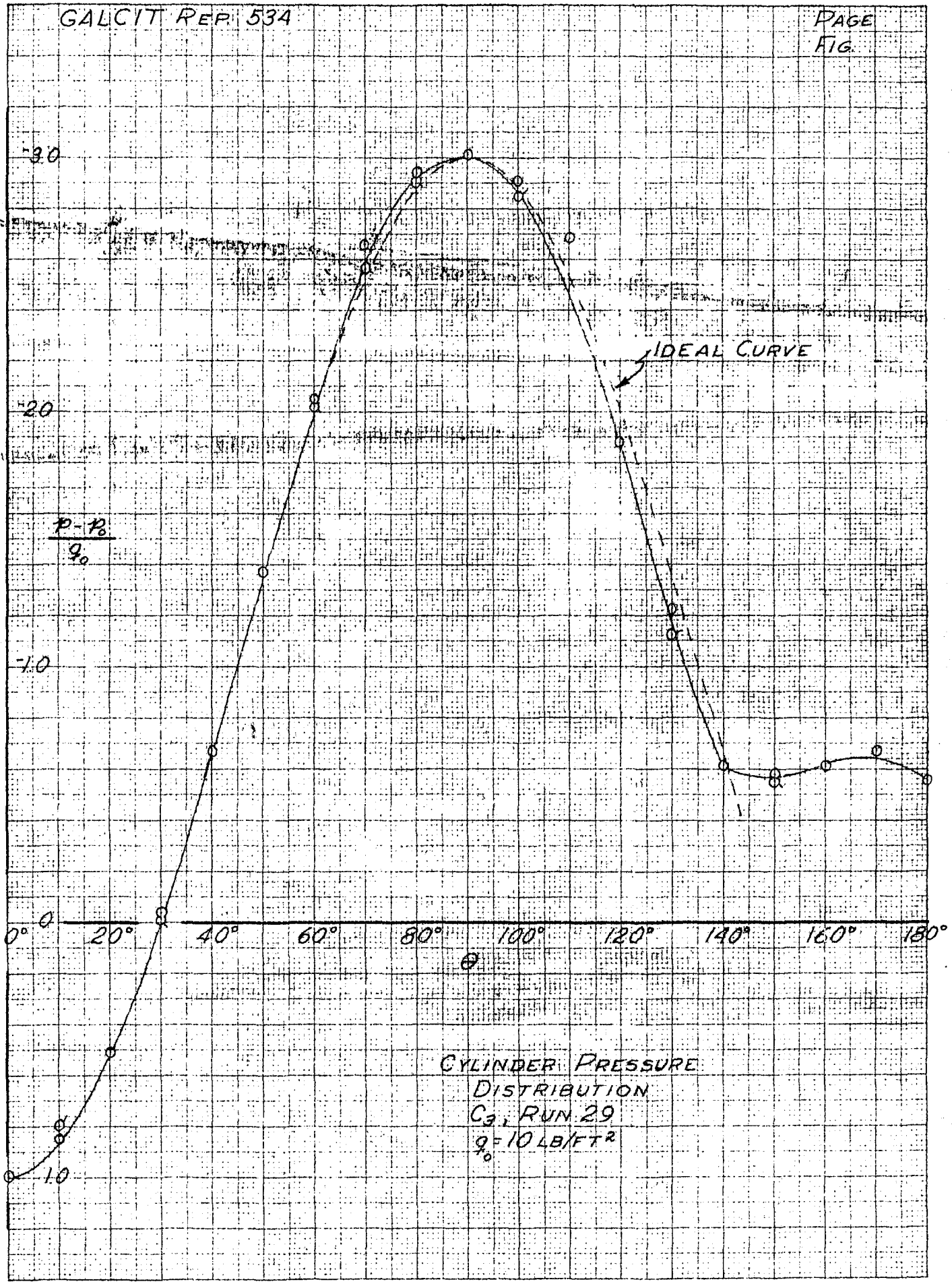

Fig. IV-51 Static Pressure Distribution over Cylinder C_3, q_0 = 10 LB/FT^2

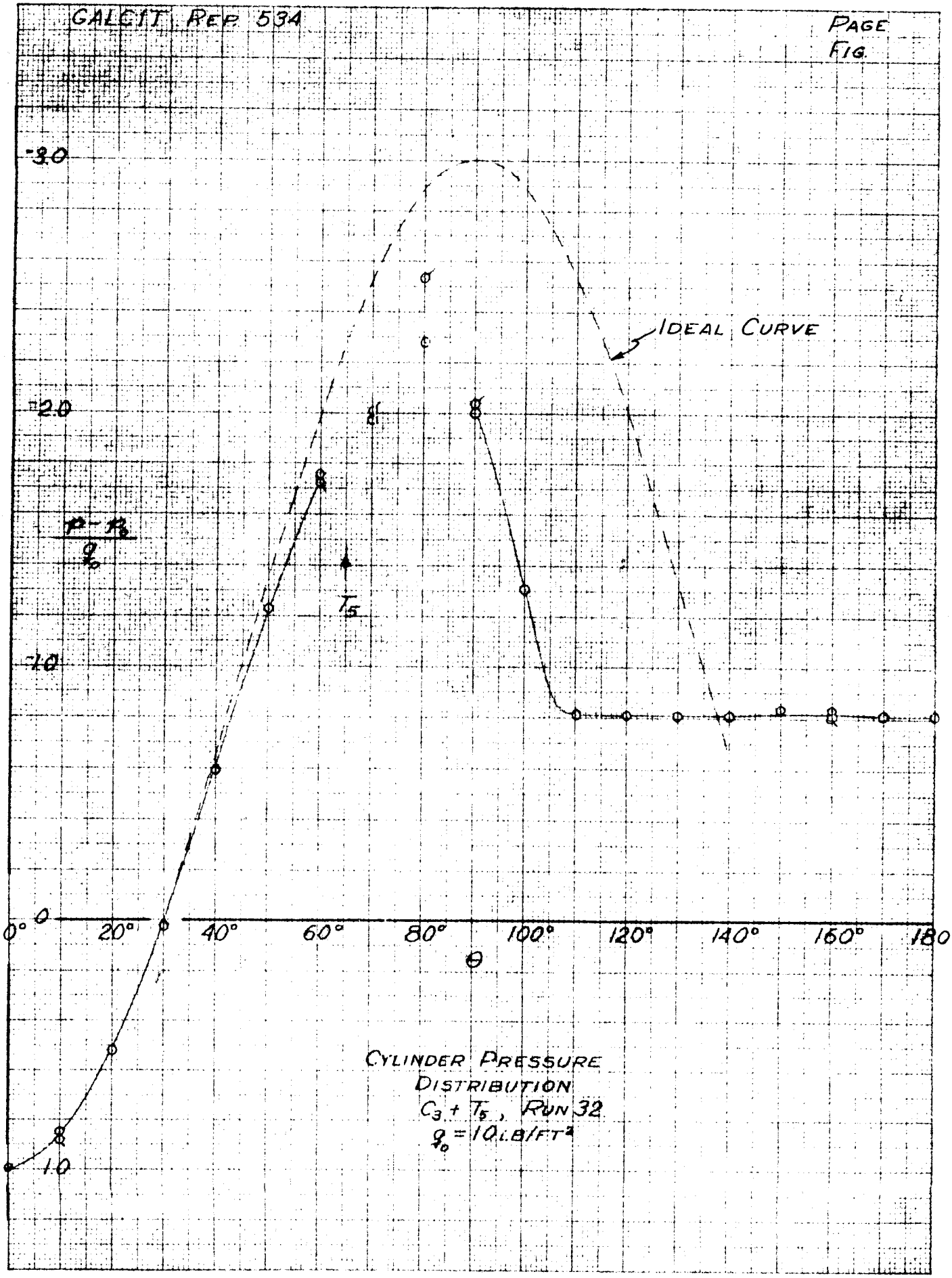

Fig. IV-52 Static Pressure Distribution over Cylinder C_3 with Separation Strips T_5, q_0 = 10 LB/FT²

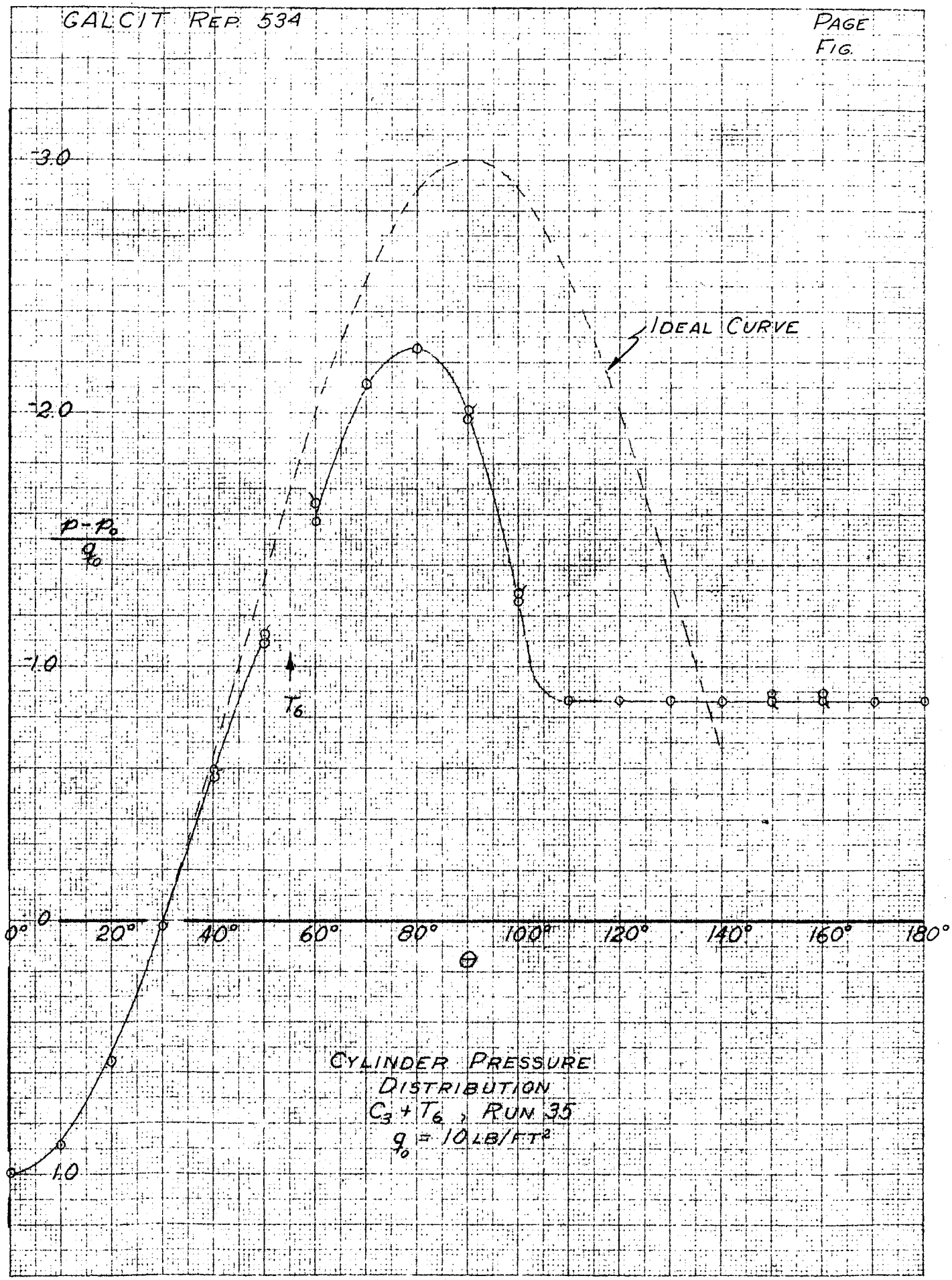

Fig. IV-53 Static Pressure Distribution over Cylinder C_3 with Separation Strips T_6, q_0 = 10 LB/FT^2

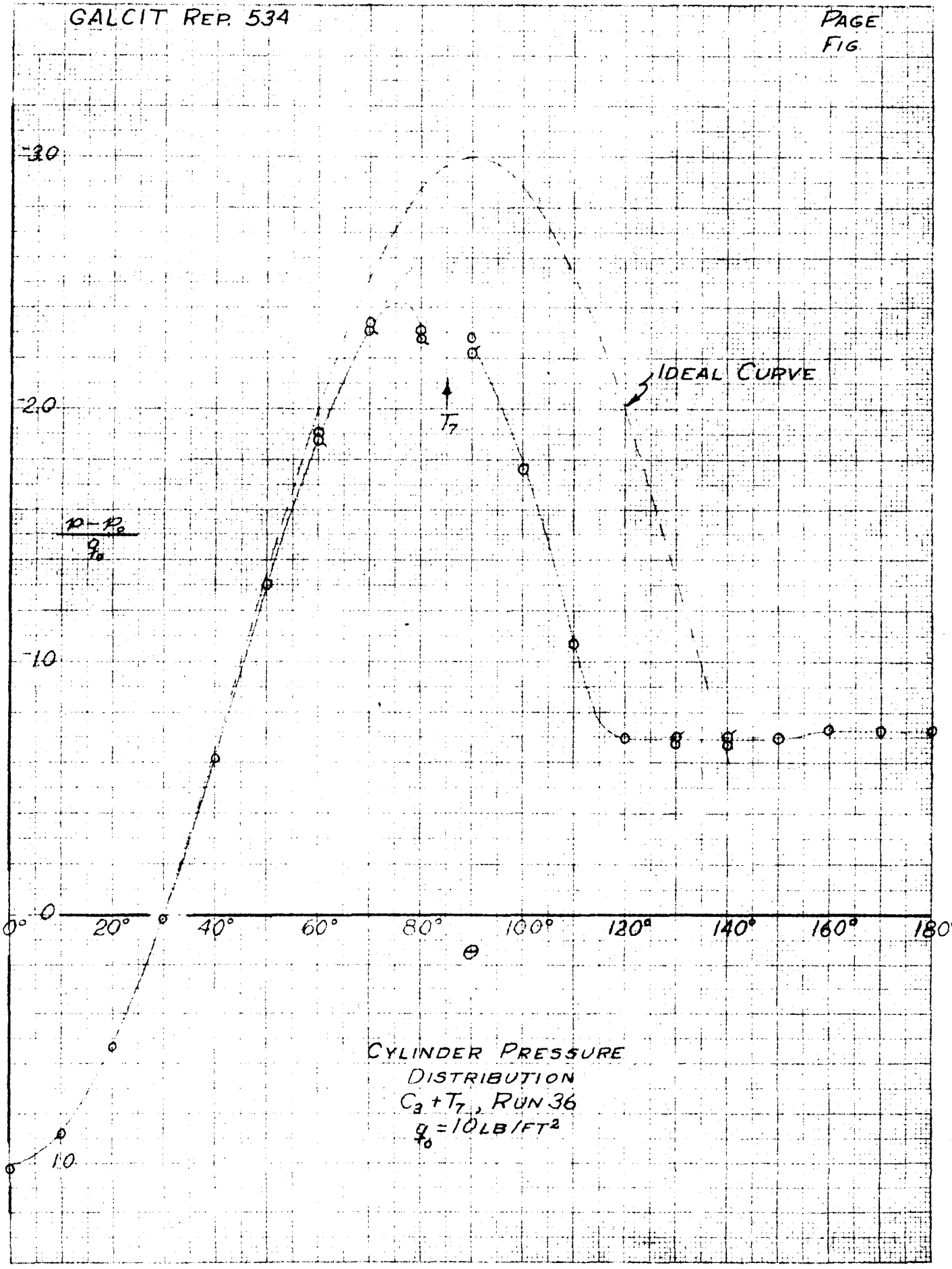

Fig. IV-54 Static Pressure Distribution over Cylinder C_3 with Separation Strips T_7, q_o = 10 LB/FT²

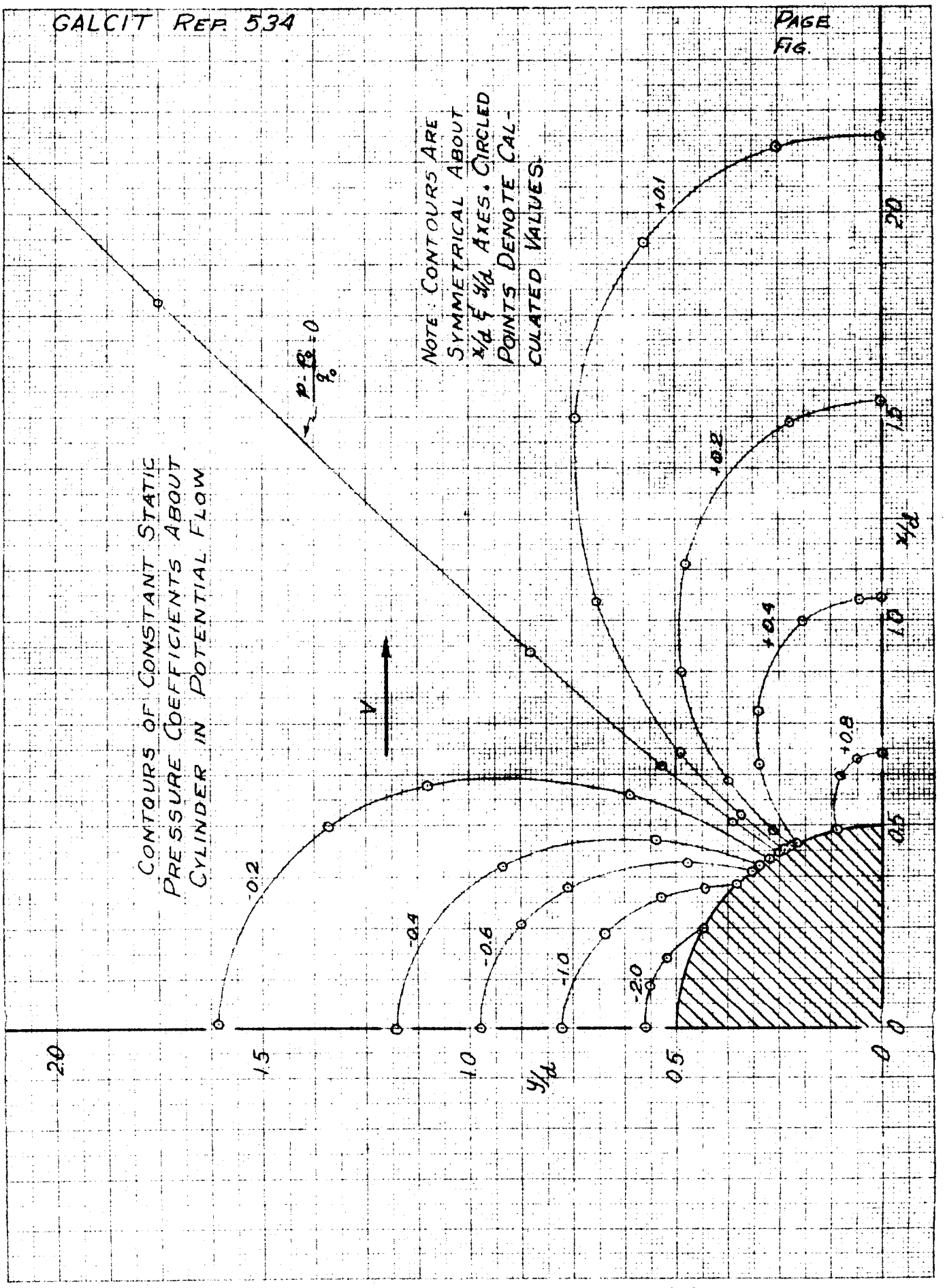

Fig. IV-55 Contours of Constant Static Pressure Coefficients About Cylinder in Potential Flow

CONTOURS OF CONSTANT STATIC PRESSURE
COEFFICIENTS ABOUT CYLINDER AT NORTH ENDPLATE

○ { C_1, RUNS 49A,B ; C_1+X_1, RUN 53 } $q_\infty = 80\ LB/FT^2$

⊡ C_2, $q_\infty = 24\ LB/FT^2$, RUN 65

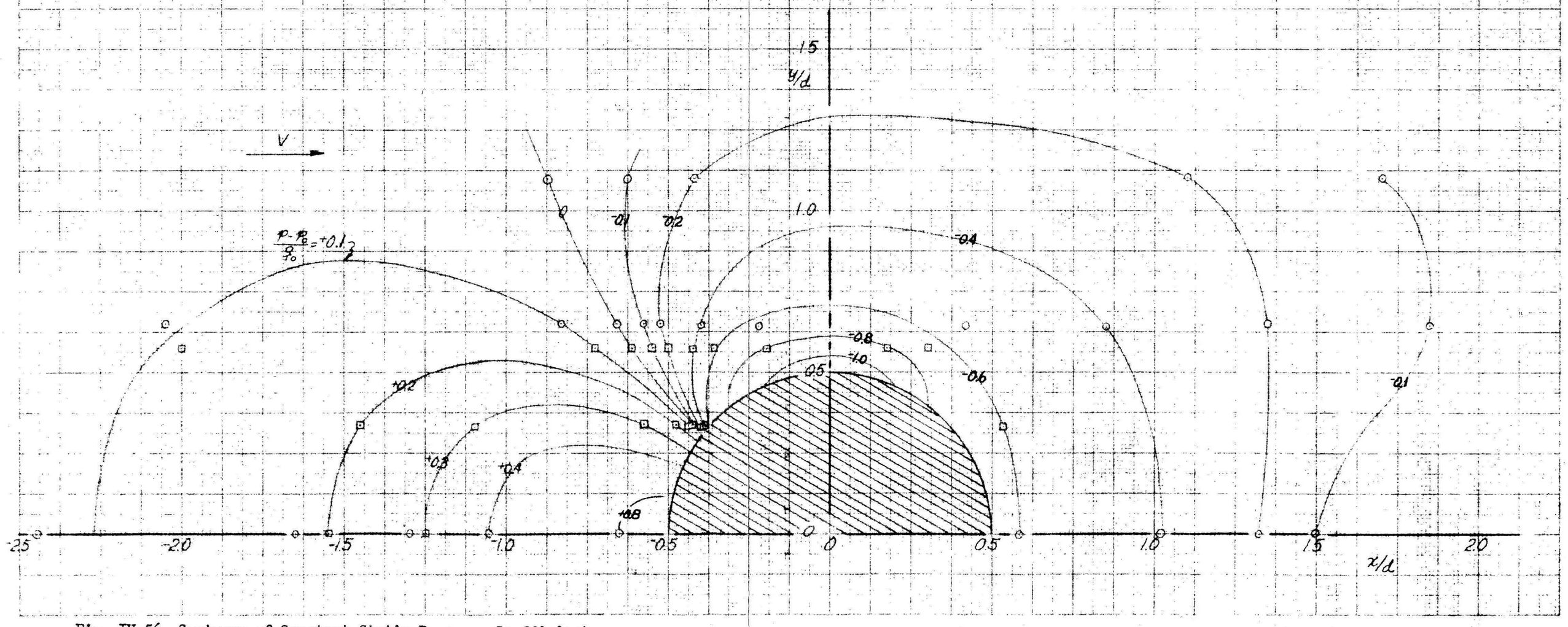

Fig. IV-56 Contours of Constant Static Pressure Coefficients About Cylinders C_1 and C_2 at North Endplate

CONTOURS OF CONSTANT STATIC PRESSURE
COEFFICIENTS ABOUT CYLINDER AT NORTH ENDPLATE
⊙ $C_1 + T_{10}$, RUN 52
$q_0 = 80 LB/FT^2$

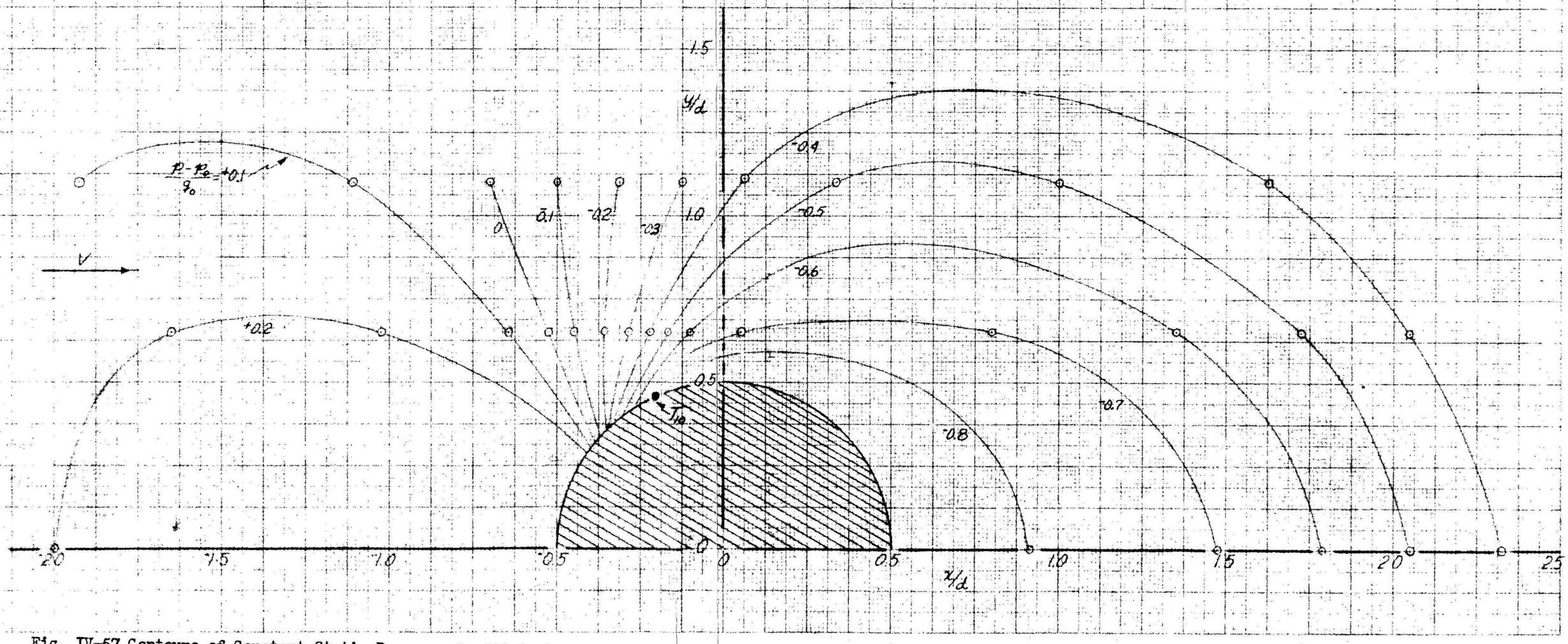

Fig. IV-57 Contours of Constant Static Pressure Coefficients About Cylinder C_1 with Separation Strips T_{10} at North Endplate

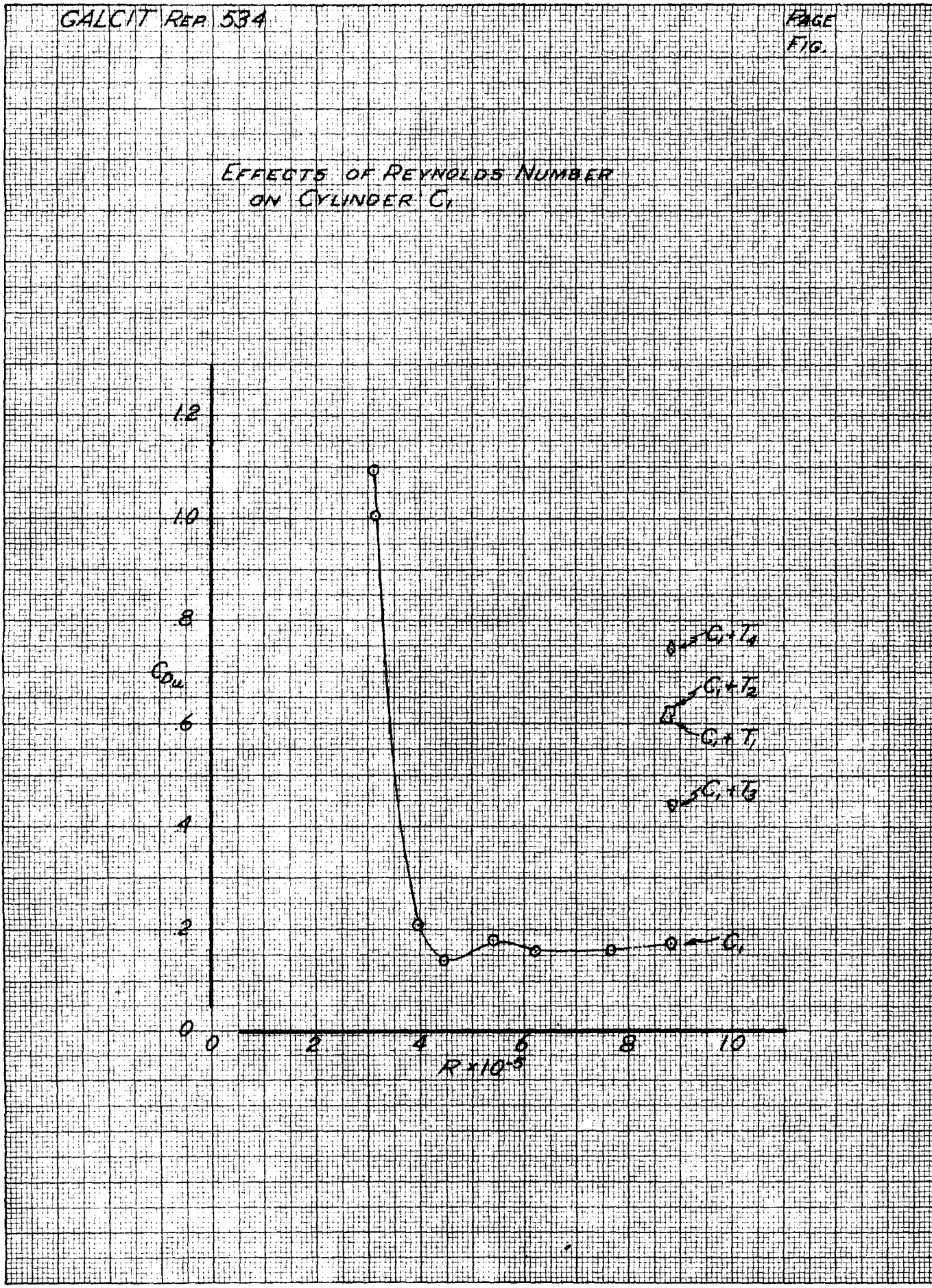

Fig. IV-58 Effects of Reynolds Number Upon Drag Coefficient for Cylinder C_1

GALCIT REP 538

PAGE
FIG

$\frac{q}{\gamma_0} = 80 \text{ LB/FT}^2$

○ C_1' , RUN 74
△ C_1 , RUNS 6, 13, 56, 57
□ $C_1 + T_3$, " 18, 19, 63
◇ $C_1 + T_4$, " 24, 61

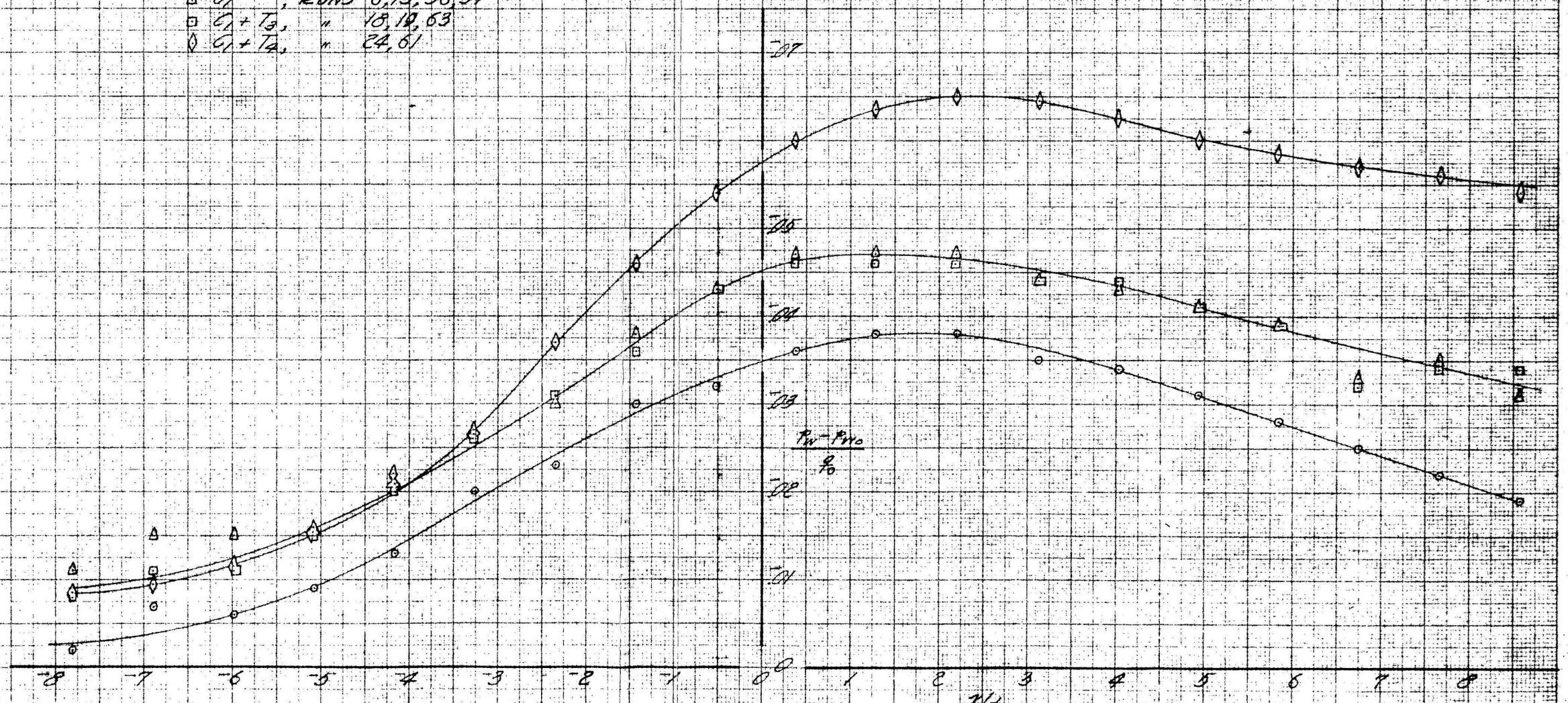

Fig. IV-59 Static Pressure Survey Along Floor and Ceiling, Cylinder C_1 with and without Separation Strips

GALCIT REP 534

PAGE
FIG

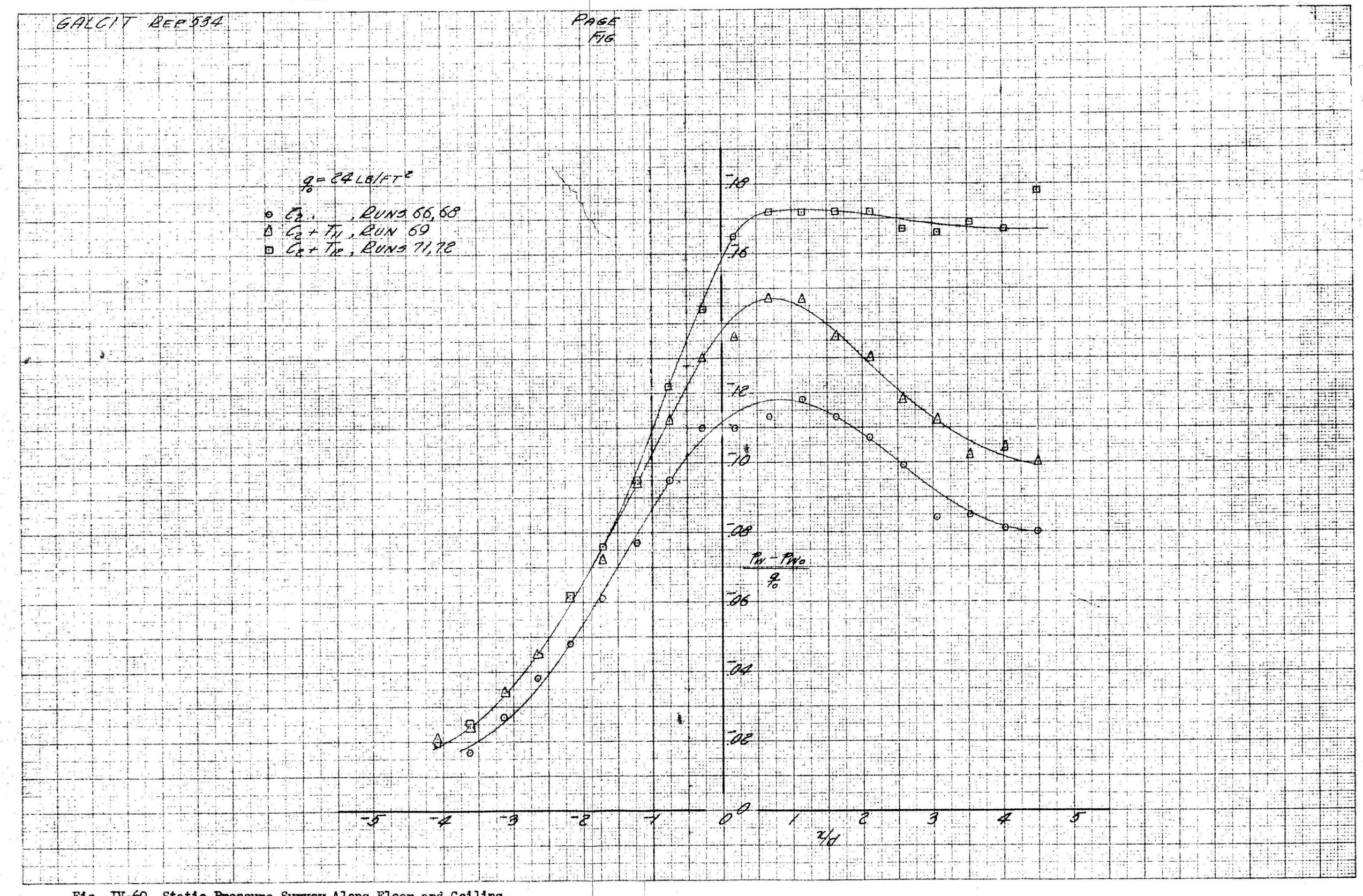

Fig. IV-60 Static Pressure Survey Along Floor and Ceiling, Cylinder C_2 with and without Separation Strips

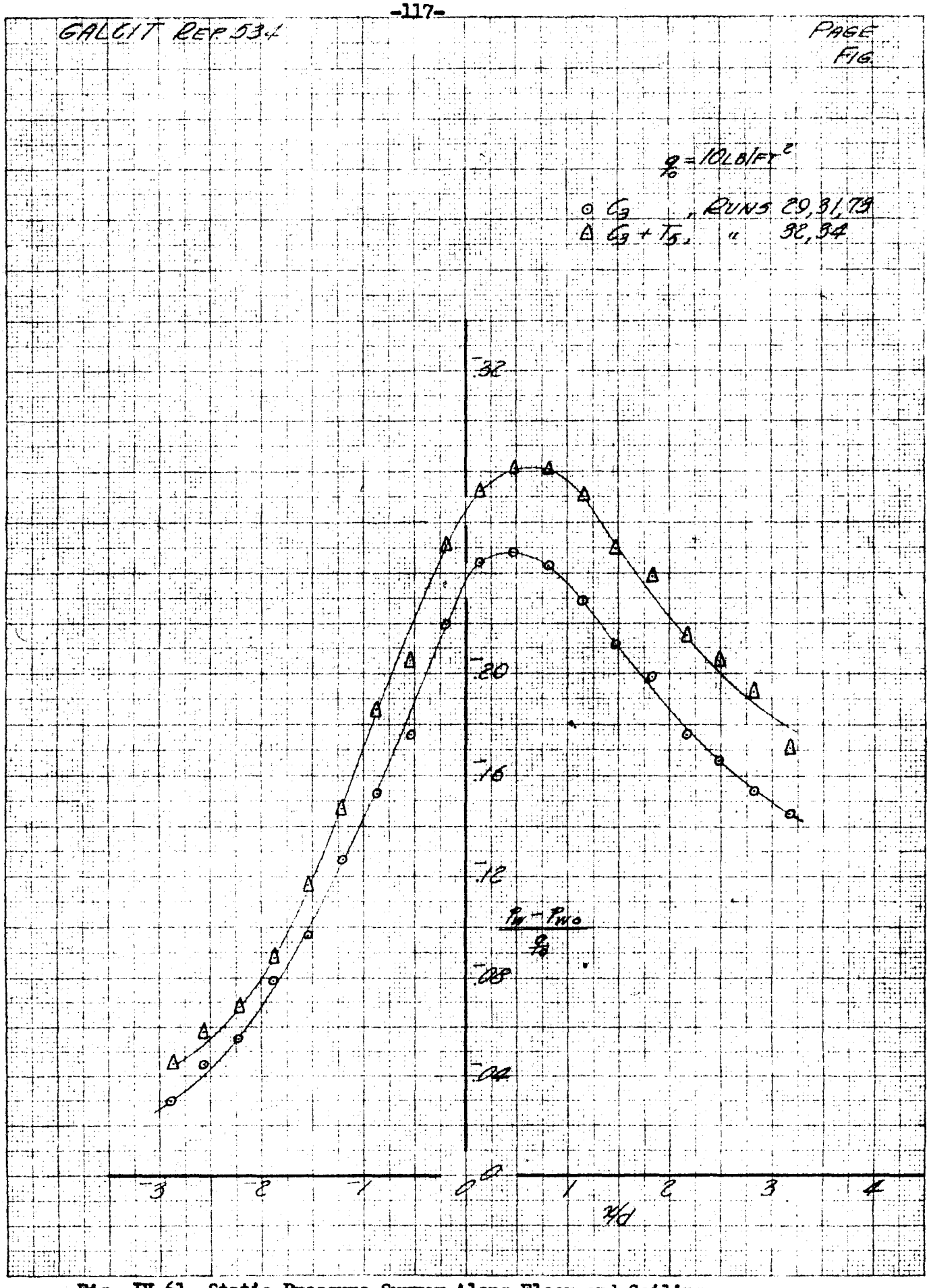

Fig. IV-61 Static Pressure Survey Along Floor and Ceiling, Cylinder C_3 with and without Separation Strips

GALCIT REP 534 PAGE FIG.

WALL VELOCITIES RESULTING FROM SOLID AND WAKE BLOCKAGE FOR CYLINDER C_2 WITH SEPARATION STRIPS T_{11}

$(\frac{u}{U})_w - 1$ = EXPERIMENTALLY DETERMINED VELOCITY CHANGE AT WALL

ε_{sw} = THEORETICAL VALUE OF VELOCITY AT WALL FROM SOLID BLOCKAGE

$(\varepsilon_{ww})_1$ = PSEUDO-EXPERIMENTAL VALUE OF VELOCITY AT WALL FROM WAKE BLOCKAGE

$= [(\frac{u}{U})_w - 1] - \varepsilon_{sw}$

$(\varepsilon_{ww})_2$ = THEORETICAL VALUE OF VELOCITY AT WALL FROM WAKE BLOCKAGE EMPLOYING A SYSTEM OF FOUR SOURCES AND SINKS ON TUNNEL AXIS AFT OF CYLINDER TO SIMULATE THE WAKE. STRENGTHS OF SOURCES AND SINKS ARE DETERMINED FROM VALUES OF $(\varepsilon_{ww})_1$ AT FOUR x/d LOCATIONS.

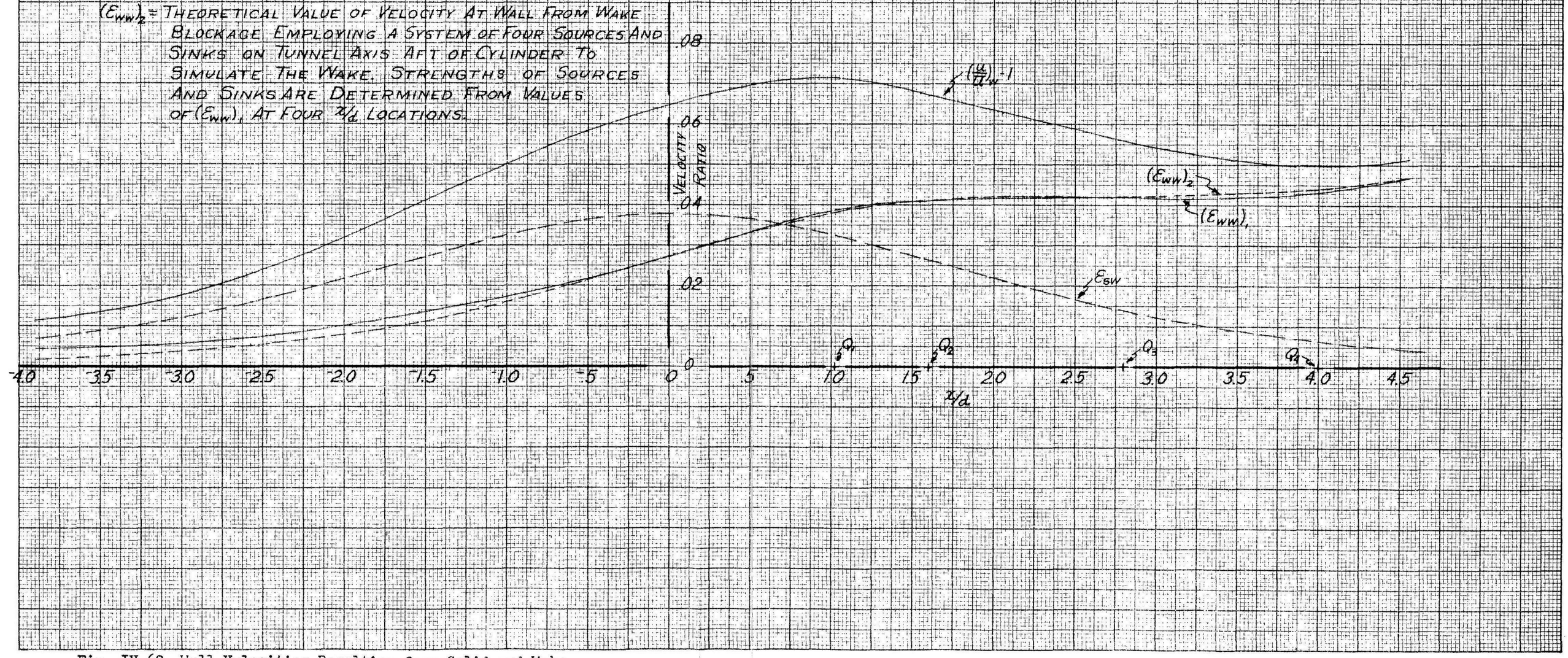

Fig. IV-62 Wall Velocities Resulting from Solid and Wake Blockage Effects, Cylinder C_2 with Separation Strips T_{11}

GALCIT REP. 534

PAGE
FIG.

WALL VELOCITIES RESULTING FROM SOLID AND WAKE BLOCKAGE FOR CYLINDER C_2 WITH SEPARATION STRIPS T_{12}

$(\frac{u}{U})_w - 1$ = EXPERIMENTALLY DETERMINED VELOCITY CHANGE AT WALL

ε_{sw} = THEORETICAL VALUE OF VELOCITY AT WALL FROM SOLID BLOCKAGE

$(\varepsilon_{ww})_1$ = PSEUDO-EXPERIMENTAL VALUE OF VELOCITY AT WALL FROM WAKE BLOCKAGE
$= [(\frac{u}{U})_w - 1] + \varepsilon_{sw}$

$(\varepsilon_{ww})_2$ = THEORETICAL VALUE OF VELOCITY AT WALL FROM WAKE BLOCKAGE EMPLOYING A SYSTEM OF FOUR SOURCES AND SINKS ON TUNNEL AXIS AFT OF CYLINDER TO SIMULATE THE WAKE. STRENGTHS OF SOURCES AND SINKS ARE DETERMINED FROM VALUES OF (ε_{ww}) AT FOUR x/d LOCATIONS

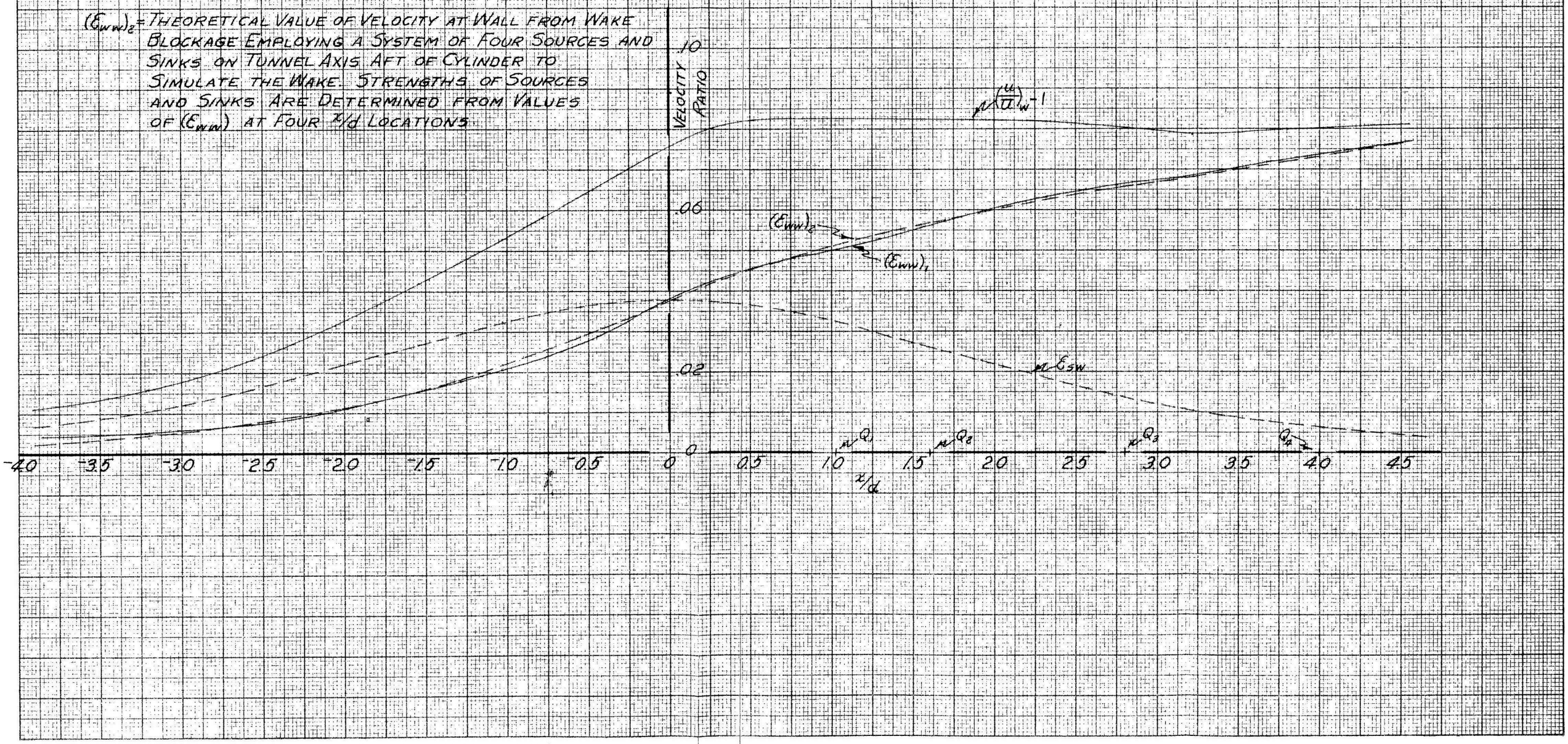

Fig. IV-63 Wall Velocities Resulting from Solid and Wake Blockage Effects, Cylinder C_2 with Separation Strips T_{12}

Appendix A

THEORETICAL APPROACH TO FLOW ABOUT CIRCULAR CYLINDERS

The representation of real flow (two-dimensional, viscous) about circular cylinders can be approximated by special treatments of perfect fluid theory assuming two-dimensional, incompressible, non-viscous, and irrotational flow. With these assumptions, we may use the general potential flow theory and employ the analytic function and complex variable.[1]

The study will be subdivided into the following groups:

1. Perfect fluid flow about a circular cylinder in an infinite two-dimensional channel.
2. Perfect fluid flow in an infinite two-dimensional channel about a circular cylinder using singularities downstream to simulate the wake encountered in real flow.
3. Perfect fluid flow about a circular cylinder in a finite two-dimensional channel.
4. Perfect fluid flow in a finite two-dimensional channel about a circular cylinder using singularities downstream to simulate the wake.
5. Comparisons between the flows in an infinite and a finite two-dimensional channel.

In the following treatments we will work with the quantities:

$z = x + iy = re^{i\theta}$ = complex distance

$w(z) = u - iv = (u_r - iu_\theta)e^{-i\theta}$ = complex velocity

$F(z) = \phi + i\psi$ = complex potential

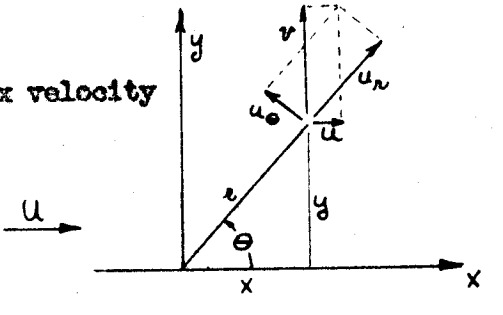

From the condition of irrotationality, the velocity potential is defined as:

$$u = \frac{\partial \varphi}{\partial x} \quad ; \quad v = \frac{\partial \varphi}{\partial y}$$

The continuity condition defines the stream function ψ as:

$$u = \frac{\partial \psi}{\partial y} \quad ; \quad v = -\frac{\partial \psi}{\partial x}$$

Having defined the basic quantities which we will use in the derivations, we can proceed to consider the cases outlined.

1. TWO-DIMENSIONAL FLOW ABOUT A CIRCULAR CYLINDER IN AN INFINITE CHANNEL

This flow is well known,[6] therefore it will only be given in summary here. Potential flow theory tells us that two-dimensional flow about a circle has as its hydrodynamic equivalent the superposition of rectilinear flow upon doublet flow. In this case the $\psi = 0$ streamline defines both the stagnation streamlines and the circle whose center is coincident with the doublet and whose radius is determined by the doublet strength.

The complex potential is:

$$F(z) = U\left(z + \frac{b^2}{z}\right) \ldots (1.1)$$

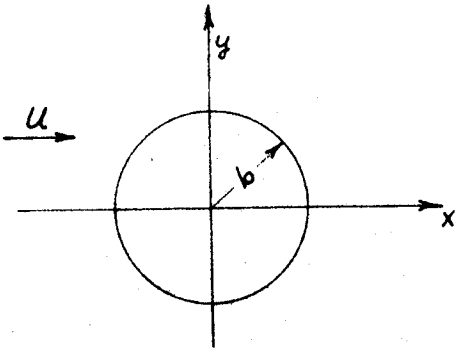

from which the flow potential and stream function are immediately

seen as being

$$\left.\begin{aligned} \varphi &= Ux\left[1+\frac{b^2}{(x^2+y^2)}\right] \\ \psi &= Uy\left[1-\frac{b^2}{(x^2+y^2)}\right] \end{aligned}\right\} \quad \ldots (1.2)$$

Equation 1.2 shows that the $\psi = 0$ streamline is indeed defined by the $y = 0$ axis and by a circle of radius b.

Also the complex velocity is defined by:

$$\left.\begin{aligned} w(z) &= U\left[1-\left(\frac{b}{z}\right)^2\right] \\ &= U\left[1-\left(\frac{b}{r}\right)^2 e^{-2i\theta}\right] \end{aligned}\right\} \quad \ldots (1.3)$$

The velocities may be readily obtained in either cartesian or polar coordinates using equation 1.2 or 1.3, and they are:

$$\left.\begin{aligned} u &= U\left[1-\frac{b^2(x^2-y^2)}{(x^2+y^2)}\right] \\ v &= -U\frac{b^2xy}{(x^2+y^2)} \end{aligned}\right\} \quad \ldots (1.4a)$$

$$\left.\begin{aligned} u_r &= U\left[1-\left(\frac{b}{r}\right)^2\right]\cos\theta \\ u_\theta &= -U\left[1+\left(\frac{b}{r}\right)^2\right]\sin\theta \end{aligned}\right\} \quad \ldots (1.4b)$$

The pressure coefficient in the flow may be obtained by presenting the pressure, which is obtained from the incompressible form of the

energy equation, in dimensionless form. The actual equation is:

$$C_p = \frac{p - p_\infty}{\frac{1}{2}\rho U^2} = 1 - \frac{u^2+v^2}{U^2}$$

$$= \left(\frac{b}{r}\right)^2\left[2 - \left(\frac{b}{r}\right)^2 - 4\sin^2\theta\right] \qquad \ldots (1.5)$$

On the cylinder, the pressure coefficient varies between

$$C_p = +1.0 \text{ at } \theta = 0^\circ$$

and

$$C_p = -3.0 \text{ at } \theta = \pi/2$$

2. TWO-DIMENSIONAL FLOW ABOUT A CIRCULAR CYLINDER IN AN INFINITE CHANNEL WITH SINGULARITIES DOWNSTREAM

In representing the real flow in an infinite channel about a circular cylinder, account must be taken of the viscosity effects which cause a wake to form at the cylinder and go downstream. In representing the modifications to the flow in the vicinity of the cylinder from the wake, we shall consider the flow change as being caused by a wake width which is defined by a displacement thickness in a manner similar to that used in boundary layer theory. The wake displacement thickness defines a solid body behind the cylinder which may be duplicated from potential flow theory by distributing singularities along the horizontal axis. In the solution presented here, only one singularity behind the cylinder will be considered, namely, a source. In actual practice, a series of sources and sinks are needed in order to match accurately the desired wake displacement thickness, but superposition of the general solution presented here

permits this to be done readily.

Since the original boundary conditions are that uniform flow go around a circular body, and these conditions must still exist when a solid body wake representation is used, some singularities must lie within the circle in order to preserve it as an undistorted solid body. To accomplish this, an image of the source behind the cylinder must be placed inside the cylinder at the "inverse point" plus a sink at the origin (so as to have no fluid outflow from the circle). The actual location and strength of the source behind the cylinder is determined by the shape and width of the wake displacement thickness.

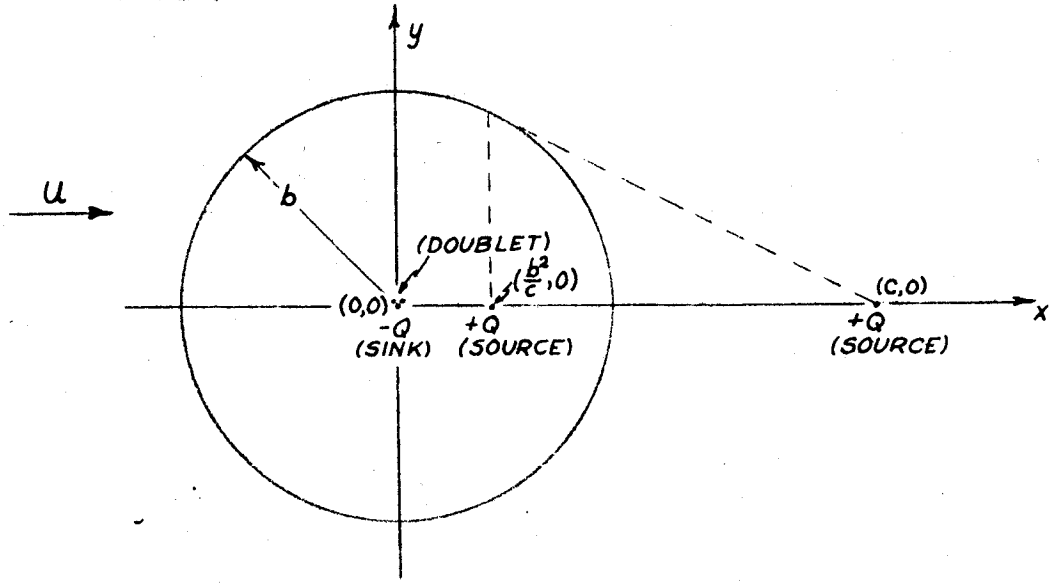

As shown in the above sketch we have:

a) Rectilinear velocity coming from infinity with magnitude U.

b) Doublet at origin of strength Ub^2. This strength defines the radius of the cylinder in rectilinear flow.

c) Source +Q placed arbitrarily on the x axis at x = c.

d) Source +Q placed at the "inverse point" inside the cylinder on the x axis at $x = b^2/c$.

e) Sink -Q placed at the origin.

We can therefore write the complex potential as :

$$F = \varphi + i\psi = U\left[z + \frac{b^2}{z}\right] + \frac{Q}{2\pi}\left[\ln(z-c) + \ln\left(z - \frac{b^2}{c}\right) - \ln z\right] \qquad \ldots(2.1)$$

where $z = x + iy$

$$z - c = (x-c) + iy$$

$$z - \frac{b^2}{c} = \left(x - \frac{b^2}{c}\right) + iy$$

Equation 2.1 can be separated into its real and imaginary parts which in turn gives the velocity potential and the stream function. These are:

$$\left.\begin{aligned} \varphi &= Ux\left[1 + \frac{b^2}{x^2+y^2}\right] + \frac{Q}{2\pi}\ln\frac{\sqrt{\alpha^2+\beta^2}}{x^2+y^2} \\ \psi &= Uy\left[1 - \frac{b^2}{x^2+y^2}\right] + \frac{Q}{2\pi}\tan^{-1}\frac{\beta}{\alpha} \end{aligned}\right\} \qquad \ldots(2.2)$$

where

$$\left.\begin{aligned} \alpha &= x(x^2+y^2+b^2) - (x^2+y^2)\left(\frac{c^2+b^2}{c}\right) \\ \beta &= y(x^2+y^2-b^2) \end{aligned}\right\} \qquad \ldots(2.2a)$$

The boundary conditions are satisfied by equations 2.2 and 2.2a, and this can be most readily seen if the complete expression for ψ

is presented.

$$\psi = Uy\left[1 - \frac{b^2}{x^2+y^2}\right] + \frac{Q}{2\pi}\tan^{-1}\frac{y(x^2+y^2-b^2)}{x(x^2+y^2+b^2)-(x^2+y^2)(\frac{c^2+b^2}{c})} \quad \ldots(2.2b)$$

Equation 2.2b shows us that $\psi = 0$ when $y = 0$ and $x > c$, that $\psi = Q/2$ on the circle of radius b and when $y = 0$ and $x < 0$ or $b^2/c < x < c$, and that $\psi = Q$ when $y = 0$ and $0 < x < b^2/c$.

Also a solid body symmetrical about the x axis and downstream of the cylinder is formed by the $\psi = Q/2$ streamline. This solid body behind the cylinder will actually intersect the cylinder if the source is located near to the cylinder and is of sufficient strength. This is easily shown from the radial and tangential velocities on the cylinder.

When $r = b$:

$$\left.\begin{aligned} u_r &= \frac{1}{r}\frac{\partial\psi}{\partial\theta} = 0 \\ u_\theta &= -\frac{\partial\psi}{\partial r} = -2U\sin\theta\left[1 - \frac{Q}{2\pi U}\frac{c}{c^2+b^2-2bc\cos\theta}\right] \end{aligned}\right\} \quad \ldots(2.3)$$

but $(c^2 + b^2 - 2bc\cos\theta)^{1/2} = S$ = distance from source $+Q$ at $x = c$, $y = 0$ to point on cylinder surface defined by angle θ.

Therefore, the tangential velocity u_θ is zero when $\theta = 0$, as in the case for perfect fluid flow around a cylinder. In addition, u_θ is zero when the term within the bracket is zero, or in other words when:

$$Q \cdot c = 2\pi U S^2 \quad \ldots(2.4)$$

Equation 2.4 gives the result also that the solid body will not intersect the cylinder unless $Q \geqslant 2\pi U \left(1-\frac{b}{c}\right)^2$.

The width of the solid body behind the cylinder steadily increases as x becomes larger and has an asymptotic value as x tends to infinity. This final value of the wake width (or the width of the $\frac{Q}{2}$ streamline) may be found by considering equation 2.2b as follows:

when $x \to \infty$, equation 2.2b tells us that

$$\psi = \frac{Q}{2} = Uy + \frac{Q}{2\pi} \tan^{-1} O\left(\frac{1}{+x}\right)$$

$$= Uy + 0$$

so in a limit the half width of the wake becomes

$$\lim_{x \to \infty} y = \frac{Q}{2U} \qquad \ldots(2.5)$$

or the total width becomes $\frac{Q}{U}$. This is to be expected since the volume outflow from the source behind the cylinder must eventually diffuse into the freestream.

3. TWO-DIMENSIONAL FLOW ABOUT A CIRCULAR CYLINDER IN A FINITE CHANNEL

The solution for perfect fluid flow about a circular cylinder in a finite channel, although not quite as well known as that of flow in an infinite channel about a circular cylinder, is treated in many references.[7] The treatment for this case of a finite channel is similar to that for an infinite channel in that a doublet is placed at the origin while in the presence of a uniform rectilinear flow field. The modification arises in that the walls of the finite channel impose a boundary condition that the flow is tangential at the walls. This additional boundary condition is met by placing images of the original doublet along the y axis uniformly spaced such that the distance between them is equivalent to the total channel width (providing of course that the original doublet is midway between the channel walls).

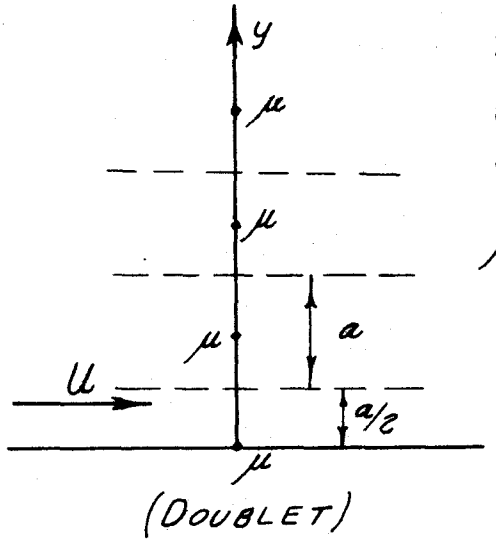

Define the following quantities

a = height of channel

b = radius of cylinder

μ = strength of doublet

$= \frac{2\pi^2 b^2}{Ua}$

Looking at the sketch showing the arrangement of the singularties, we can set up the complex flow potential.

$$F(z) = Uz + \frac{\mu}{2\pi} \sum_{n=-\infty}^{+\infty} \frac{1}{z - ina}$$

and the infinite series can be expressed as $\coth \frac{\pi z}{a}$, so

$$F(z) = Uz + \frac{\mu}{2\pi} \coth \frac{\pi z}{a} \qquad \ldots(3.1)$$

The doublets are located at (0,0), (0, ± a), (0, ± 2a),..etc. Substituting z = x +iy and separating F (z) into its real and imaginary parts will give the stream function and flow potential. Also replacing the doublet μ by $2\pi b^2 U/a$, as we shall show later, results in a close approximation to having the cylinder circular.

The hyperbolic cotangent of a complex variable can be expressed as:

$$\coth z = \frac{\cosh (x' + iy')}{\sinh (x' + iy')}$$

$$= \frac{\cosh x' \cos y' + i \sinh x' \sin y'}{\sinh x' \cos y' + i \cosh x' \sin y'}$$

which can be simplified to

$$\coth z = \frac{\sinh 2x' - i \sin 2y'}{\cosh 2x' - \cos 2y'} \qquad \ldots(3.2)$$

Now if we replace z' by $\pi z/a$ and let $\mu = 2\pi^2 b^2 U/a$, we get

$$\left.\begin{aligned} \phi &= Ux + \frac{\pi b^2 U}{a} \frac{\sinh \frac{2\pi x}{a}}{\cosh \frac{2\pi x}{a} - \cos \frac{2\pi y}{a}} \\ \psi &= Uy - \frac{\pi b^2 U}{a} \frac{\sin \frac{2\pi y}{a}}{\cosh \frac{2\pi x}{a} - \cos \frac{2\pi y}{a}} \end{aligned}\right\} \qquad \ldots(3.3)$$

Equation 3.3 satisfied the boundary condition that $\psi = 0$ when $y = 0$. Also the upper and lower walls of the channel become the streamlines $\psi = Ua/2$ and $\psi = -Ua/2$ respectively. In order to investigate whether the circle of radius b is a true streamline, we shall use equation 3.3 in a slightly modified form.

When $\psi = 0$;

$$y\left(\cosh\frac{2\pi x}{a} - \cos\frac{2\pi y}{a}\right) = \frac{\pi b^2}{a}\sin\frac{2\pi y}{a}$$

$$= \frac{\pi b^2}{a}\left[\frac{2\pi y}{a} - \left(\frac{2\pi y}{a}\right)^3 \cdot \frac{1}{3!} + \cdots\right] \quad \ldots(3.4)$$

This equation is satisfied by $y = 0$. If we factor y out, the streamline $\psi = 0$ is also satisfied by

$$\cosh\frac{2\pi x}{a} - \cos\frac{2\pi y}{a} = \frac{2\pi^2 b}{a} - \frac{\pi b^2}{a}\left(\frac{2\pi}{a}\right)^3 \cdot \frac{y^2}{3!} + \cdots \quad \ldots(3.5)$$

Equation 3.5 is the equation of an oval with the origin as center. Its semi-diameter along the x- axis is obtained by setting $y = 0$.

$$\cosh\frac{2\pi x}{a} - 1 = \frac{2\pi^2 b}{a}$$

or

$$x = \frac{a}{2\pi}\cosh^{-1}\left(1 + \frac{2\pi^2 b}{a}\right) \quad \ldots(3.6a)$$

The semi-diameter along the y axis is obtained by setting $x = 0$ in equation 3.4.

$$1 - \cos\frac{2\pi y}{a} = \frac{\pi b^2}{a} \cdot \frac{1}{y} \cdot \sin\frac{2\pi y}{a}$$

which can be simplified to give

$$\sin\frac{2\pi y}{a} = \frac{1}{\frac{ay}{2\pi b^2} + \frac{\pi b^2}{2ay}} \qquad \ldots(3.6b)$$

The actual departure of the oval as defined by equation 3.5 from a circle of radius b is small. In a later section, we shall determine the error involved in using these expressions with the various ratios of $\frac{b}{a}$ considered in the experiments.

The velocities may be readily determined from the equations for the flow potential and the stream function.

$$u = \frac{\partial\Phi}{\partial x} = \frac{\partial\psi}{\partial y} \quad ; \quad v = \frac{\partial\Phi}{\partial y} = -\frac{\partial\psi}{\partial x}$$

differentiating ψ in equation 3.3 with respect to the variable y gives us

$$u = U - \frac{2\pi^2 b^2}{a^2} U\left[\frac{\cosh\frac{2\pi x}{a}\cos\frac{2\pi y}{a} - 1}{\left(\cosh\frac{2\pi x}{a} - \cos\frac{2\pi y}{a}\right)^2}\right] \qquad \ldots(3.7)$$

and differentiating in equation 3.3 with respect to the variable y gives us

$$v = -\frac{2\pi^2 b^2}{a^2} U\left[\frac{\sinh\frac{2\pi x}{a}\sin\frac{2\pi y}{a}}{\left(\cosh\frac{2\pi x}{a} - \cos\frac{2\pi y}{a}\right)^2}\right] \qquad \ldots(3.7a)$$

At the wall where y = a/2, we find from equation 3.7 that

$$u = U\left[1 + \frac{2\pi^2 b^2}{a^2}\frac{1}{\cosh\frac{2\pi x}{a} + 1}\right] = U(1 + \varepsilon_{sw}) \qquad \ldots(3.8)$$

where ε_{sw} = Solid blockage correction to the freestream velocity at the wall.

4. TWO-DIMENSIONAL FLOW ABOUT A CIRCULAR CYLINDER IN A FINITE CHANNEL WITH SINGULARITIES DOWNSTREAM

In representing the real flow in a finite channel about a circular cylinder, account will be taken of the wake behind the cylinder in a manner similar to that used in section 2. As pointed out in section 3, the effects of the channel walls are to cause images of the flow singularities to be formed in a uniform pattern to $\pm$ infinity in the y direction when the walls are parallel to and equidistant from the x axis. These images form in order to preserve the channel walls as streamlines.

It is convenient to first consider the nature of the complex potential for a source singularity at the origin and to then set up the complete complex potential for the desired flow pattern.

For a single source at the origin, the complex potential is:

$$F(z) = \frac{Q}{2\pi} \ln z$$

For a series of sources in the y direction at (0,0), (0, $\pm$ a), (0, $\pm$ 2a), ... etc., which corresponds to the image representation of a source between two walls at y = $\pm$ a/2, we have as the complex potential:

$$F(z) = \frac{Q}{2\pi} \sum_{n=-\infty}^{+\infty} \ln (z - ina)$$

and the infinite series can be expressed as $\ln \sinh \frac{\pi z}{a}$, so

$$F(z) = \frac{Q}{2\pi} \ln \sinh \frac{\pi z}{a} \qquad \ldots(4.1)$$

Equation (4.1) can be separated into its real and imaginary

parts in order to give the flow potential and the stream function.

Equation (4.1) becomes, using complex notation:

$$F(z) = \frac{Q}{2\pi} \ln \sinh \frac{\pi(x+iy)}{a}$$

$$= \frac{Q}{2\pi} \ln \left(\sinh \frac{\pi x}{a} \cos \frac{\pi y}{a} + i \cosh \frac{\pi x}{a} \sin \frac{\pi y}{a} \right)$$

$$= \frac{Q}{4\pi} \ln \frac{1}{2} \left(\cosh \frac{2\pi x}{a} - \cos \frac{2\pi y}{a} \right) + \frac{iQ}{2\pi} \tan^{-1} \frac{\tan \frac{\pi y}{a}}{\tanh \frac{\pi x}{a}}$$

$$= \phi + i\psi$$

Therefore we can express the flow potential and the stream function for a single source midway between two channel walls as:

$$\left.\begin{aligned} \phi &= \frac{Q}{4\pi} \ln \frac{1}{2} \left(\cosh \frac{2\pi x}{a} - \cos \frac{2\pi y}{a} \right) \\ \psi &= \frac{Q}{2\pi} \tan^{-1} \frac{\tan \frac{\pi y}{a}}{\tanh \frac{\pi x}{a}} \end{aligned}\right\} \qquad \ldots(4.2)$$

The velocity components due to the single source are:

$$\left.\begin{aligned} u &= \frac{\partial \phi}{\partial x} = \frac{Q}{2a} \frac{\sinh \frac{2\pi x}{a}}{\cosh \frac{2\pi x}{a} - \cos \frac{2\pi y}{a}} \\ v &= \frac{\partial \phi}{\partial y} = \frac{Q}{2a} \frac{\sin \frac{2\pi y}{a}}{\cosh \frac{2\pi x}{a} - \cos \frac{2\pi y}{a}} \end{aligned}\right\} \qquad \ldots(4.3)$$

Having developed the equations for a singularity at the origin, we can set up a complex potential for the system in which the wake behind the cylinder is represented by a source singularity. As in section 2, we shall consider the effects of a source behind the cylinder. In addition, we have a sink of the same strength far downstream so as to satisfy the boundary condition that the wake has no influence far upstream.

Using the results of equations 3.1 and 4.1, we get as a complex potential

$$f(z) = Uz + \frac{\pi b^2 U}{a}\coth\frac{\pi z}{a} + \frac{Q}{2\pi}\left\{\ln\sinh\frac{\pi}{a}(z-c) + \ln\sinh\frac{\pi}{a}\left(z-\frac{b^2}{c}\right) - \ln\sinh\frac{\pi z}{a} - \ln\sinh\frac{\pi(z-B)}{a}\right\} \quad \ldots(4.4)$$

where account is taken of

a) Rectilinear flow from minus infinity with magnitude U

b) Doublet at origin and its images

c) Source +Q at x = c, y = 0 and its images

d) Source +Q at inverse point x = b^2/c, y = 0 and its images

e) Sink −Q at origin and its images

f) Sink − Q far downstream at x = B, y = 0 and its images.

Separating the complex potential into its imaginary part and letting B approach its limit, we get the stream function.

$$\psi = Uy - \frac{\pi b^2 U}{a}\frac{\sin\frac{2\pi y}{a}}{\cosh\frac{2\pi x}{a} - \cos\frac{2\pi y}{a}} + \frac{Q}{2\pi}\left\{\tan^{-1}\frac{\tan\frac{\pi y}{a}}{\tanh\frac{\pi}{a}(x-c)} + \tan^{-1}\frac{\tan\frac{\pi y}{a}}{\tanh\frac{\pi}{a}\left(x-\frac{b^2}{c}\right)} - \tan^{-1}\frac{\tan\frac{\pi y}{a}}{\tanh\frac{\pi x}{a}} + \frac{\pi y}{a}\right\} \quad \ldots(4.5)$$

From equation 4.5, we see that the streamlines have the same values along the x axis and over the slightly distorted circle as in the infinite channel case. In addition the upper and lower walls of the channel correspond to $\psi = \pm\left[\frac{Ua}{2} + \frac{Q}{2}\right]$ respectively.

The velocity in the channel is given by:

$$u = U + \frac{2\pi^2 b^2 U}{a} \frac{\sin \frac{2\pi y}{a}}{\cosh \frac{2\pi x}{a} - \cos \frac{2\pi y}{a}} + \frac{Q}{2a} \left\{ \frac{\sinh \frac{2\pi}{a}(x-c)}{\left[\cosh \frac{2\pi}{a}(x-c) - \cos \frac{2\pi y}{a}\right]} \right.$$

$$\left. + \frac{\sinh \frac{2\pi}{a}\left(x-\frac{b^2}{c}\right)}{\left[\cosh \frac{2\pi}{a}\left(x-\frac{b^2}{c}\right) - \cos \frac{2\pi y}{a}\right]} - \frac{\sinh \frac{2\pi x}{a}}{\left[\cosh \frac{2\pi x}{a} - \cos \frac{2\pi y}{a}\right]} + 1 \right\} \quad \ldots(4.6)$$

If we define the velocity along the channel walls by

$$u_w = U\left[1 + \varepsilon_{sw} + \varepsilon_{ww}\right] \quad \ldots(4.7)$$

where

ε_{sw} = Solid blockage correction to velocity at the wall

ε_{ww} = Wake blockage correction to velocity at the wall

Then from equation 4.6, we see that:

$$\varepsilon_{sw} = 2\pi^2 \frac{b^2}{a^2} \cdot \frac{1}{\cosh \frac{2\pi x}{a} + 1}$$

$$\varepsilon_{ww} = \frac{Q}{2Ua} \left\{ \frac{\sinh \frac{2\pi}{a}(x-c)}{\left[\cosh \frac{2\pi}{a}(x-c) + 1\right]} + \frac{\sinh \frac{2\pi}{a}\left(x-\frac{b^2}{c}\right)}{\left[\cosh \frac{2\pi}{a}\left(\frac{x-b^2}{c}\right) + 1\right]} \right.$$

$$\left. - \frac{\sinh \frac{2\pi x}{a}}{\left[\cosh \frac{2\pi x}{a} + 1\right]} + 1 \right\} \quad \ldots(4.8)$$

The change in static pressure at the wall in terms of the solid and wake blockage corrections is obtained using the incompressible form of the energy equation. The expression is:

$$\frac{p_w - p_{wo}}{q_o} = 1 - \frac{q_w}{q_o} = 1 - \left(1 + \varepsilon_{sw} + \varepsilon_{ww}\right)^2 \quad \ldots(4.9)$$

where

p_{wo} = static pressure at wall originally

p_w = static pressure at wall with blockage

q_o = apparent dynamic pressure or dynamic pressure in channel when no cylinder is present.

q_w = true dynamic pressure at wall when cylinder is present

The linearized form of equation 4.9 is obtained by assuming ε_{sw} and $\varepsilon_{ww} \ll 1$. Then we get:

$$\frac{p_w - p_{wo}}{q_o} = -2(\varepsilon_{sw} + \varepsilon_{ww}) \qquad \ldots(4.9a)$$

5. COMPARISON OF FLOWS IN AN INFINITE AND A FINITE WIDTH CHANNEL

Compared in this section are the potential theory solutions of the flow about a circular cylinder with a wake representation in an infinite and finite width channel. The example considered in the comparison applies to the case of a source located 0.50 radii behind the cylinder trailing edge. The source strength was selected such that an exaggerated solid body representation of the wake would be obtained in order to permit a ready visualization of the flow. The source strength is $Q = 2Ub$ and this strength results in the stagnation streamlines (ψ/Ub) having a value of unity.

Figure A-1 presents the streamlines about a cylinder and its wake while in a two-dimensional flow channel of infinite width. Equation 2.2b was employed to determine the locations of the streamlines.

For the case of flow in a finite width channel, the ratio of channel width to cylinder diameter was selected to correspond to the medium-sized cylinder (C_2) when tested in the two-dimensional test section during the experimental investigations. Equation 4.5 was employed to determine the streamlines. The calculations showed that the distortion of the circular cylinder from the images of the doublet resulted in approximately a 1.2% decrease in maximum thickness. The effects of the images of the source (wake) system resulted in an additional distortion of the maximum thickness of the cylinder, and as shown later the departure of the cylinder from a circle is quite pronounced over the aft end. The cylinder distortion as a result of the wall images was compensated by increasing the doublet

strength (equation 4.5) approximately 6.6%. The increase of doublet strength to compensate for cylinder distortion is determined of course by the particular values chosen in the example. The final streamlines are presented in Figure A-2.

Comparison of Figures A-1 and 2 permits a visualization of the blockage effects upon the two-dimensional flow over a cylinder and its solid body wake representation when in a finite width channel. As can be noted, the width of the wake and the spacing between streamlines are decreased.

GALCIT Rep 534

PAGE
FIG.

STREAMLINE PATTERN OF TWO-DIMENSIONAL FLOW PAST A CYLINDER IN AN INFINITELY WIDE CHANNEL WITH A SOURCE OF STRENGTH Q=2Ub PLACED 0.50 CYLINDER RADII BEHIND TRAILING EDGE

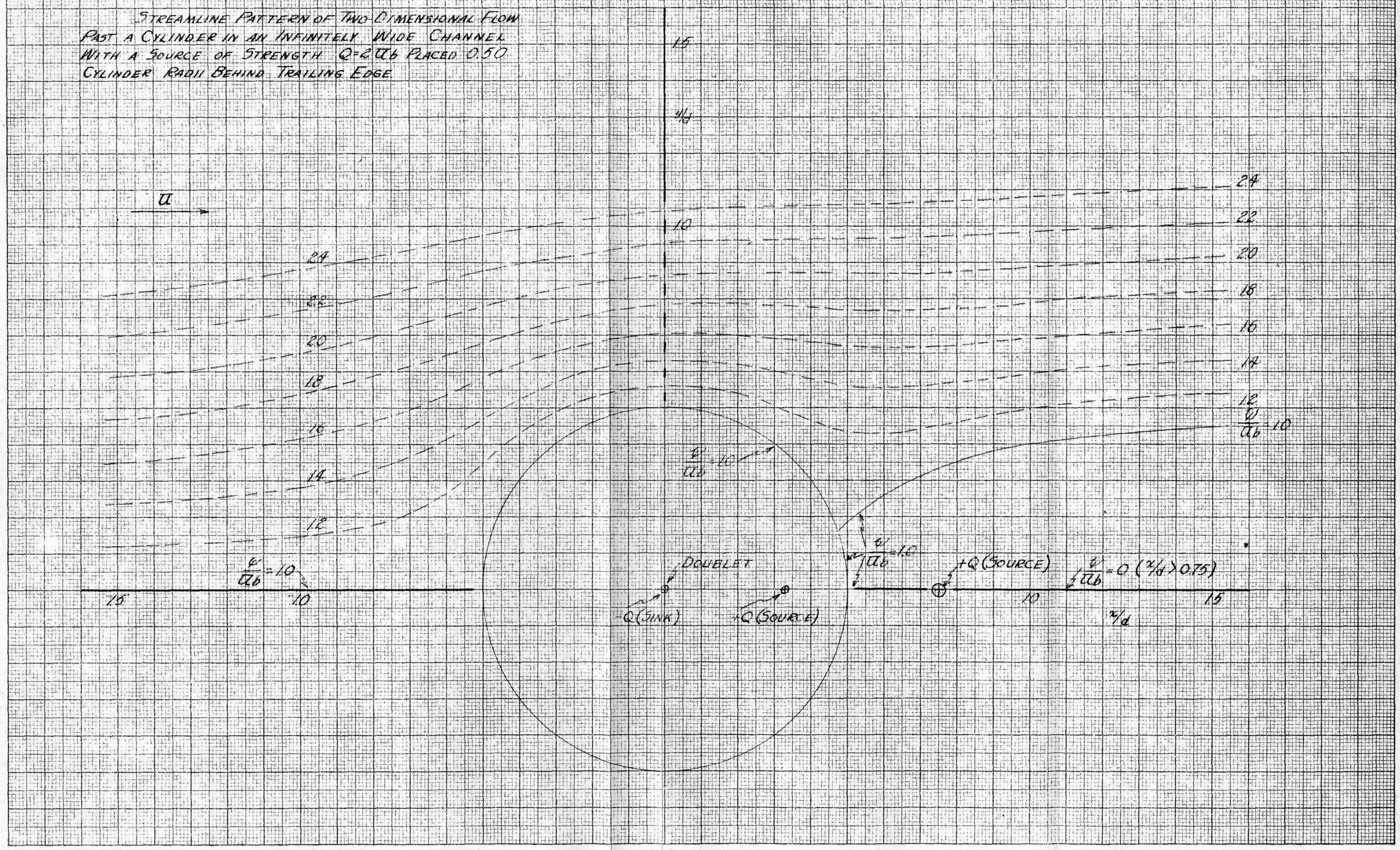

Fig. A-1 Streamlines Past a Circular Cylinder with a Wake Representation, Infinitely Wide Channel

GALCIT Rep 534

PAGE
FIG.

STREAMLINE PATTERN OF TWO-DIMENSIONAL FLOW PAST A CYLINDER IN A FINITE WIDTH CHANNEL WITH A SOURCE OF STRENGTH Q-2Ub PLACED 0.50 CYLINDER RADII BEHIND TRAILING EDGE. RATIO OF CYLINDER DIAMETER TO CHANNEL WIDTH IS 0.124

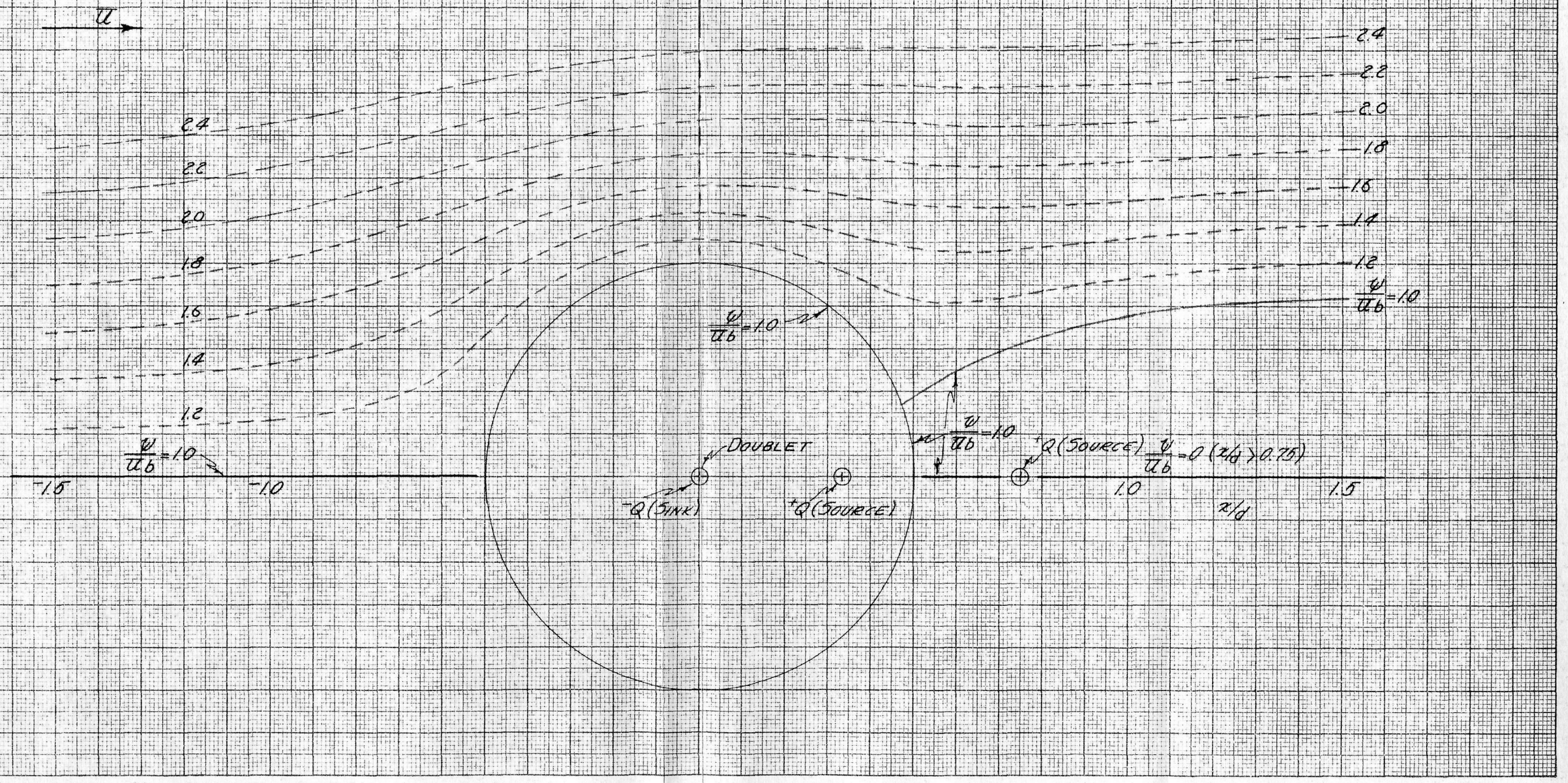

Fig. A-2 Streamlines Past a Circular Cylinder with a Wake Representation, Finite Width Channel

BIBLIOGRAPHY

1. Thom, A., "Blockage Corrections in a Closed High Speed Tunnel," R. and M. No. 2033, British A.R.C., 1943

2. Lindsay, W. F., "Drag of Cylinders of Simple Shapes," NACA T.R. No. 619, 1938

3. Knowler, A. E. and Pruden, F. W., "On the Drag of Circular Cylinders at High Speeds," R. and M. No. 1933, British A.R.C., 1944

4. Bell, R. W., "Determination of Profile Drag by the Momentum Method," CALCIT W.T.T. (unpublished)

5. Prandtl, L., "Aerodynamic Theory," Durand, Vol. III, p. 195, 1934

6. Prandtl, L. and Tietjens, O.G., "Fundamentals of Hydro- and Aeromechanics," Chapter X, 1934

7. Streeter, V.L., "Fluid Dynamics," Chapter VI, 1948